

Unlocking the Key to Life: Observation and Formation of Nitriles in Protoplanetary Disks

A Thesis presented

by

Alessandra Canta

to

The Department of Chemistry

and

The Department of Astronomy

in partial fulfillment of the requirements

for the joint degree of

Bachelor of Arts

in the subjects of

Chemistry and Astrophysics

Harvard University

Cambridge, Massachusetts

April 2021

Unlocking the Key to Life: Observation and Formation of Nitriles in Protoplanetary Disks

Abstract

The chemical composition of protoplanetary disks around young stars affects the chemical habitability of nascent planets. Nitriles are key participants in reactions that lead to pre-biotically interesting molecules such as RNA and amino acids. However, their abundances and formation mechanisms in planet-forming disks are not well constrained. In this thesis, we present the first detection of ortho-CH₂CN in a protoplanetary disk. An excitation analysis reveals a disk-averaged column density (N_{tot}) of $4.7^{+0.4}_{-0.4} \times 10^{12} \text{cm}^{-2}$, and a rotational temperature (T_{rot}) of 38 ± 5 K. A radially resolved analysis shows that the CH₂CN column density peaks within the first 50 au of the disk whereas the T_{rot} remains constant across the disk. Our observations and models point to a close chemical relationship between CH₂CN and the more commonly observed CH₃CN. We then investigate the role of VUV irradiation in nitrile formation by laboratory experiments. We irradiate NH₃:C₂H₆, NH₃:C₂H₄, and NH₃:C₂H₂ ice mixtures at 30 K, 40 K, and 50 K. We find that CH₃CN is formed in a subset of these experiments and that CH₃CH=NH is an intermediate for CH₃CN production. These reactions show a temperature dependence and sensitivity to the unsaturation of the hydrocarbon reactant. Comparison of our findings to observed molecule abundances in clouds suggests that these are not the main pathways for nitrile formation in disks. Contribution from ice chemistry involving the more abundant N₂ should be investigated.

Acknowledgments

First and foremost, I would like to thank my thesis advisor Professor Karin Öberg. I truly could not have asked for a better mentor. I am in awe of her breadth of knowledge on Astrochemistry and her enthusiasm for this subject. I would also like to thank Dr Richard Teague for his encouragement, patience and for always knowing how to answer my myriad of questions. I am so grateful to all the members of the Öberg Astrochemistry Lab - Dr Mahesh Rajappan, Dr Elettra Piacentino, Alexia Simon - for all the guidance and for being so willing to teach me.

Thank you to Dr Rafael Martín-Doménech and Dr Sean Andrews, who served as external readers for this thesis. Their detailed feedback pushed me to sharpen my thinking and brought my work to a higher level.

I would also like to acknowledge Professor John Kovac and my Astronomy 99 peers. I am grateful for their invaluable comments and feedback, which helped me stay on track and made the intimidating task of writing a thesis far less daunting.

A special thanks to Dr Gregg Tucci, the Director of Undergraduate Studies in Chemistry, for his kindness, enthusiasm and guidance. I cannot express how grateful I am for his support as I found my way to Chemistry first and then to Astrophysics. Thank you to Isa, Ksenia, Sanskrati, Sofia-Marie and Zoi for being there every step of the way and cheering me through this journey. Thank you to my family - Mamma, Papà and Peppe - for the endless love and unwavering support. This thesis would not have been possible without them.

CHAPTER 0. ACKNOWLEDGMENTS

Contents

Abstract	ii
Acknowledgments	iii
1 Introduction	1
1.1 Star & Planet Formation	2
1.1.1 Star Formation	3
1.1.2 Planet Formation	5
1.2 Protoplanetary Disks	6
1.2.1 Structure	6
1.2.2 Molecular Inventory	10
1.2.3 The TW Hydrae Protoplanetary Disk	11
1.3 Astrochemistry	13
1.3.1 Gas-phase Reactions	14

CONTENTS

1.3.2	COMs During Star Formation	17
1.3.3	Nitriles	21
1.4	Thesis Motivation and Outline	24
2	Observational Methods & Results	27
2.1	Millimeter Interferometry	28
2.2	The Atacama Large Millimeter/submillimeter Array	30
2.3	Data Collection & Calibration	31
2.4	Image Analysis	32
2.5	Morphology	36
2.6	CH ₂ CN Excitation Analysis	37
2.6.1	Method	38
2.6.2	Disk-Averaged Analysis	40
2.6.3	Radially-resolved Analysis	44
3	Discussion I: CH₂CN in the TW Hya Protoplanetary Disk	47
3.1	CH ₂ CN/CH ₃ CN Ratio & Disk Models Results	47
3.2	CH ₂ CN Radial Morphology	51
3.3	CH ₂ CN Chemistry	53
4	Experimental Methods	57

CONTENTS

4.1	SPACE CAT	57
4.2	VUV Photoprocessing	61
4.3	Analytical Techniques	62
4.3.1	Infrared Spectroscopy	62
4.3.2	Temperature Programmed Desorption	63
4.4	Experimental Design: NH_3 & Hydrocarbons	64
5	Experimental Results	67
5.1	Analysis Overview	67
5.2	$\text{NH}_3\text{:C}_2\text{H}_6$ Ice Mixtures	72
5.3	$\text{NH}_3\text{:C}_2\text{H}_4$ Ice Mixtures	77
5.4	$\text{NH}_3\text{:C}_2\text{H}_2$ Ice Mixtures	86
5.5	Results Summary	95
6	Discussion II: Formation of Nitriles during VUV Photoprocessing	99
6.1	Comparing Hydrocarbons	99
6.2	Temperature Dependence	103
6.3	Astrophysical Implications	105
7	Summary & Conclusions	109
7.1	Summary	109

CONTENTS

7.2	Conclusions & Future Work	111
A	Additional Experimental Results	115
.1	Ammonia & Hydrocarbons	115
.1.1	$\text{NH}_3:\text{C}_2\text{H}_6$	115
.1.2	$\text{NH}_3:\text{C}_2\text{H}_4$	119
.1.3	$\text{NH}_3:\text{C}_2\text{H}_2$	119
.2	Ethylamine ($\text{CH}_3\text{CH}_2\text{NH}_2$)	127
.3	The First Detection of CH_2CN in TW Hya	132
	References	133

Chapter 1

Introduction

The path to biological life on Earth started millions of years before Earth’s formation. Our planet, and more generally, any planet’s suitability for hosting life is in part dictated by the chemical environment and composition of protoplanetary disk within which the planet formed (e.g., Walsh et al. 2015; Bergner et al. 2018). The gas, ice and dust that compose these circumstellar disks are incorporated into nascent planets (this is further elaborated in §1.1.2), and as a result the elemental and (potentially) molecular composition of new planetary systems is regulated by the chemical inventory of disks (Walsh et al. 2015). At this time, over 90 organics (not including isotopologues) of varying complexity have been detected in disks (see Table 1.1 for the full list), yet the provenance of the majority of these molecules remains unknown (McGuire 2018). A challenge lies in discerning whether these species are inherited directly from the protostellar stage, and were therefore already present in the molecular cloud from which the star formed, or whether they are produced *in situ* in the disk (Loomis et al. 2018).

CHAPTER 1. INTRODUCTION

One commonly invoked origin of organic molecules in both protostellar envelopes and protoplanetary disks is ice chemistry. When simple laboratory ice mixtures are exposed to the conditions analogous to those in disks, molecules ranging from simple hydrocarbons to amino acid residues are observed in the products (e.g., Muñoz Caro et al. 2002; Nuevo et al. 2010). These ice experiments demonstrate the possibility that *in situ* formation is responsible for the production of the organic molecules observed in disks. On the other hand, studies of meteorites and comets in our Solar System provide contrasting evidence, as their molecular composition is similar to that of protostellar envelopes, thus suggesting that the organic composition of planetesimals was passed down directly from the Protosolar Nebula to the disk surrounding the young Sun (Altwegg et al. 2020; Mumma & Charnley 2011). Alternatively, both of these mechanisms could contribute to the chemical reservoir of nascent planets. Understanding where these molecules come from will help trace the trajectory of the organic chemistry as it evolves during planet formation, estimate the organic inventory of newly-formed planets, and ultimately determine what factors contribute to their chemical habitability.

1.1 Star & Planet Formation

All stars form from the collapse of interstellar cloud cores, however, there are substantial differences between the formation pathway of low-mass stars ($< 2 M_{\odot}$) and that of more massive stars. In this thesis, we will use the term "star" to refer to low-mass, solar-like stars, and protostars unless otherwise specified. This is because $< 2 M_{\odot}$ stars are the most common in our Galaxy and they also have a longer

lifetime, which means that they are more likely to see the formation of both planets and pre-biotic life (Öberg & Bergin 2020).

1.1.1 Star Formation

Giant molecular clouds (GMCs) are cold ($T \approx 10$ K), denser regions of the interstellar medium (ISM) and are as massive as $\sim 10^4 M_\odot$ and as large as 100 pc (Williams et al. 1994). Moderate density gas ($\sim 20 \text{ H}_2 \text{ cm}^{-3}$) surrounds a highly structured, hierarchical environment composed of over-dense regions, namely clumps and cores, whose high density ($10^3 - 10^5 \text{ H}_2 \text{ cm}^{-3}$) is particularly conducive to star formation (Bergin & Tafalla 2007). Cores tend to be ~ 1 order of magnitude smaller (0.03-0.3 pc vs 0.3-3 pc) and ~ 2 orders of magnitude more dense than clumps, thus increasing the likelihood of gravitational collapse (Bergin & Tafalla 2007; Benson & Myers 1989). Cores that are destined to this fate are called pre-stellar, and they are depicted in Figure 1.1a.

The prestellar core begins to collapse (Figure 1.1b) due to its own gravity. At first, this collapse is isothermal as the core remains optically thin. However, when the central density reaches $10^{-13} \text{ g cm}^{-3}$ the sphere of gas becomes opaque and the collapse begins to decelerate reaching a halt when the central density reaches $2 \times 10^{-10} \text{ g cm}^{-3}$ and the temperature reaches ~ 2000 K. At this point, there is a second collapse resulting in the formation of a smaller hydrostatic core, now a protostar, surrounded by an envelope of material that continues to fall onto the central object (Larson 2003). Figure 1.1c shows the continued inflow of material onto the protostar. Much of the material remaining from the original cloud forms a

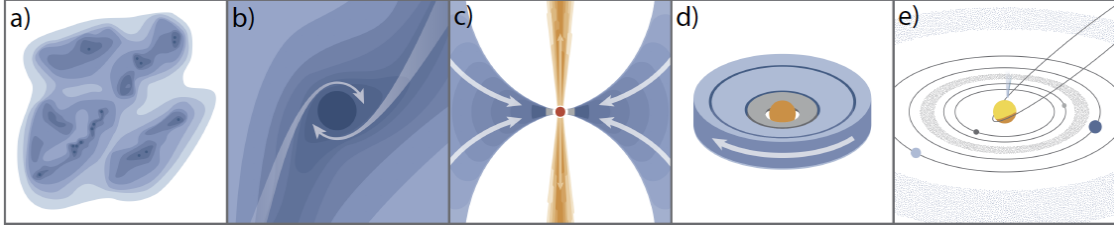


Figure 1.1 Cartoon showing the formation of a low-mass star (a) Stars form dense regions of GMCs called pre-stellar cores. (b) The first stage of star formation: dense core starts to collapse due to self-gravity. (c) Formation of a protostar and associated circumstellar disk. The latter allows for the continued accretion of remnant cloud material. (d) Following dispersion of cloud material, the pre-main sequence star and its protoplanetary disk are revealed. (e) Gas giants, as well as rocky and ice planets are formed. Figure from Öberg & Bergin (2020) and reproduced with permission from the authors.

circumstellar disk around the young stellar object (YSO). This disk is born out of the necessity to bring material inwards towards the YSO and angular momentum outwards, away from the YSO, as otherwise the protostar would be torn apart by the sheer force of its own rotation (Larson 2003; Williams & Cieza 2011; Henning & Semenov 2013). Within the optically thick envelope, the temperature of the protostar continues to increase until it reaches $\sim 10^6$ K and fusion can begin. If the envelope also contains emission from rotationally excited complex organic molecules (COMs), it is known as a hot corino and it is thought to be very chemically active (van Dishoeck & van der Tak 2002; van der Tak et al. 2003). These objects are formed in the innermost regions of the envelope around the central object, with temperatures > 100 K. Outflows in the form of shocks and collimated bipolar jets are also observed during the protostar stage. Although their role is not well understood

yet, there is evidence that they are responsible for speeding up the ejection of the envelope and contributing to the end of the accretion onto the star from the disk (Shu et al. 1991; Arce & Sargent 2005). Once the envelope is completely dispersed, the pre-main sequence star and its circumstellar disk are revealed (Figure 1.1d) and planet formation can begin. There is also evidence from recent observations that suggests that planet formation begins before the protostellar envelope disappears (Harsono et al. 2018).

1.1.2 Planet Formation

Terrestrial planet formation begins with μm -sized dust grains in the disk growing into mm-sized objects via adhesive two-body collisions (Armitage 2018). The next step is creating objects of the order of a km, these are known as *planetesimals*. The leading hypothesis for their formation is *streaming instability*, which essentially states that the drag force felt by dust particles orbiting in a gaseous disk creates density perturbations and causes the formation of gravitationally unstable clumps prone to collapse (Youdin & Goodman 2005). Once planetesimals have formed, the subsequent formation of planets depends on the strength of the collisions between similar-sized objects. Slower collisions in the cold areas of the disk are preferred for aggregation of bodies over high-velocity impacts as the latter may result in the fragmentation of the planetesimal. Planetesimal accretion continues until the *feeding zone* is almost depleted (Pollack et al. 1991). This is defined as the region of the protoplanetary disk from which a growing planet can accrete planetesimals, it is usually an annulus of $5 r_H$ on each side of the orbit (Fortier et al. 2013). The Hill

CHAPTER 1. INTRODUCTION

radius, r_H , is the area over which the protoplanet’s gravity dominates over the tidal force of the central star, and is given by the equation:

$$r_H = \left(\frac{M}{3M_\star} \right)^{\frac{1}{3}} \cdot a \quad (1.1)$$

where M is the mass of the protoplanet, M_\star is the mass of the central star and the size of the orbit of the planet around the central star is a (Armitage 2018; D’Angelo & Lissauer 2018). The protoplanet stops growing when it reaches the mass of the planetesimals in the feeding zone. This is called the *isolation mass* (Armitage 2018). As the mass of the body increases, so does their ability to trap and retain gases which leads to the formation of a primary atmosphere around certain planets (are big enough to accrete a primary atmosphere) (Lissauer 1993). Above a critical core mass ($M_{core} = 5 - 20 M_\oplus$), the gaseous envelope surrounding the protoplanet becomes unstable and it collapses onto itself due to self-gravity thus forming a gaseous planet (Armitage 2018; Mizuno 1981). Alternatively, above this core mass gas accretion is fast enough that the planet mass size can double very quickly, thus entering a regime of runaway accretion and leading to the formation of gas giants.

1.2 Protoplanetary Disks

1.2.1 Structure

Young protoplanetary disks are mainly composed of gas, but about 1% of the mass is in small silicates and graphite grains with a radius on the order of a tenth of a micrometer (Draine 2003; Henning & Semenov 2013). As the disk ages, the size of the grains increases from micron-sized to cm-sized pebbles (Williams & Cieza

2011). Most of the disk presents a vertical temperature gradient, with temperature ranging from < 20 K in the midplane to $\gtrsim 100$ K in the photon-dominated region (uppermost layers) (Williams & Cieza 2011). This structure is partially due to the type of radiation that is able to reach the different layers, and therefore, different chemical environments can also be observed in different parts of the disk. The type of irradiation that prevails as well as the different temperatures are schematically depicted in Figure 1.2.

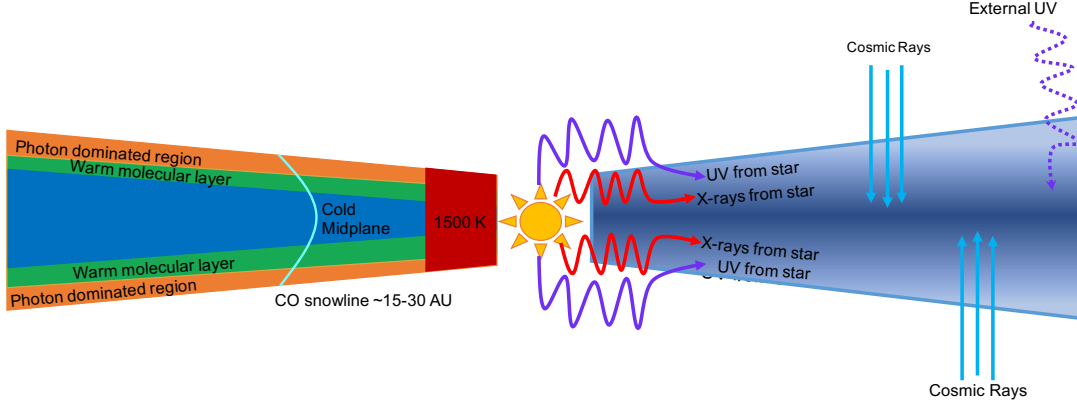


Figure 1.2 Cartoon showing the structure of a protoplanetary disk. The contribution from different types of radiation is shown on the right, whereas on the left the different chemical environments are shown. The CO snowline is also depicted, beyond this point all volatiles are found as ices in the midplane. This happens between 17 and 30 AU in the TW Hya disk, the disk we observed as a part of this thesis (Qi et al. 2013; Schwarz et al. 2016). This figure has not been drawn to scale.

Temperature and Chemical Environment

The temperature close to the star can exceed 1,000 K resulting in the sublimation of refractory materials (e.g, Al_2O_3) and the destruction of carbon-containing

CHAPTER 1. INTRODUCTION

compounds (D'Alessio et al. 1999; Henning & Semenov 2013). This region of the disk has an active chemistry, dominated by collisional dissociation reactions, where hydrogen is removed from saturated carbon-chain molecules and other species are destroyed (for example SO_2) (Willacy et al. 1998). The chemistry that we can observe using ALMA (Atacama Large Millimeter/submillimeter Array, further discussed in Chapter 2) occurs in the outer regions of nearby star-forming regions. The majority of the chemical reactions that lead to the formation of COMs are thought to occur on the surface of dust grains in the cold midplane (shown in blue on the left side of Fig. 1.2) (Semenov 2011). This region is largely shielded from the high-energy interstellar radiation field (except cosmic rays) as it is embedded within the optically thick warm molecular layer and photon-dominated region, which explains its low (<20 K) temperature (Henning & Semenov 2013). Organic synthesis occurs by formation of radicals on the surface of the grain, diffusion, and subsequent rearrangement (this will be thoroughly discussed in Section 1.3.2). Thermal desorption as well as cosmic-ray and X-ray induced desorption, and chemical desorption are then responsible for the release of these newly formed molecules into the gas-phase (Leger 1987; Henning & Semenov 2013). Desorbed, gas-phase molecules are found in the warm molecular layer (shown in green in Fig. 1.2). Here, the temperature ranges between 30-70 K as the layer is partially shielded from high-energy radiation. The C/O ratio in this region of the disk can be larger than one, which leads to a rich Carbon chemistry (Semenov 2011; Du et al. 2015; Bergin et al. 2016). Finally, the photon-dominated region is the outermost vertical layer and it is shown in orange in Fig. 1.2. Photodissociation of molecules is particularly prevalent in this regions because of the exposure to high-energy UV (usually in the form of Lyman- α) and

CHAPTER 1. INTRODUCTION

X-ray radiation, mostly from the central star and with limited contribution from the interstellar radiation field (Schindhelm et al. 2012; Henning & Semenov 2013). The presence of this irradiation also means that temperatures in this region are the highest, at $\gtrsim 100$ K.

UV-Irradiation, Cosmic Rays & Electron Bombardment

Young solar-type stars, like the T Tauri star at the center of TW Hya, emit an excess of X-rays and VUV (vacuum-ultraviolet) radiation in the Lyman- α range (121.6 nm) (Herczeg et al. 2002; Bergin et al. 2003). Other sources of UV-irradiation include nearby massive stars and the interstellar radiation field (ISRF). However, these are only relevant close to the edge of protoplanetary disks as the stellar radiation field dominates closer to the central star (Aikawa & Herbst 1999). As shown in Fig. 1.2, the outermost regions of the disk tend to have the highest UV-flux and the PDR-like disk atmosphere extends all the way down to the disk midplane, therefore much of the chemistry is driven by photo-dissociation. The importance of UV-driven reactions will be further elaborated in Sections 1.3.2 & 1.3.1. The density of dust and ice grains increases with increasing proximity to the midplane, which also means that VUV and X-ray radiation is blocked out (Bergin et al. 2007; Williams & Cieza 2011). In this region more penetrating radiation, such as cosmic rays, are prevalent and therefore are thought to drive the majority of the chemistry in the midplane (Öberg 2016).

Cosmic rays (CRs) are charged particles that are accelerated to high velocities by unknown astrophysical sources (Ferrari & Szuszkiewicz 2009). Although the vast

CHAPTER 1. INTRODUCTION

majority of CRs are composed of protons, they can also be made of α -particles, heavier nuclei, and electrons (Mewaldt et al. 1996; Clem et al. 1996). The contribution to the chemistry by cosmic rays (CRs) vs. UV irradiation is still a debated topic. When CRs pass through molecules deposited on ice, they create a shower of secondary electrons, δ -electrons, which are available for reactions (Öberg 2016; Shen et al. 2004; Bennett et al. 2005). Though electrons with energy as high as 2 keV are produced from this process, it is the low energy electrons that have the most impact on the chemistry and experiments have shown that molecules as complex as dipeptides can be formed following low-energy electron bombardment of simple ice mixtures (Kaiser et al. 2013). Further discussion on the chemistry is in § 1.3. CRs are particularly relevant in the denser, cold (< 30 K), areas of the disk as UV and X-rays are not able to reach such optically thick regions (Cleeves et al. 2015; Aikawa & Herbst 1999). Therefore, the effect of CRs is particularly important in the midplane where the gas density can considerably surpass $n_{\text{H}_2} = 10^9 \text{ cm}^{-3}$. Here, CRs are the the main drivers of both gas-phase and solid-phase chemistry as the interstellar radiation field and the radiation from the central star are not able to contribute (Cleeves et al. 2015; Herbst & Klemperer 1973).

1.2.2 Molecular Inventory

Carbon monoxide and its isotopologues were the first molecules to be detected in protoplanetary disks, followed by slightly larger compounds such as HCN and H_2CO (Dutrey et al. 1997). The advent of the Atacama Large Millimeter/submillimeter Array (ALMA) in 2013 significantly facilitated the expansion of this library as it

CHAPTER 1. INTRODUCTION

allowed the detection of more complex organics. However, ALMA only allows for detection of 2-3 carbon molecules in the gas-phase, which are a small fraction of disk COMs since the majority are expected to be found in the solid-state (see §1.3.2 for more on chemistry). This means that our library of species most likely only represents a small proportion of the true molecular population in disks. At present, detected COMs include oxygen bearing species including methanol, CH_3OH , and formic acid, HCOOH , and nitriles such as acetonitrile, CH_3CN , and cyanopolyne, HC_3N (Chapillon et al. 2012; Walsh et al. 2016; Favre et al. 2018). The full repertoire of all observed species in protoplanetary disks can be found in Table 1.1. These are all relatively small, simple molecules compared to those that have been detected in molecular clouds and protostellar hot corinos where organics as complex as benzonitrile, $\text{c-C}_6\text{H}_5\text{CN}$, and as large as the fullerenes C_{60} and C_{70} have been observed (in TMC-1 and Tc 1 respectively) (Cami et al. 2010; McGuire et al. 2018). Therefore, further observations are needed to try bridge the gap between protoplanetary disks and earlier stages of star formation, or, if these molecules remain undetected in disks, to use laboratory experiments and models to predict their distribution and the overall chemical evolution.

1.2.3 The TW Hydrae Protoplanetary Disk

The main disk that we will be focusing on in the observational part of this thesis is the disk around TW Hya, a $\sim 0.8M$ solar-like T Tauri star that is often used in astrochemical observations because of its proximity (60.1 pc Bailer-Jones et al. 2018) and its face-on orientation, $i \approx 5^\circ$, which allows for easier interpretation of data.

CHAPTER 1. INTRODUCTION

Table 1.1. List of Molecules and Isotopes Observed in Protoplanetary Disks. This table has been reproduced from McGuire (2018) and adapted to reflect new detections.

2 Atoms		3 Atoms		4 Atoms		5 Atoms		6 Atoms	
Species	Ref	Species	Ref	Species	Ref	Species	Ref	Species	Ref
CO	2	HCN	10, 22	H ₂ CO	11	CH ₄	15	CH ₃ CN	26
¹³ CO	34	HNC	11	C ₂ H ₂	23	c-C ₃ H ₂	31	CH ₃ OH	38
CS	27, 4, 16	C ₂ H	11	HC ₃ N	8, 26	HCOOH	13		
C ¹⁸ O	10	HCO ⁺	11, 22	NH ₃	32	CH ₂ CN	5		
CN	11, 22	H ¹³ CN	18	H ₂ CS	24				
H ₂	35	N ₂ H ⁺	29, 12						
C ¹⁷ O	35, 17	DCO ⁺	9						
OH	25, 33	H ₂ O	6, 33, 20						
SO	14	CO ₂	7						
CH ⁺	37	DCN	30						
HD	3	H ¹³ CN	18						
C ¹⁵ N	19	HC ¹⁵ N	18						
C ³⁴ S	1	N ₂ D ⁺	21						
		H ₂ S	28						

References. — [1] Artur de la Villarmois et al. (2018), [2] Beckwith et al. (1986), [3] Bergin et al. (2013), [4] Blake et al. (1992), [5] the detection of this molecule will be the focus of Chapter 2, [6] Carr et al. (2004), [7] Carr & Najita (2008), [8] Chapillon et al. (2012), [9] van Dishoeck et al. (2003), [10] Dutrey et al. (1994), [11] Dutrey et al. (1997), [12] Dutrey et al. (2007), [13] Favre et al. (2018), [14] Fuente et al. (2010), [15] Gibb & Horne (2013), [16] Guilloteau et al. (2012), [17] Guilloteau et al. (2013), [18] Guzmán et al. (2015), [19] Hily-Blant et al. (2017), [20] Hogerheijde et al. (2011), [21] Huang & Öberg (2015), [22] Kastner et al. (1997), [23] Lahuis et al. (2006), [24] Le Gal et al. (2019c), [25] Mandell et al. (2008), [26] Öberg et al. (2015), [27] Ohishi et al. (1991), [28] Phuong et al. (2018), [29] Qi et al. (2003), [30] Qi et al. (2008), [31] Qi et al. (2013), [32] Salinas et al. (2016), [33] Salyk et al. (2008), [34] Sargent & Beckwith (1987), [35] Smith et al. (2009), [36] Thi et al. (1999), [37] Thi et al. (2011), [38] Walsh et al. (2016), [39] van Zadelhoff et al. (2001).

CHAPTER 1. INTRODUCTION

The disk is approximately 10 Myr old and models fit to observations have shown that it is still accreting gas at a rate of $\sim 1.8 \times 10^{-9} \text{ M}_{\odot} \text{ yr}^{-1}$ (Ingleby et al. 2013; Weinberger et al. 2013). Its total gas mass has been calculated to be 0.11 M_{\odot} , and a total dust mass of $15\text{-}80 \text{ M}_{\oplus}$, both of these parameters being significantly higher than the average for a disk of this age (Manara et al. 2018; Williams et al. 2019; Nayakshin et al. 2020). TW Hya also presents several gaps in the continuum sub-mm dust emission on the scale of 1-44 au, which suggest the presence of budding planets (none have been officially detected, however) (Andrews et al. 2016; Tsukagoshi et al. 2016). So far, the list of molecules detected on TW Hya is largely dominated by simple molecules and very few COMs. Small species include: CO, CN, HCN (and its isotopologues H^{13}CN and HC_{15}N), C_2H , CS, NH_3 (Qi et al. 2004; Kastner et al. 2015; Salinas et al. 2016; Teague et al. 2017; Hily-Blant et al. 2019; Teague & Loomis 2020). More complex organics include: CH_3CN , CH_2CN , CH_3OH , H_2CO , HCOOH (Walsh et al. 2016; Öberg et al. 2017; Bergner et al. 2018; Favre et al. 2018; Loomis et al. 2018).

1.3 Astrochemistry

The chemistry in protoplanetary disks affects the molecular composition of nascent planets, as when planetesimals form from the dust grains in the disk, they also inherit the volatiles that are frozen-out on the surface of the grains. Therefore, studying the chemistry in the disk also allows us to better understand what kind of molecules can be passed down to new planets and what factors contribute to their chemical habitability. In turn, the chemical diversity in disks is partially dictated by

the chemistry taking place during star formation, which means that understanding the chemical environment at the early stages of star formation provides insight in the composition of disks. In addition to this, the physical conditions in prestellar cores and protostellar envelopes are similar to those in the midplane and the warmer layers of the disk, respectively. This means that we can infer much about the chemistry in different layers of the disk from the chemistry in early star development stages.

1.3.1 Gas-phase Reactions

There are different mechanisms that contribute to gas-phase chemistry and they depend on the kind of species taking place in the reaction. Herbst & Klemperer (1973) and Öberg & Bergin (2020) provide a comprehensive summary of the possible gas-phase reactions, which are summarised in the Table 1.2.

Reaction Type	Mechanism	Formula	Midplane ML PDR		
Bond Rearrangement	Ion-molecule	$A^+ + B \longrightarrow C^+ + D$	X	X	X
	Neutral - Neutral	$A + B \longrightarrow AB$	X	X	0
	Charge Transfer	$A^+ + B \longrightarrow A + B^+$	X	X	X
Bond Formation	Radiative Association	$A^+ + B_2 \longrightarrow (AB_2^+) + h\nu$	X	X	X
	Associative Detachment	$A^- + B \longrightarrow AB + e^-$	X	X	X
Bond Destruction	Photodissociation	$AB + \gamma \longrightarrow A + B$	0	X	X
	Dissociative Recombination	$AB^+ + e^- \longrightarrow A + B$	X	X	X

Table 1.2: List of possible gas-phase reactions and the locations that they can occur in as reported by Herbst & Klemperer (1973), Öberg & Bergin (2020), and Semenov (2011). The warm molecular layer and the photon-dominated region of the disk are respectively indicated by ML and PDR.

CHAPTER 1. INTRODUCTION

Bond rearrangement reactions include: ion-molecule, neutral-neutral, and charge transfer reactions. The majority of these reactions are binary, so they only involve two reactants. Three-body reactions of the form $A + B + C \longrightarrow (ABC)^* \longrightarrow AB + C$, are extremely rare which restricts the kind of products that can be formed (Öberg & Bergin 2020; Hasegawa & Herbst 1993). Other limitations include the cold temperatures, especially closer to the disk midplane exterior to the CO snowline, which means that it is less likely for molecules to possess enough kinetic energy to overcome the activation barriers (Öberg & Bergin 2020). Bond formation mechanisms include radiative association and associative detachment. The latter tends to be faster than radiative association, however, it involves anions and these species are rare in the interstellar medium and in protoplanetary disks (Öberg & Bergin 2020). The low gas density of the ISM and of the disks means that when reactions do occur, they first form an unstable intermediate prone to re-dissociation (Wakelam et al. 2010). However, by radiating away some of the extra energy, the intermediate is able to find stability. This is the process of radiative association, the main pathway to the formation of larger ions containing carbon and hydrogen (Wakelam et al. 2010). Bond dissociation reactions include photodissociation and dissociative recombination (DR), which involve the absorption of a photon and an electron respectively. Photodissociation is dominant in regions of the disk and the ISM where UV flux is particularly high. Upon absorption of the photon, the now excited molecule can begin to dissociate (predissociation) or decay into a dissociative state (spontaneous radiative dissociation) (Öberg & Bergin 2020; van Dishoeck & Black 1988). In DR, the electron is captured by the ion, causing the formation of a doubly excited neutral molecule that then dissociates into the final product (Bates

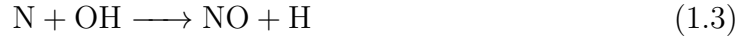
CHAPTER 1. INTRODUCTION

1950). The electrons needed for this process are available as a result of ionisation by X-rays, UV-rays, and the interaction between cosmic rays and ice grains as discussed in §1.2.1.

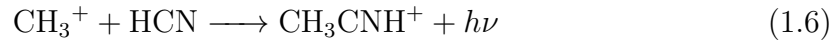
Most reactions that lead to the formation of small, simple molecules are hypothesised to occur in the gas phase (Semenov 2011, e.g.). For example, the production of C_2N primarily happens in the gas phase via the neutral-neutral reaction:



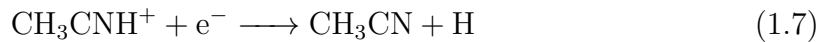
(Loomis et al. 2018). C_2N can freeze out on grain surfaces, which then may lead to the formation of COMs, such as CH_3CN , in the solid state. Hydrogen cyanide is one of the main reactants that leads to the formation of nitriles in the gas phase, and using the chemical models computed Agúndez et al. (2008), the gaseous pathway from N to HCN can be retraced as shown below:



COMs such as acetone nitrile can also be formed through a gaseous pathway by radiative association



followed by dissociative recombination



(Loomis et al. 2018; Le Gal et al. 2019a). This combination of radiative association, followed by dissociative recombination is common in the production of nitriles in

the gas phase and it will also be relevant for the formation pathways of CH_2CN . However, it is worth noting that this reaction pathway vastly under-predicts the CH_3CN abundance in disk chemistry models, and surface pathways are generally believed to be the main source of this molecule.

1.3.2 COMs During Star Formation

The low temperature in pre-stellar cores and giant molecular clouds ($< \sim 10$ K) means that all gases except for He, Ne and, H_2 condense and form a mantle on the surface of grains where cold chemistry can occur (Hiraoka et al. 1995). Under these conditions, the formation of small molecules (NH_3 , H_2CO) can occur via the interactions of atoms such as N, H, C, and O. For example, Hiraoka et al. (1995) found that H atoms migrate in N_2 and H_2O matrices at ~ 10 K and that they can react with N atoms, generated from the photodissociation of N_2 , to form ammonia by successive hydrogenation:



(Hiraoka et al. 1995). This mechanism has also been proposed for the formation of slightly more complex organics, such as CH_3OH and H_2CO (Tielens & Hagen 1982; Tielens & Allamandola 1987). In fact, Watanabe & Kouchi (2002) were able to produce formaldehyde from the sequential hydrogenation of CO ices, the two main reservoirs of carbon and oxygen. A graphical depiction of hydrogenation pathway on ice grains is shown in Figure 1.3. The heat released from these reactions is then

responsible for the desorption of a small fraction of the newly formed, hydrogenated molecules to the gas phase, through so called chemical desorption.

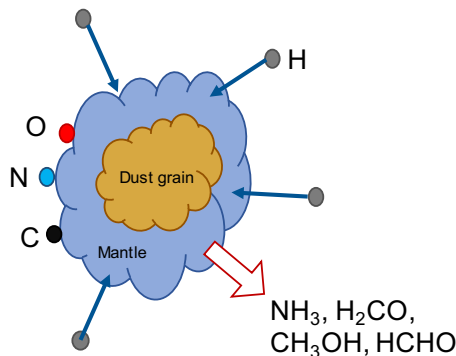


Figure 1.3 Cartoon depicting the formation of simple, hydrogenated molecules in cold ($< \sim 10$ K) environments. H atoms migrate on the surface of N_2 or H_2O mantles and react with atoms on their surface. A small fraction of these products is released into the gas phase by the heat released during chemical reactions.

These molecules, which can be formed on the grain surfaces in prestellar cores before they begin to collapse, are termed zeroth generation molecules (Herbst & van Dishoeck 2009; Visser et al. 2009). One of the questions that remains unanswered is when during star formation, COMs start being formed from zeroth generation molecules. The original hypothesis is that during the collapse and hot corino stage, zeroth generation molecules evaporate from the surface of the grains and take part in gas-phase reactions, which lead to COMs. Alternatively, the "warm-up scenario" by Garrod & Herbst (2006) states that COMs can also form on the surface of grains prior to the hot corino stage. These radical-radical reactions are only expected to work if the grain is exposed to warmer temperatures in the range of $\sim 30 - 40$ K for an extended period of time (in the order of $\sim 10^3 - 10^4$ years) (Vasyunin et al. 2017). These conditions are present in the protostellar envelope. The products are

CHAPTER 1. INTRODUCTION

then released into the gas phase when the grains approach the protostar and are heated to a temperature above 100 K.

One proposed mechanism for the formation of radicals is energetic processing by VUV-irradiation or cosmic rays. In the case of photochemistry (i.e. if the grain is hit by VUV photons), the molecules will be in an excited state and will subsequently either decay back into their original state, or split up into radicals. Alternatively, they could participate in an electron transfer ($A^* + B \longrightarrow A^+ + B^-$), or transfer their excitation to another molecule ($A^* + B \longrightarrow A + B^*$), which could start a reaction chain, or participate in bimolecular reactions ($A^* + B \longrightarrow C + D$) (Semenov 2011). In these reactions, the number of electrons remains constant, but this is not the case with radiolysis. This is when a cosmic ray hits a molecule on ice, which releases a cascade of electrons (δ -electrons) (Shen et al. 2004). These low energy electrons can then either ionise nearby molecules, or excite them so that they dissociate and yield two radicals, or they are absorbed by molecules to produce a transient negatively charged intermediate (Herbst & Klemperer 1973). These are reactive species and they would either react with their original molecule or with any of the daughter products, thus giving rise to new species. The different steps of this mechanism are summarised in Figure 1.4.

The idea that at least a luke-warm (30 K) temperature is needed for the production of COMs has been challenged by discoveries of COMs in cold, pre-stellar cores which suggest that the formation of complex organics can proceed already at 10 K. Among the complex species that have been observed there are acetaldehyde (C_2H_4O), dimethyl ether (C_2H_6O), and methyl formate ($C_2H_4O_2$) (Öberg et al. 2010; Bacmann et al. 2012; Vastel et al. 2014; Jørgensen et al. 2020, e.g.). Recently, Beaklini et al.

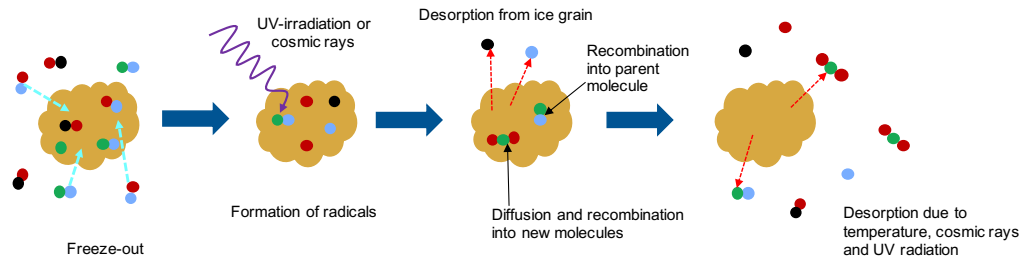


Figure 1.4 Cartoon showing the mechanism by which COMs are proposed to form on the surface of ice grains. The first step shows the freeze-out of molecules from the gas-phase to the surface of the grains. This is followed by UV irradiation or electron bombardment by cosmic rays, in both cases radicals are formed. These can either reform into the parent molecule, recombine to form a new molecule, or thermally desorb and go back to the gas-phase. Finally, the action of temperature or chemical desorption will cause the desorption of the newly-formed molecules.

(2020) also reported the detection of complex nitriles, namely $\text{CH}_3\text{CH}_2\text{CN}$ and CH_3CN in IRDC-C9, a complex of cold cores. The variety of species that is being detected implies that there is a rich chemistry happening, even in the cold and quiescent conditions of the pre-stellar cores.

The first model that attempted to explain these unusual observations was proposed by Vasyunin & Herbst (2013). The proposed mechanism involved reactive desorption (aka chemical desorption or desorption upon formation), a type of non-thermal desorption of selected precursor molecules, such as CH_3OH , H_2CO . Once in the gas-phase, these molecules can participate in ion-molecule reactions to form COMs. Overall, the predicted abundance of volatiles produced by this mechanism was in good accordance with observations of COMs and their precursors, except for formaldehyde, whose abundance was overestimated by ~ 2 orders of magnitude. The

conditions in prestellar cores are similar to the chemical environment in the midplane of disks as they are both dense and with temperatures ~ 10 K. Therefore, these pathways could be analogous to the chemistry that takes place in the midplane.

This model was refined by Reboussin et al. (2014), who included heating of the grain and the mantle by cosmic-rays; by Balucani et al. (2015), who also included neutral-neutral reactions in the network of gas-phase pathways; and finally by Vasyunin et al. (2017) who included a layer-by-layer approach to grain chemistry, and a wider gas-phase reaction network. This latter model proved to be in very good accordance with observations, and accurately predicted the abundances of methyl formate, dimethyl ether, and acetaldehyde in cold cores.

The COM formation chemistry developed for cores and protostellar envelopes is directly applicable to the chemistry in protoplanetary disks, since the same range of temperatures exist in disks. Initially cold grains could be warmed up over time if streaming in towards the star, or lifted up into the atmospheres, similar to the protostellar warm-up model, while the disk midplane is analogous to prestellar cold cores. The different steps are summarised in Fig. 1.4.

1.3.3 Nitriles

Nitriles (or cyanides) are organic molecules containing a nitrogen-carbon triple bond, $C\equiv N$. They appear to be the building blocks of the terrestrial origins of life chemistry out of which life emerged on Earth about 3.5-4 billion years ago. Within this chemical network they have been identified as key precursors for the synthesis of RNA ribonucleotides and amino acids (Powner et al. 2009; Patel et al.

2015). The role of nitriles in the production of amino acids was constrained by two different groups, namely by Woon (2002) and Elsila et al. (2007). Woon (2002) used quantum chemical models to calculate the kinetics of the reactions leading to the production of the amino acid glycine, serine, and alanine. They found that HCN was a key reactant for the formation of methylamine radical CH_2NH_2 , which together with the COOH radical, was essential for the formation of amino acids. In addition, theoretical isotope labelling predicted that HCN provides the C and N in the central carbon (side chain) and in the amino group of the amino acids. On the other hand, Elsila et al. (2007) first irradiated two ice mixtures ($\text{H}_2\text{O}:\text{CH}_3\text{OH}:\text{NH}_3$ and $\text{H}_2\text{O}:\text{CH}_3\text{OH}:\text{HCN}$ both in a ratio of 20:2:2). The major products were glycine, alanine, and serine. Isotope labelling experiments were used to investigate the origins of the carbons and nitrogen in these compounds. They conclude that HCN provides the nitrogen, central carbon, and acid carbon atoms and that only in the case of serine can the amino nitrogen come from NH_3 . Overall, they show that HCN is responsible for the major pathway that gives rise to the three aforementioned amino acids, and while they can also be formed in the absence of HCN, the yield is significantly reduced. Despite using different approaches, both parties found that the major pathway by which the amino acid was being formed included HCN as an essential reactant.

Studies of comet composition have shown that HCN, CH_3CN , and HC_3N were present in the young solar nebula (Mumma & Charnley 2011; Biver et al. 2002; Crovisier et al. 2009). Laboratory ice experiments have shown that there are pathways from both N_2 and NH_3 , the most abundant N-containing molecules in disks, to simple and complex nitriles. The diatomic molecule N_2 is present in larger quantities than NH_3

CHAPTER 1. INTRODUCTION

in the disk, but it is primarily available in the midplane (Bisschop et al. 2006; Li et al. 2013). Because of this, we would expect that the majority of the chemistry that involves N_2 is driven by cosmic rays as they are able to penetrate deeper into the disk and reach the midplane. Nevertheless, one proposed pathway for the production of $\text{C}\equiv\text{N}$ -bearing species is the VUV-irradiation of simple hydrocarbons embedded in a N_2 matrix. Upon VUV-irradiation at 20 K, Wu et al. (2012) reported the formation of HNC and HCN in a ratio of 0.5-0.7 and showed that HCN production has the highest branching ratio at Lyman- α wavelength. Experiments carried out using electron bombardment, which is analogous to the electron shower induced by cosmic rays upon interaction with disk ices, revealed an alternative formation pathway for nitriles. Chin et al. (2016) mirrored the experiment carried out by Wu et al. (2012) and found that nitrile formation occurred at the higher temperature (> 30 K), whereas the lower temperatures (10 -20 K) were dominated by CH_3 and N_3 radicals.

Alternatively, NH_3 chemistry can be investigated as it likely also contributes to the formation of nitriles in disks. While N_2 reactions mainly occur in the midplane, NH_3 -driven chemistry is prevalent in the outer, cold edges of the disk as the abundance of NH_3 is highest in the outer radii (Pontoppidan et al. 2019). In these regions of the disk, UV-flux is also highest as the disk is more diffuse so we expect more contribution from VUV-irradiation driven chemistry. While there is a lack of literature on the formation of nitriles from the VUV photoprocessing of ice mixtures, this is not the case for electron bombardment. Kundu et al. (2017) used electron bombardment on mixtures of NH_3 and CH_4 at 15 K. They detected CN (and its ion CN^-), HCN, and CH_2NH in the products. The findings suggest that low-energy electrons are able to initiate complex reactions in condensed ice mixtures. Though

the reaction pathway could not be constrained with certainty, a likely hypothesis is that when CH_4 is activated in the presence of NH_3 , CH_2 and NH radicals are formed, which in turn react to form CH_2NH (the major product of this reaction). HCN is then produced by dehydrogenation of CH_2NH .

The temperature dependence of the reactions leading to the formation of nitriles still needs to be investigated, as data from Chin et al. (2016) suggests that nitrile formation may be more efficient at higher temperatures. Determining whether $\text{C}\equiv\text{N}$ formation is mainly driven by cosmic rays or VUV irradiation (or alternatively, whether they mainly driven by N_2 or NH_3 chemistry), will allow us to pinpoint the location in the disk where these molecules are primarily being formed. This will have implications for both our understanding of how planets inherit pre-biotically favourable molecules, and of the structure of protoplanetary disks.

1.4 Thesis Motivation and Outline

In this thesis, we focus on the detection and chemistry of nitriles in protoplanetary disks, the direct progenitors to planets. Elucidating the nitrile chemistry in disks is important both to interpret existing astrochemical observations, and to predict the nitrile budget in forming planets and planetesimals. We aim to develop our understanding of nitrile chemistry using both observational and laboratory techniques. Here, we present the first detection of CH_2CN (cyanomethyl) in a planet-forming environment, the protoplanetary disk TW Hya. We characterise its behaviour and constrain its main formation pathway. We supplement these findings with laboratory experiments in which we investigate the photoprocessing of

CHAPTER 1. INTRODUCTION

$\text{NH}_3:\text{C}_2\text{H}_6$, $\text{NH}_3:\text{C}_2\text{H}_4$, and $\text{NH}_3:\text{C}_2\text{H}_2$ ices as these reactions are a potential source of nitriles in different disk environments. The structure that we will follow is outlined below:

In Chapter 2 we introduce the observational methods and we present the first detection of CH_2CN in TW Hya. We use a rotational diagram to constrain the excitation temperature and column density. We also investigate how these quantities change as a function of radius by radially-resolved analysis.

In Chapter 3 we use chemical models from collaborators and the literature to speculate on the potential reasons for the observed morphology and the possible formation and destruction pathways for cyanomethyl. We comment on the efficiency of our reactions and the possible limitations.

In Chapter 4 we introduce the ice experiments and the experimental set up. We investigate the contribution of NH_3 -containing pathway to the abundance of nitriles in astronomical environments. The results of the laboratory experiments are discussed in Chapter 5.

In Chapter 6 we discuss the results of our laboratory experiments and the implications for our understanding of chemical reactions in protoplanetary disks. In Chapter 7 we provide a summary of our findings and our conclusions.

Chapter 2

Observational Methods & Results

Our astrochemical observations were acquired with the Atacama Large Millimeter and submillimeter Array (ALMA). As the name suggests, this is an array of dishes rather than a traditional single-dish telescope. The reason for using an array is that it allows us to increase the spatial resolution without increasing the diameter of the individual dishes. This is advantageous because, as a general rule, the greater the diameter of the primary mirror of a telescope, the greater the resolution of the images. This is especially problematic at long wavelengths since the spatial resolution is proportional to the wavelength. However, building very large mirrors is expensive and difficult as the weight of the mirror causes it to sag and distort, thus affecting the quality of the images. Interferometry uses the distance between antennas, rather than the size of individual telescopes, to obtain higher resolution images. Further information about how interferometry works will be given in §2.1. Our observational data has been collected using the Atacama Large Millimeter/submillimeter Array (ALMA), an interferometer operated by the European Southern Observatory (ESO)

and located on the Chajnantor plateau in the Chilean Andes. More on ALMA in §2.2. The data reduction is discussed in §2.3. We also present and analyse the results and compare them to those obtained by Loomis et al. (2018) on the detection of CH₃CN toward TW Hya with the goal to constrain both their formation pathways.

2.1 Millimeter Interferometry

Interferometry exploits the superimposition of electromagnetic waves (EM) to combine the signal from physically separated telescopes. This allows the creation of an image as if it had been taken by a single telescope with a mirror diameter equal to distance between the two antennas with the greatest separation. The distance between two antennas is known as the baseline. The more baselines are used, the more information one can obtain about the object being studied as it will be seen at multiple resolutions.

The basic principles behind interferometry is the Young’s double slit experiment and the idea that when EM waves interact, they can do so constructively or destructively (Monnier 2003). In Young’s double-slit experiment, monochromatic light from a distant point source goes through a surface with two slits and the resulting pattern is projected on a screen. The experiment is depicted in Figure 2.1.

For a telescope, the slits are representative of the different antennas and the varying baselines will give rise to different patterns of interference fringes, as the spacing is given by:

$$\Delta\Theta = \frac{\lambda}{b} \text{radians} \quad (2.1)$$

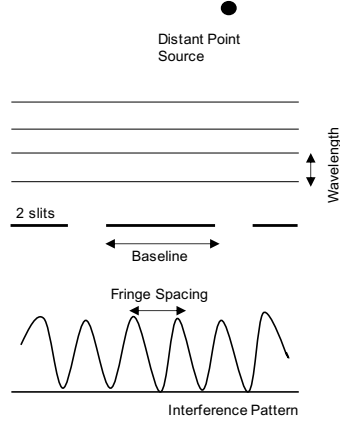


Figure 2.1 Young double slit experiment: light from a distant source passes through two slits and the resulting wave pattern is projected onto a screen. Adapted from Monnier (2003).

(Monnier 2003). The pattern of fringes will also be affected by the size and the shape of the object that is being observed. Subsequently, by combining the observations from of all the antennas and by seeing how the different light signals interfere with each other, an image of the body that is being observed can be reconstructed.

Classical diffraction theory defines the “Rayleigh Criterion” as the resolution of a filled circular aperture of diameter D and it is calculated through the equation:

$$\Delta\Theta_{\text{telescope}} = 1.22 \frac{\lambda}{D} \text{radians} \quad (2.2)$$

(Monnier 2003). For a telescope that uses interferometry, this becomes

$$\Delta\Theta_{\text{interferometer}} = 1.22 \frac{\lambda}{b} \text{radians} \quad (2.3)$$

where b is the baseline. Therefore, the greater the distance between the two furthest antennas, the more detail will be discerned in the source.

2.2 The Atacama Large Millimeter/submillimeter Array

ALMA is an interferometer composed of 66 antennas, which are divided in the 12-m Array, and the Atacama Compact Array (ACA). The distances between the antennas (baseline) varies from ~ 15 m to 16 km. ALMA detects millimeter-submillimeter wavelengths in the range $350\mu\text{m}$ - 3 mm (soon to be 7 mm) which means that cold astronomical objects, such as molecular clouds and protoplanetary disks, are able to be observed as they emit radiation in the aforementioned range. For instance, the disk HL Tau was imaged with unprecedented detail and revealed a pattern of bright and dark rings that shone light on the planet formation process and allowed for better modelling of disk temperature and density structure (ALMA Partnership et al. 2015).

The high resolution and high sensitivity of the telescope come from the 12-m Array. This is the largest component, as it is composed of fifty antennas with 12-m dishes. When all 50 dishes are operating, there are in total 1225 baselines, which allows for an unparalleled resolution. ACA is the smallest component with twelve 7-m antennas, and 4 12-m antennas for single-dish observations (these four comprise the Total Power (TP) Array). An important role of the ACA is to solve the short baseline problem. This is the issue that arises from the fact that it is not possible to pack antennas closer than their diameter, hence without ACA there would be a lack of data at short baselines and at zero, and as a result it would be impossible to image large angular structures. The 7-m antennas cover the range of baselines from 9 m to 30 m, and the TP Array provides coverage from 0 m to about 12 m (ALMA

Partnership et al. 2015).

2.3 Data Collection & Calibration

The observations for this project were taken and calibrated by Dr. Richard Teague as part of ALMA Project 2018.A.00021. The data is split into six different executions: two of which were taken in a compact configuration and the remaining four were taken with a greater baseline range. These observations also used a different number of antennas, ranging from 35 for one execution, up to 48 for others (44, 44, 48, 48, 35 and 47). The compact data was collected on April 4th 2019, with baselines spanning 15 m -500 m, whereas the extended configuration data was collected on September 29th 2019, and the baselines ranged from 15 m-2.62 km. The shorter baseline executions included 41.7 minutes on-source integration while the longer baseline executions used 51.1 minutes on-source for a total on-source time of 4.9 hours. For all six executions the precipitable water vapor (PWV) ranged between 0.46mm and 0.86mm. In both instances, the correlator set up included a single wide frequency divided mode (FDM) window centered on 241.5 GHz to provide access to the continuum for self-calibration as well as 4 narrower windows centered on different molecular lines. The quasar J1037-2934 was used for both bandpass and flux calibration for all executions while the phase calibration was performed with J1147-3812 and J1126-3828 respectively for the short and long baseline data. The six emission lines of CH₂CN, the target molecule of this study, were detected in the continuum window, as well as a single C34^S line.

Initial calibration was performed using the standard pipeline procedure in **CASA**

v5.6.2, and then self-calibrated following the procedure used in the DSHARP program (McMullin et al. 2007; Andrews et al. 2018). All spectral windows were used, masking out any lines in each spectral window. The windows that did not present any lines were then used to find phase solutions, which were then applied to the entire dataset. The executions were aligned to the same phase center and then combined together. All but one execution had flux within 2% of one another, whereas the final long baseline execution showed 10% variation. Therefore, it was rescaled using the `gaincal` task such that the total flux matched that of the other three long baseline executions before combining all six of them together. Finally, the continuum was subtracted using the `uvcontsub`.

The continuum FDM window was imaged using the multi-scale CLEAN algorithm and adopting a Briggs weighting with a robust parameter of 2 (similar to natural weighting) yielding a synthesized beam of $0''.34 \times 0''.32$ at a position angle of 104.8° . The data was imaged at the native spectral resolution of the FDM window of 1.4 km s^{-1} .

2.4 Image Analysis

We detected six CH_2CN transitions with their associated quantum labelling are depicted in Figure 2.2 and their respective properties are described in Table 2.1. CH_2CN has two identical hydrogen atoms and as a result there exist two distinct spin isomers of CH_2CN : ortho- CH_2CN , when the spins of both hydrogen nuclei are parallel to each other and para- CH_2CN , which arises when the hydrogen nuclei spins are anti-parallel. Ortho- CH_2CN have transitions with even values of K_a (the

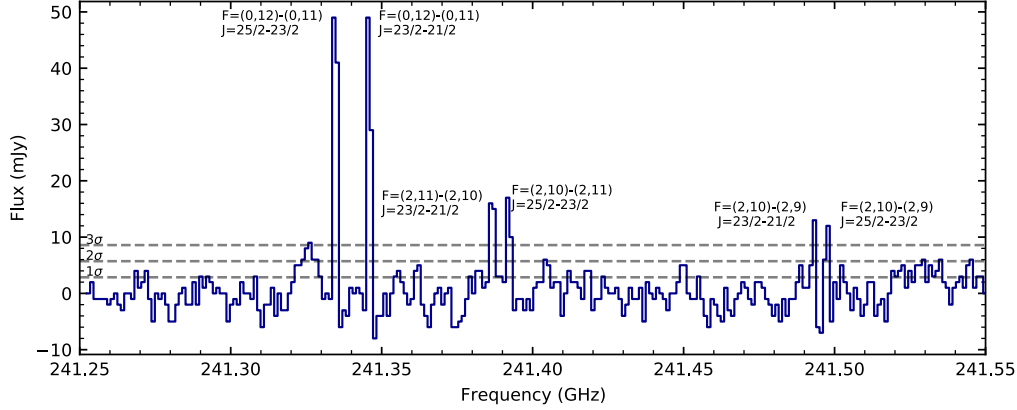


Figure 2.2 Spectrum of the observed CH_2CN transitions. The 6 brightest peaks are shown with their quantum numbers. The signal-to-noise is calculated to be 2.9 mJy. Dashed horizontal lines represent 1σ , 2σ and 3σ noise levels.

projection of the angular momentum along the inertia a axis) and all our transitions are ortho transitions.

The spectrum is useful for the identification of the molecule, but it does not provide direct information about the distribution of the molecule in the protoplanetary disk. Therefore, we also depict the six transitions in integrated intensity maps in Figure 2.3. Since only two of the transitions are robustly detected, we also create a high signal-to-noise map by stacking the transitions together to better visualise the morphology of the molecule (left panel of Fig 2.4).

To better visualize the morphology, we also plot the radial profiles of each of the individual transitions (Fig 2.5) and of the stacked data (right panel Fig 2.4). For this part of the analysis we use two different data sets: the native resolution data and a smoothed data cube. The latter is the original data (native resolution) that has been smoothed by Dr Teague to a lower spatial resolution (from $0''.34 \times 0''.32$ to

Table 2.1. Observed CH₂CN Transitions

N' - N''	K _a	K _c	J' - J''	ν_0 (GHz)	g_u	A_{ul} (s ⁻¹)	$S_{ij}\mu^2$ (D ²)	E_{upper} (K)
12-11	0 - 0	12 - 11	25/2 - 23/2	241.3335423	234	9.62×10^{-4}	1376.0	75
12-11	0 - 0	12 - 11	23/2 - 21/2	241.3458390	216	9.59×10^{-4}	1265.6	75
12-11	2 - 2	11 - 10	23/2 - 21/2	241.3860255	216	9.33×10^{-4}	1230.5	128
12-11	2 - 2	11 - 10	25/2 - 23/2	241.3913950	234	9.36×10^{-4}	1337.7	128
12-11	2 - 2	10 - 9	23/2 - 21/2	241.4925510	216	9.34×10^{-4}	1230.6	128
12-11	2 - 2	10 - 9	25/2 - 23/2	241.4970603	234	9.37×10^{-4}	1337.7	128

Note. — All data for column N'' - N'' through to E_{upper} was obtained from The Cologne Database for Molecular Spectroscopy (CDMS; Müller et al. 2001; Endres et al. 2016).

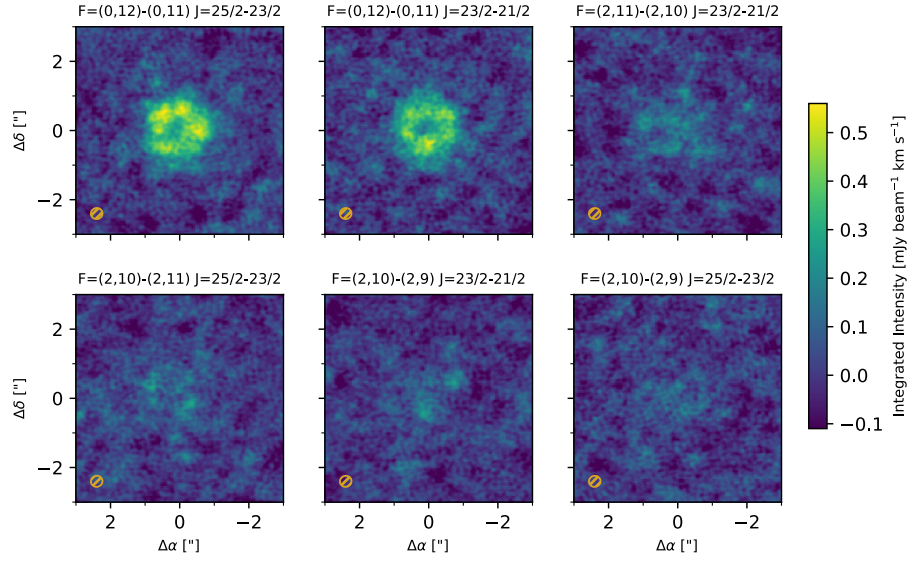


Figure 2.3 Integrated intensity images of individual observed transitions. All the panels share the same intensity scale. The synthesised beam is shown in the bottom left corner. We find σ to be $0.06 \text{ mJy beam}^{-1} \text{ km s}^{-1}$.

$1''.05 \times 0''.83$). This resolution was selected to both boost the SNR, and to match a previous observation of the chemically related molecule CH_3CN , which we will later compare our results against. To obtain the radial profiles in Figure 2.5, we radially bin the integrated flux from each transition into $0.05''$ (~ 3 au)-wide bins. For TW Hya we use a position angle of 152° and an inclination, $i = 5^\circ$ (Huang et al. 2018). The radial profile extraction is carried out once for the native resolution data, for the smoothed spatial resolution data, and for the stacked data at native resolution. As the weaker transitions are more clearly detected in the smoothed images (this can be observed in Fig 2.5), we use the smoothed images all quantitative analysis, while we use the native resolution profiles for the morphology characterization in §2.5.

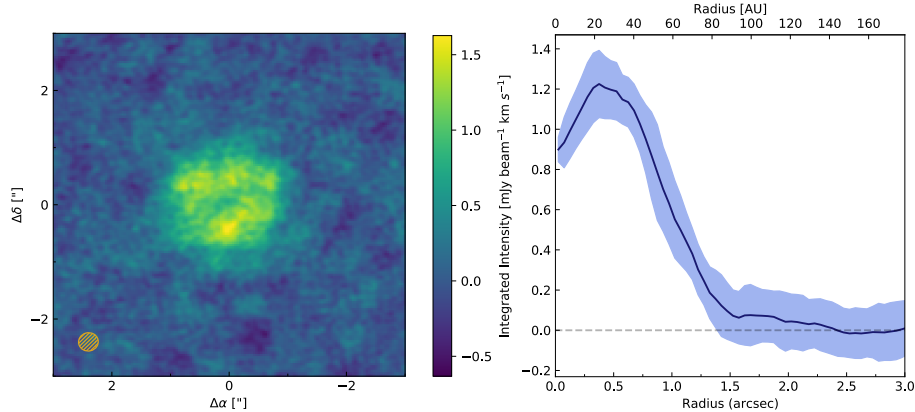


Figure 2.4 Left panel: Integrated intensity map made from the stacked 6 transitions. The noise is calculated to be $0.14 \text{ mJy beam}^{-1} \text{ km s}^{-1}$. Right panel: the azimuthally averaged integrated intensity radial profile obtained from the stacked native resolution data. Shaded areas represent 1σ uncertainties, where σ represents the standard deviation in each radial bin.

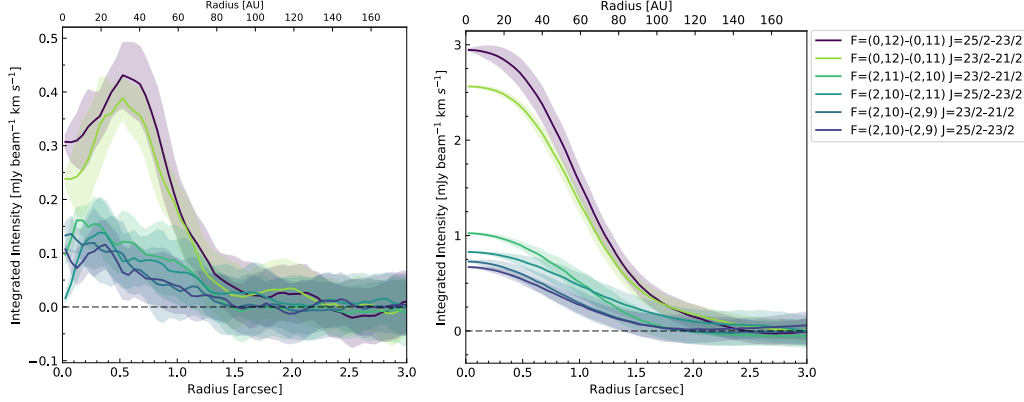


Figure 2.5 The integrated intensity radial profile obtained from native and lower spatial ("smoothed") resolution data (left and right panel respectively). Shaded areas represent 1σ uncertainties, where σ represents the standard deviation in each radial bin.

2.5 Morphology

The integrated intensity maps in Fig 2.3, Fig 2.4, and the native resolution radial profile, seem to imply a ring morphology. Therefore, we fit the native resolution stacked radial profile to a Gaussian to infer the ring width and center. This fit is shown in Figure 2.6. We find the ring center to be at $0.4''$ (~ 24 au) and the full width half maximum to equal $1.1''$ (~ 69 au). We also note that there is some excess emission between $1.5''$ and $2.5''$, however, further observations are needed to characterise it and understand its origins.

Loomis et al. (2018) found that CH_3CN exhibited a centrally-peaked morphology at the resolution of our smoothed data. We obtain a similar result when using the smoothed data cube, as shown in 2.5. The similar distribution suggests that there is a chemical link between the two molecules, which will be further explored in later

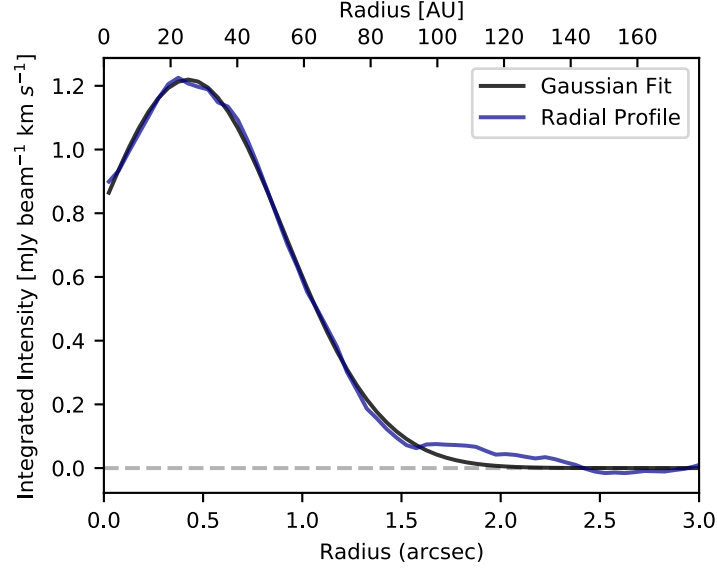


Figure 2.6 The native radial profile of the stacked transitions fitted with a Gaussian to infer the ring width and position of the center.

chapters.

2.6 CH₂CN Excitation Analysis

To constrain the physical conditions of the CH₂CN gas we use a rotational diagram. This allows us to obtain the rotational temperature, T_{rot} , and the column density, N_{tot} , for CH₂CN. This method implicitly assumes that the molecule excitation can be described by a single temperature, that the molecules are in local thermodynamic equilibrium (LTE), and that the source fills the beam (Goldsmith & Langer 1999). The resulting T_{rot} is unlikely to represent the excitation temperature for all molecules, however, it provides an average temperature for the region from which molecular emission arises (Bisschop et al. 2007).

2.6.1 Method

For the calculation of T_{rot} and N_{tot} we use the approach described by Goldsmith & Langer (1999). We constrain these values using the equation:

$$\ln \frac{N_u}{g_u} + \ln C_\tau = \ln N_{tot} - \ln Q(T_{rot}) - \frac{E_u}{kT_{rot}}, \quad (2.4)$$

where N_u is the the column density of molecules in the upper state of each transition, C_τ is the optical depth correction factor, and $Q(T_{rot})$ is the molecular partition function and E_u is the upper state energy. For the molecular partition function, we use known values from The Cologne Database for Molecular Spectroscopy (CDMS; Müller et al. 2001) to linearly interpolate our values of interest. The resulting function is shown in Figure 2.7. It is important to note that degeneracies due to the hyperfine structure are included in the calculation, therefore we do not need to perform further corrections to $Q(T_{rot})$.

We calculate the N_u for each transition through the equation:

$$N_u = \frac{4\pi S_\nu \Delta v}{A_{ul} \Omega h c}, \quad (2.5)$$

where S_ν is the flux density, A_{ul} is the Einstein coefficient, Δv is the width of the two channels that we used for integration (each 1.4 km s^{-1} wide) and Ω is the solid angle subtended by the source, which in this instance is equal to 1.06×10^{-10} steradians.

The calculated N_u value needs to be adjusted to take into consideration the optical thickness of the lines. For this, we use the optical correction factor C_τ given by:

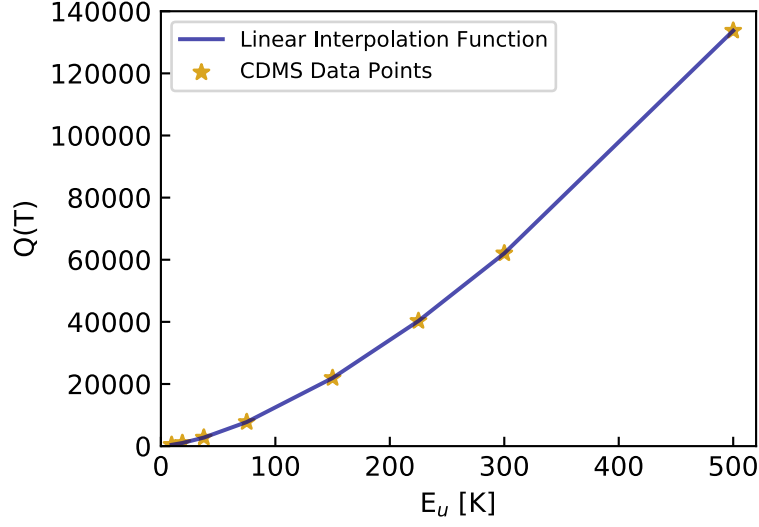


Figure 2.7 The function used for linear interpolation of the partition function is shown in dark blue. The data points (golden crosses) are taken from CDMS (Müller et al. 2001).

$$C_\tau = \frac{\tau}{1 - e^{-\tau}}. \quad (2.6)$$

where the optical depth, τ , can be related to the upper level population through the equation:

$$\tau_{ul} = \frac{A_{ul}c^3}{8\pi\nu^3\Delta v}N_u(e^{h\nu/kT_{rot}} - 1). \quad (2.7)$$

Given that our emission is dominated by Doppler broadening, the line width, Δv , is given by

$$\Delta v = \sqrt{\frac{2kT_{rot}}{m_u m_H}}, \quad (2.8)$$

with m_u being the molecular weight of CH_2CN (40 g/mol) and m_H being the mass of a hydrogen atom.

We create a model that relates N_u , C_τ and Δv to Equation 2.4 and we derive the values of T_{rot} and N_{tot} by matching the observed N_u/g_u values. We use Scipy's `curve_fit` function to find the minimum χ^2 and find the best estimate of our desired parameters (Jones et al. 2001).

2.6.2 Disk-Averaged Analysis

In this section, we will calculate the average column density and rotational temperature across the disk up to a radius of $2.5''$. At this radius of the disk, approximately all the the flux from all the transitions reaches 0 as shown in the right panel of Figure 2.5. We first calculate the value of S_ν (flux density) so that we can obtain the N_u value (number of molecules in the energy level) for each of the transitions using Equation 2.5. In order to calculate S_ν , we extract the cube data for each detected transitions (by singling out the channels in the data cube where we observe signal), find the mean and standard deviation of the cube data for the 6 detected lines since each detection was across two channels and finally, we bin these parameters into a single $2.5''$ -wide annulus. Once we have obtained N_u , we can use Equation 2.4 to plot our disk-averaged rotational diagram ($\ln(N_u/g_u)$ against the upper state energies, E_u), shown in Figure 2.8. The slope and the y -intercept of the resulting graph respectively represent $-T_{rot}^{-1}$ and N_{tot} . The standard deviation of the cube data is propagated to obtain the errors in S_ν , N_u and N_u/g_u in Equation 2.4. From the disk-averaged rotational diagram in Figure 2.8 we obtain a disk-averaged

rotational temperature of 38 ± 5 K and a disk-averaged total column density of $(3.5 \pm 0.3) \times 10^{12} \text{ cm}^{-2}$ for ortho-CH₂CN up to a radius of $2.5''$. As described in Le Gal et al. (2017), for a molecule containing 2 identical Hydrogen nuclei, such as CH₂CN, we expect a statistical ortho/para ratio of 3:1, and therefore we infer a total column density for CH₂CN of $4.7 \times 10^{12} \text{ cm}^{-2}$. We represent the uncertainties by showing plotting the rotational diagrams using random best-fit parameters. These are obtained by assuming that our parameters follow a Gaussian distribution with mean at the best-fit parameter (i.e., N_t or T_{rot}) and standard deviation equal to error in these parameters. Under this assumption, we can draw random pairs of N_t and T_{rot} and plot them near our best-fit line to better visualise the uncertainties.

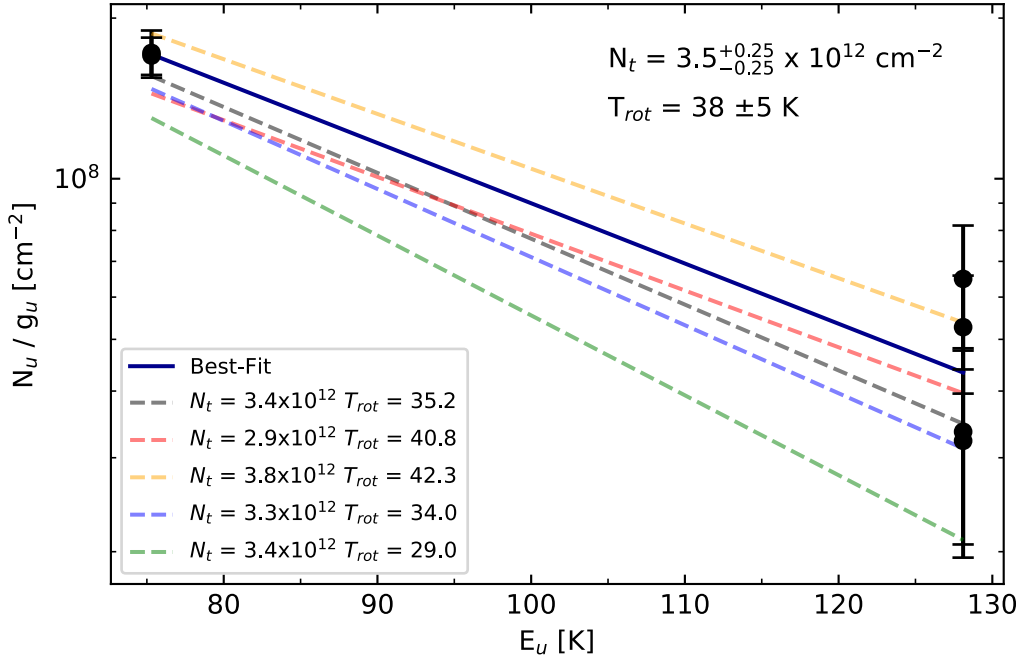


Figure 2.8 Ortho-CH₂CN disk-averaged rotational diagram, calculated from disk-averaged flux intensities out to a radius of $2.5''$. Random draws of best-fit parameters are also shown to depict the uncertainties.

CHAPTER 2. OBSERVATIONAL METHODS

We repeat the rotational diagram fitting out to a radius of $1.75''$. As shown by Fig 2.5, the flux from the weaker emission lines is almost completely lost at this radius. Therefore, using this smaller radius allows us to calculate the N_{tot} and T_{rot} in the regions of the disk where there is substantial CH_2CN emission. In addition to this, Loomis et al. (2018) present their results on CH_3CN up to a radius of $1.75''$, which means that we are able to make a more direct comparison between these two molecules. The results from the rotational diagram out to a radius of $1.75''$ confirm what can be observed from the radial profiles (Fig 2.5, 2.4): the outer radii of TW Hya contribute very little to the column density. In fact, the rotational diagram up to a radius of $1.75''$ yields a column density of $(8.4 \pm 0.7) \times 10^{12}$ ($(6.3 \pm 0.5) \times 10^{12}$ for ortho- CH_2CN) cm^{-2} , while the rotational temperature remains relatively constant at 40 ± 5 K. We note that our excitation temperature is similar to the CH_3CN excitation temperature of $32.7^{+3.9}_{-3.4}$ K in the same disk (Loomis et al. 2018). The column density of CH_3CN , $1.82^{+0.25}_{-0.19} \times 10^{12}$, is ~ 5 times lower than our observed CH_2CN 's N_{tot} .

From our rotational diagrams we can see that all of our data points are concentrated at $E_u = 75\text{K}$ and $E_u = 128\text{K}$ and while the N_u/g_u values at 75 K are almost equivalent, we observe a large scatter in values at 128 K. This means that there could be a lot of variation in the slope of the line, and by association, the calculated T_{rot} may be more uncertain than the errors would suggest.

To test the validity of our calculated T_{rot} we plot several rotational diagrams using the same method as §2.6.1, but we keep the temperature constant at either 20 K, 30 K, 40 K or 70 K. The results are shown in Figure 2.9. From this, we are able to rule out temperatures around 20 K and 70 K as potential T_{rot} , and confirm that our

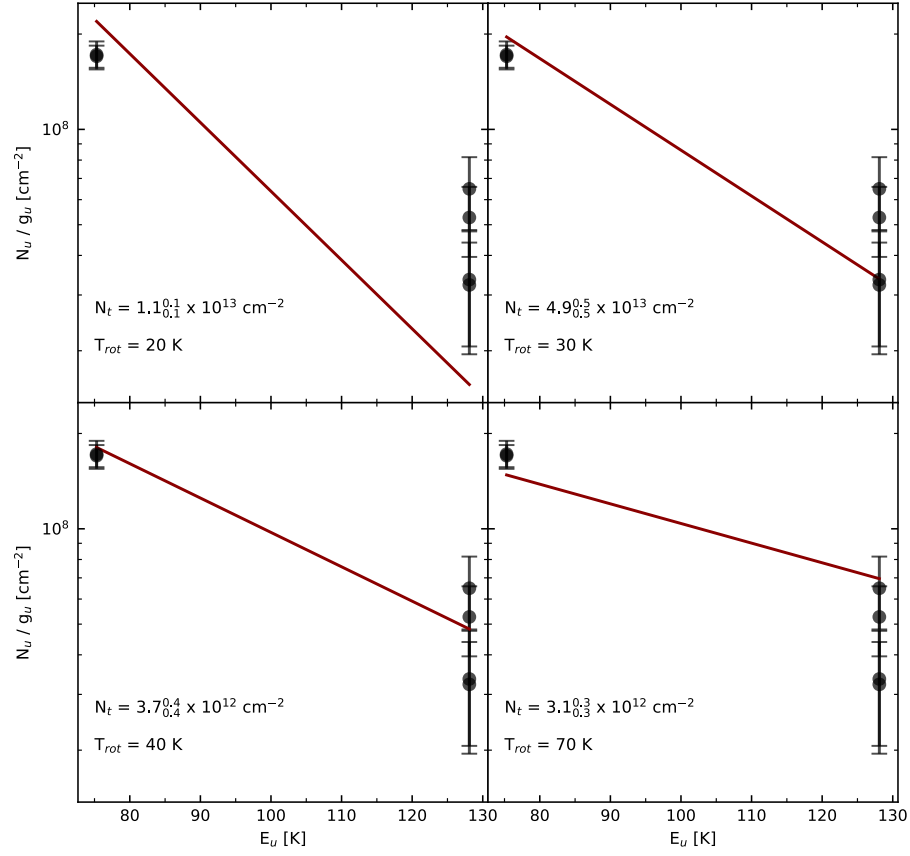


Figure 2.9 Rotational diagrams plotted using the method described in §2.6.1, but keeping the rotational temperature fixed at 20K (A), 30K (B), 40K (C) and 70K (D).

obtained T_{rot} of $38 \pm 5\text{K}$ is indeed a very good fit to our data. This suggests that while our calculated uncertainty is 5 K, the systematic uncertainty of our data is likely closer to ~ 10 K. Additional modelling efforts are needed to further constrain the rotational temperature. While there is still some uncertainty associated with our T_{rot} , our N_{tot} remains fairly constant regardless of the T_{rot} used, hence implying that the total column density for ortho-CH₂CN is well constrained.

Finally, we calculate the optical depth, τ , of our transitions. Even though we included this parameter in the fitting of our rotational diagram, we can now use our obtained T_{rot} to ensure that we have optically thin transitions. In all cases, we obtained a value of $\tau \ll 1$, with values of range 4×10^{-4} to 3.4×10^{-3} . When taking into consideration the additional systematic uncertainty, we obtain an accepted τ range of Therefore, our detected transitions were of negligible optical thickness and in hindsight, could have been omitted from the rotational diagram calculation.

2.6.3 Radially-resolved Analysis

Next, we investigate how N_{tot} and T_{rot} change as a function of radius. To do so, we create $0.05''$ -wide bins up to a radius of $2.5''$ (for a total of 50 bins) as we had previously done for the radial profiles and for the disk-averaged excitation analysis in §2.6.2. The mean and standard deviation of the cube data in each of the 50 bins that we created is calculated. We can then obtain the flux density, S_ν in each of these bins. The S_ν value can then be used in Equation 2.5 and then in Equation 2.4 to obtain a total column density and rotational temperature for each $0.05''$ interval in disk radius. The resulting N_{tot} and T_{rot} are then plotted against the radius of the

disk, as shown in Figure 2.10, to show how these two parameters vary across the disk.

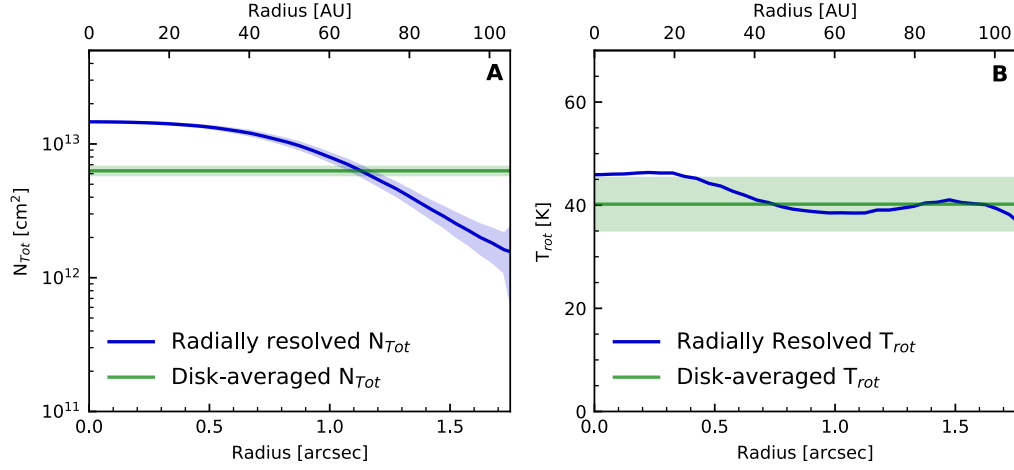


Figure 2.10 Panels A & B: respectively the radial profiles of the ortho-CH₂CN total column density and the rotational temperature. The colour dark blue indicates radially resolved values, whereas green is used for values we obtained from disk-averaged analysis. Shaded areas represent 1 σ uncertainties.

Figure 2.10A shows that N_{tot} decreases from 5×10^{13} to 0.6×10^{13} across the radius of the disk. This is consistent with the disk-averaged column density. The T_{rot} (Fig 2.10B) ranges between 45 and 37 K, which is consistent with the disk-averaged T_{rot} (38 ± 5 K).

Chapter 3

Discussion I: CH_2CN in the TW Hya Protoplanetary Disk

3.1 $\text{CH}_2\text{CN}/\text{CH}_3\text{CN}$ Ratio & Disk Models Results

We begin exploring the chemistry of methyl cyanide by using chemical models by Le Gal et al. (2019b) to compare the predicted abundance of both CH_2CN and CH_3CN at all radii in the disk. The model has been modified to fit the physical parameters of TW Hya, shown in Table 3.1. Another parameter to take into consideration is the C/O ratio of the disk. Carbon and oxygen atoms primarily reside in the disk as CO, however, photo-dissociation reactions cause the breakdown of this molecule into C and O. The majority of the resulting products go on to reform CO except for a small percentage that takes part in chemical reactions that lead to the formation of complex nitriles (Bergin et al. 2014). The importance of having a C/O ratio above unity has been shown by Bergin et al. (2016), who demonstrated that if

this condition is not met, chemical models are unable to reproduce the observed hydrocarbon abundance in both the disks of DM Tau and TW Hya. This was further confirmed by Miotello et al. (2019), as their model failed to reproduce the observed C_2H fluxes in a sample of Lupus sources unless a C/O ratio ≥ 1 was used. Therefore, for the purpose of our model, we adopt a C/O ratio of 1. The resulting predicted radial profiles for CH_3CN and CH_2CN are shown in Figure 3.1.

Table 3.1: Physical parameters used for the disk chemistry modeling

Parameters	TW Hya ^a
Stellar mass: M_\star (M_\odot)	0.8
Characteristic radius: R_c (AU)	10
Density power-law index	1.5
Midplane temperature at R_c	20
Atmosphere temperature at R_c	104
Surface density at R_c	0.79
Temperature power-law index	0.55
Vertical temperature gradient index	2
UV Flux ^b at R_c (in Draine (1978)’s units)	3400

^a Andrews et al. (2012)

^b Herczeg et al. (2004)

Overall, the model is in good accordance with our observations as it predicts that CH_2CN is more abundant than CH_3CN at all radii. However, while our observations show a CH_2CN/CH_3CN ratio of ~ 5 , the ratio from the model is one order of magnitude larger. In addition to this, Le Gal et al. (2019b) model seems to under-predict the abundance of CH_3CN . This suggests that there may be some

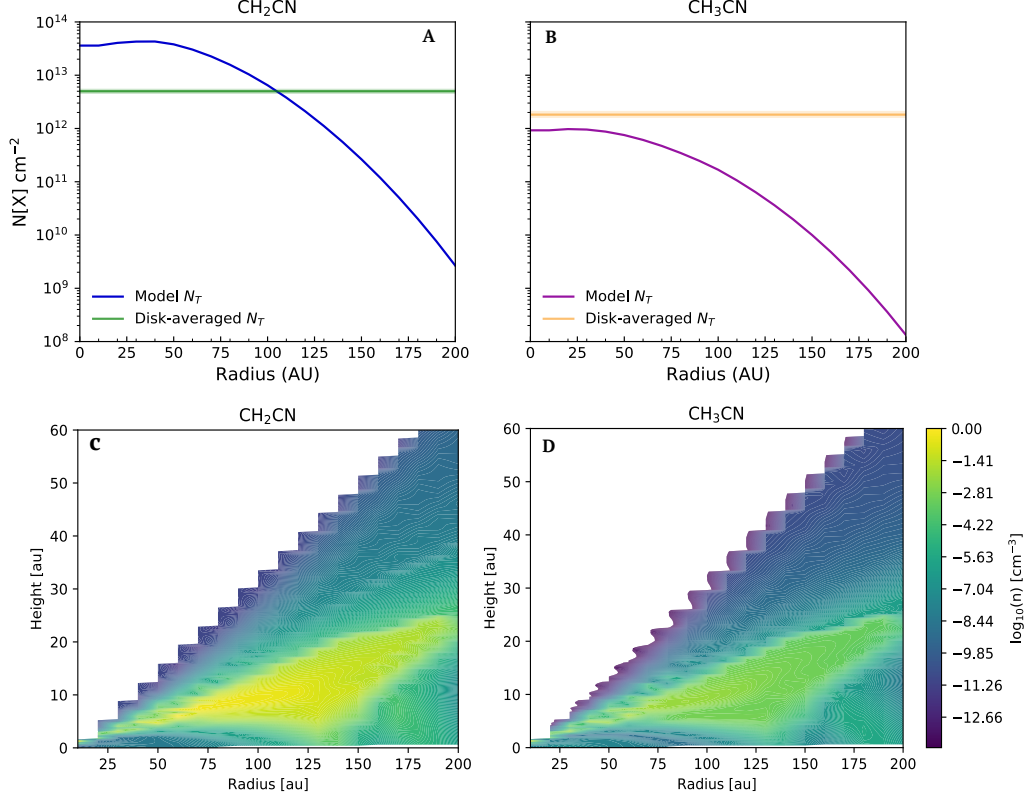


Figure 3.1 Total column densities of CH_2CN (Panel A) and CH_3CN (Panel B) as a function of radius, predicted by the chemical models of Le Gal et al. (2019b) that we adapted to TW Hya (blue and purple curve for CH_2CN and CH_3CN , respectively). We use our derived column density for CH_2CN (green horizontal line in Panel A) and the values reported by Loomis et al. (2018) for CH_3CN (orange horizontal line in Panel B). Panel C and Panel D show the abundance of CH_2CN and CH_3CN respectively as a function of radius and height. We are able to see that the region of highest emission is between ~ 50 - 110 au and a height of ~ 10 au.

formation pathways for CH_3CN that are missing from the model. We attempt to bridge this gap between the predicted and observed CH_3CN abundance by investigating potential CH_3CN formation pathways in the experimental component of this thesis. Specifically, we look at cold, grain-surface photoprocessing of NH_3 and hydrocarbons (C_xH_y). More detailed astrochemical models are needed to understand the discrepancy that exists between the predicted and observed CH_3CN abundance. On the other hand, the column density of CH_2CN is well represented, which suggests that this molecule is well constrained by Le Gal et al. (2019b)’s chemical model. In addition to this, both the models and the observations show that most of the emission of CH_2CN arises from the inner radii of the disk (within the first 50 au) which suggests that this molecule could be incorporated into nascent planets as planet-formation begins close to the central star.

Figure 3.1C and D show the distribution of CH_2CN and CH_3CN (given as n , which represents the volume density of the species) as a function of the height and radius of the disk as predicted by Le Gal et al. (2019b)’s model. This allows us to pinpoint the location of the emission with respect to height above the midplane and compare the location and strength of the emission of the two nitriles. For both molecules, we find that the brightest emission comes from a radius of 50 au-110 au and a height of 10 au. CH_2CN emission appears to be approximately one order of magnitude stronger than that of CH_3CN at all radii. This is also supported by our observations. One difference between Le Gal et al. (2019b)’s models and our observations is that we see most of the CH_2CN emission originating from the first 25 au of the disk (Figure 2.5 and 2.4), whereas the models predict that the brightest emission would come from a broader, further out region of the TW Hya disk (~ 50 -110 au). This

implies that these models need to be refined to better represent the distribution of CH_2CN in the disk. Constraining the formation pathways that lead to the formation of both CH_3CN and CH_2CN would allow us to pin-point where in the disk these reactions happen and therefore, where we would expect the most emission. We will focus on potential candidates for these reactions in the next component of this thesis.

3.2 CH_2CN Radial Morphology

When imaged at native resolution ($0.3''$), CH_2CN appears to be distributed in a $1.1''$ -wide ring that peaks at $0.4''$ (as shown by Figure 2.5 and 2.4). The chemical model results for CH_2CN shown in Figure 3.1, seem to replicate the morphology that we observed in Figure 2.10. This suggests the presence of a ‘Goldilocks zone’ for the dominant CH_2CN formation pathway, where the observed morphology can be attributed to the balance between formation and destruction reactions under fiducial disk conditions. In this region of the disk, the chemical environment (i.e. optimal UV radiation flux or temperature of the disk molecular layer) may be particularly favourable for the production of CH_2CN .

While this chemical ‘Goldilocks zone’ (a region of the disk where the chemical environment is particularly suited to the production of CH_2CN) may be sufficient to explain why CH_2CN appears as a ring, it is still interesting to consider other possible causes. The ring morphology seen in both the model and observations is not unique to cyanomethyl, as CN and C_2H are also analogously distributed in TW Hya, however, their rings peak at considerably larger radii at ~ 45 au ($0.75''$) and 60 au ($1''$), respectively (Teague & Loomis 2020; Bergin et al. 2016). This nested structure

of potentially chemically related species (see Table 3.3 for more) provide clues as to what processes are regulating the abundance of these molecules in TW Hya. One possible cause of rings in disks is changes in the local disk environment at the edge of the dust continuum, which occurs at ~ 60 au in TW Hya (Andrews et al. 2012). At radii smaller than 60 au, the dust acts as a barrier and therefore it is harder for VUV-irradiation from the central star and the ISRF to reach deep into the layers of the disk. On the other hand, beyond the edge of the dust continuum there VUV photons will penetrate further into the disk layers, thus leading to greater photochemistry, photodissociation and non-thermal desorption (Förstel et al. 2017). Removal of the dust mass beyond the continuum also contributes to an overall increase in the temperature of the disk, which means that the conditions become sufficiently warm to increase CO desorption from the surface of grains, thus resulting in an increase of C and O available for chemical reactions (Cleeves 2016). However, the peak of the CH_2CN emission occurs before the edge of the dust continuum and therefore we are not able to attribute the observed ring morphology to this effect.

Another possible explanation for the observed CH_2CN ring morphology is the abundance of gas-phase C and O, as chemical models by Du et al. (2015) have shown that the production of nitriles in the TW Hya disk is affected by the presence of these atoms. In fact, the abundance of N-H and C-N containing molecules increased by up to ~ 2 orders of magnitude in a situation where CO depletion (gas-phase C and O freeze-out onto the surface of grains) was taken into consideration. In addition, in models without depletion, the observed abundance of CO and H_2O could not be replicated, thus further emphasising the importance of this process for the chemistry in the disk. One disk location that may present a rapid change

in the C and O abundance is the CO snowline, where CO ice sublimates back into the gas-phase therefore increasing the abundance of C available for nitrile formation reactions. In the case of TW Hya, the CO depletion zone is found at 17-30 au, which is consistent with our finding of the CH_2CN peak emission being at 24 au (Schwarz et al. 2016; Qi et al. 2013). Exterior to the snowline, the C and O would reside on the surface of the grains in the form of CO and therefore they would not affect the chemistry of nitriles.

3.3 CH_2CN Chemistry

We use the astrochemical models by Le Gal et al. (2019b) to constrain the possible formation and destruction pathways for CH_2CN . The results are summarised in Table 3.3. The rates of reaction are calculated differently depending on the type of reaction in question and we reproduce these from the Kinetic Database for Astrochemistry available at <http://kida.astrophy.u-bordeaux.fr> (Wakelam et al. 2012). For the gas-phase formation reactions we use the Modified Arrhenius Equation

$$k(t) = \alpha \left(\frac{T}{300} \right)^\beta e^{-\frac{\gamma}{T}}; \quad (3.1)$$

whereas we calculate the ion-polar rate coefficient using the Su-Chesnavich capture approach, as follows:

$$k(t) = \alpha\beta(0.62 + 0.4767\gamma \left(\frac{T}{300} \right)^{0.5}) \quad (3.2)$$

(Woon & Herbst 2009). Finally, the rates for the photodissociation reactions are computed through the equation:

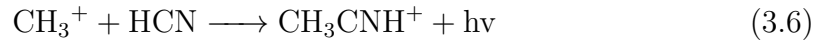
$$k(t) = \alpha e^{-\gamma A_v}, \quad (3.3)$$

where A_v is the visual extinction (Draine 1978; van Dishoeck 1994).

The similarities between the morphology of CH_3CN and CH_2CN suggest a chemical link between these two molecules. In fact, both of these species can be produced on the surface of ice grains through the rearrangement of CN radicals, as follows:



(Herbst 1985). This pathway suggests that the rate of formation of these molecules will be dependent on the abundance of CN and the relative abundance of CH_2 and CH_3 on the surface of the grains. The similarities in the chemistry of acetonitrile and cyanomethyl extend beyond surface reactions as both of these molecules can be formed through the electronic dissociative recombination of CH_3CNH^+ . The full pathway, including the formation of the charged intermediate, is given by:



. However, we propose that the main formation pathway for CH_2CN occurs on the surface of grains because our chemical model predicts a ratio of $\text{CH}_2\text{CN}/\text{CH}_3\text{CN}=0.5$

for the electronic dissociative recombination reaction, whereas our observations have shown that the true ratio between the two species is $\gg 1$. A similar conclusion was made with respect to CH_3CN by (Le Gal et al. 2019a) and (Loomis et al. 2018). Grain-surface reactions are poorly understood both from an experimental point-of-view and a theoretical one and therefore more data is needed to reach a more substantial conclusion. We attempt to shed more light on these issues using the laboratory studies that we have conducted as part of this thesis, which will be discussed in the upcoming sections, and will allow us to put more constraints on the formation and destruction pathways for nitriles such as CH_2CN and CH_3CN .

Table 3.2. Formation and destruction pathways for CH_2CN

Reaction	Reactants	Products	Mechanism	α [$\text{cm}^3 \text{s}^{-1}$]	β	γ	k rate type
Formation	CN	$\text{CH}_3 \longrightarrow \text{H}$	Neutral-Neutral	1.00(−10)	0.00	0.00	(1)
	N	$\text{C}_2\text{H}_3 \longrightarrow \text{H}$	Neutral-Neutral	6.40(−11)	0.17	0.00	(1)
	C	$\text{CH}_2\text{NH} \longrightarrow \text{H}$	Neutral-Neutral	1.00(−10)	0.00	0.00	(1)
	CH_3CN^+	$e^- \longrightarrow \text{H}$	DR ^a	2.00(−7)	−0.50	0.00	(1)
	CH_3CNH^+	$e^- \longrightarrow 2\text{H}$	DR ^a	8.00(−8)	−0.50	0.00	(1)
Destruction	s-CN^b	$\text{s-CH}_2^b \longrightarrow \text{CH}_2\text{CN}$	Grain Surface				
	CH_2CN	$\text{C}^+ \longrightarrow \text{C}$	Ion-Polar	1.00	1.61(−9)	5.81	(2)
	CH_2CN	$\text{H}_3^+ \longrightarrow \text{H}_2$	Ion-Polar	1.00	2.94(−9)	5.81	(2)
	CH_2CN	$\text{h}\nu \longrightarrow \text{CN}$	Photodissociation	1.56(−9)	0.00	1.95	(3)
	CH_2CN	$\text{h}\nu \longrightarrow \text{CH}_2\text{CN}^+ \text{ e}^-$	Photodissociation	5.29(−10)	0.00	3.11	(3)
	CH_2CN	$\longrightarrow \text{s-CH}_2\text{CN}^b$	Freeze-out				

Note. — Table showing all the possible formation and destruction pathways of CH_2CN based on the astrochemical disk model by Le Gal et al. (2019b). The rates of reactions are reproduced from the Kinetic Database for Astrochemistry available at <http://kida.astrophy.u-bordeaux.fr>

(Wakelam et al. 2012).

^aDR = Dissociative Recombination

^bs- indicates solid-state reactions, i.e. reactions occurring on the surface of grains.

Chapter 4

Experimental Methods

In this Chapter, we discuss the VUV-irradiation experiments, as well as the experimental set-up. Our aim in these experiments is to begin to understand how nitriles are formed in protoplanetary disks. To this end, we expose $\text{NH}_3\text{:C}_x\text{H}_y$ mixtures to VUV-irradiation for 6 hours at 30 K, 40 K and 50 K. Our chosen hydrocarbons are C_2H_6 (ethane), C_2H_4 (ethylene) and C_2H_2 (acetylene).

4.1 SPACE CAT

We use SPACE CAT (Surface Processing Apparatus for Chemical Experimentation to Constrain Astrophysical Theories) in the Öberg Astrochemistry Laboratory, shown in Figure 4.1, to simulate the conditions found in the interstellar medium. A more detailed explanation of this apparatus can be found in Lauck et al. (2015). SPACE CAT consists of a 13-inch spherical stainless steel ultrahigh vacuum (UHV) chamber (custom-made, Pfeiffer Vacuum), evacuated by a Pfeiffer Turbo

CHAPTER 4. EXPERIMENTAL METHODS

HiPace 400 pump backed by a DUO 10 M rotary vane pump to a base pressure of $\sim 5 \times 10^{-10}$ mbars at room temperature.

Figure 1. from CO DIFFUSION INTO AMORPHOUS H₂O ICES
 null 2015 APJ 801 118 doi:10.1088/0004-637X/801/2/118
<http://dx.doi.org/10.1088/0004-637X/801/2/118>
 © 2015. The American Astronomical Society. All rights reserved.

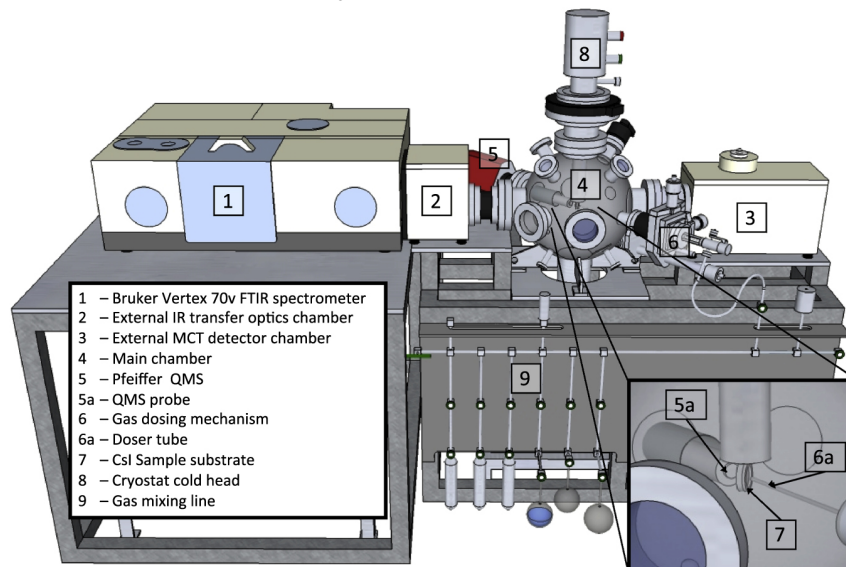


Figure 4.1 Experimental Set-Up in the Öberg Astrochemistry Laboratory in the Harvard & Smithsonian Center for Astrophysics. Gases are deposited in the main chamber (4), their composition is measured using the QMS (5), and their infra-red spectra are collected in (3). Credit: Lauck et al. (2015).

At the center of the chamber, the gases are deposited on a 2-mm thick IR transparent CsI substrate with a 19 mm clear view, mounted on a nickel-plated copper sample holder using silver gaskets, which ensures good thermal contact. The temperature of the ices is controlled by a closed cycle He cryostat (Model CS204B, Advanced Research Systems, Inc.), which can cool down the substrate to 11 K. The cryostat works through a cold tip connected to the sample holder, and the temperature is

CHAPTER 4. EXPERIMENTAL METHODS

controlled via a combination of silicon diode sensors (one near the substrate and one near the heater) and a thermofoil heater. The sensors and the heater enable temperature control using the temperature controller (LakeShore Model 335) which allows temperatures in the range 12 K to 350 K. The CsI substrate can be rotated 360° without breaking the vacuum due to the placement of the cryostat on the top port of the chamber via a differentially pumped UHV rotary seal (Thermionics RNN-400). This means that the ices can face the different analysis instruments, as shown in Figure 4.2, depending on what is required by the experimental procedure. The nominal position for the IR spectrometer is at 225°, but the irradiation is carried out at 180° so the sample is rotated to face the UV lamp, whereas during dosing the sample is rotated to 90° so that we can take IR spectra and monitor the growth of the ice in real time.

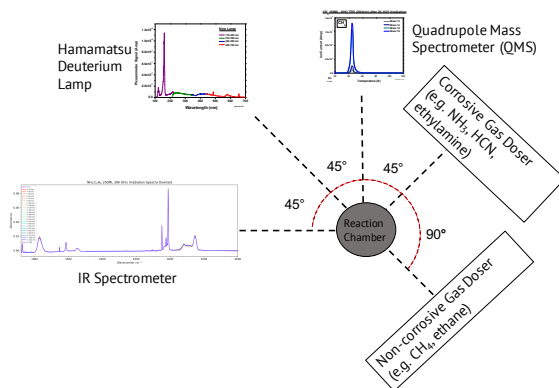


Figure 4.2 Schematic depiction of the internal chamber of SPACE-CAT. The CsI substrate can be rotated to face non-corrosive gas doser (0°, corrosive gas doser (90°), QMS (135°), Deuterium lamp (180°), and IR spectrometer (225°).

The deposition of ices occurs via an independently pumped gas-line (base pressure lower than 10^5 mbars) using a gas doser, which can be positioned 1-90 mm from the

CHAPTER 4. EXPERIMENTAL METHODS

substrate, a precision leak valve (MDC vacuum), and a deposition tube (4.8 mm diameter, 14 inches long). The deposition tube is connected to a gas line which is differentially pumped to 7×10^{-4} mbars. The line can be equipped with bulbs and stainless steel containers containing the gases needed, and a large number of valves means that once the different gas mixture components are in the gas-line they can be mixed prior to dosing into the UHV chamber.

The additional components of the apparatus relevant to our experiments are: a Bruker Vertex 70v spectrometer for infrared spectroscopy, a Pfeiffer quadrupole mass spectrometer (QMG 220M1, mass range 1–100 amu, and resolution of 0.5 amu), as well as a Deuterium lamp (not pictured) positioned at 180° with respect to the non-corrosive gas doser (which we will take to be 0°). The IR beam from the IR spectrometer is focused onto the substrate by a set of custom made mirrors inside the interference chamber and it is refocused on the MCT detector (cooled using liquid nitrogen). All the components of the spectrometer are pumped to 2 mbars to avoid atmospheric interference with the ice spectra. The QMS is positioned 40 mm off the CsI substrate and its main role is to monitor the composition of the gases inside the chamber and to complement the IR analysis of the ice composition. For our experiments, it is particularly useful to check the composition of the ices that are being deposited following completion of an irradiation experiment. We do this through a Temperature Programmed Desorption (TPD) experiment, which involves the controlled sublimation of the ices into gas form so the products of our experiments can be detected and further identified.

4.2 VUV Photoprocessing

We irradiate our ice samples using a H₂:D₂ Hamamatsu L11798 lamp. The spectral profile is shown in Figure 4.3. For the purposes of our experiments, we focus on the <200 nm component of the lamp, as this is the wavelength range that is relevant for dissociation of small molecules like NH₃ and our 2C s. In this wavelength range, most of the emission comes from the ~160 nm component (which corresponds to the emission of molecular deuterium), with a smaller contribution (<15% of the 160 nm flux) from wavelengths in the Ly α range.

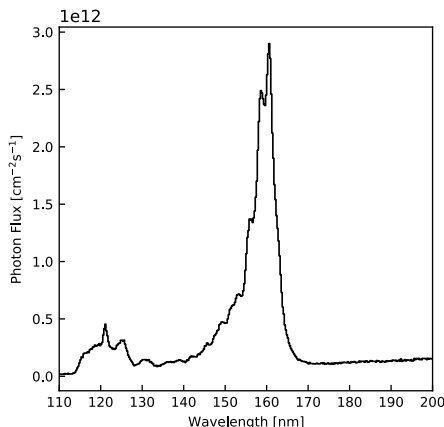


Figure 4.3 The spectral profile of the Hamamatsu L11798 lamp used during our experiments. We are interested in VUV emission, which corresponds to wavelengths <200 nm.

The flux at the sample holder is measured using a NIST-calibrated AXUV100G photodiode. The uncertainty for the flux measurement is $\approx 5\%$. This is for the whole range of emission of the lamp, however, our observed chemistry is driven by <200 nm photons. Therefore, in order to measure the VUV component of our lamp we first calculate the flux >200 nm by irradiating using a MgO window. We then subtract

the flux obtained from the total flux. Because of this subtraction, the uncertainty in the flux in the VUV regime is $\approx 10\%$.

4.3 Analytical Techniques

4.3.1 Infrared Spectroscopy

The IR spectrometer is used to check the ice thickness, composition, and morphology by taking absorption transmission spectra in the range $4000\text{-}600\text{ cm}^{-1}$. The spectra are generated and recorded using the external software OPUS. In addition to this, we take background spectra at every position (90° , 180° , and 225°) before dosing. These are automatically subtracted from the spectra that we take during the course of the experiments. To further correct the spectra, we subtract the baseline by applying a first-order polynomial correction to our spectra. We do this by using the `polyfit` and `polyval` features on Python.

During dosing, we estimate the thickness of the ices using the estimated flow rate and time elapsed since the start. Following deposition, we acquire an infrared spectrum and use this to calculate the number of ice monolayers. We do this by using the formula

$$N(X) = \frac{1}{A_X} \int_{band} \tau_\nu d\nu \quad (4.1)$$

where $N(X)$ is the column density (which can be converted to number of monolayers), A_X is the band strength of the IR features listed in Table 4.1, and τ_ν is the optical depth of the absorption band. We also take spectra routinely during irradiation of the ice and during the post-irradiation TPD (more in Section 4.3.2), approximately

every ~ 5 K to monitor the desorption of the ice mixture components.

Species	Band (cm^{-1})	A_i (cm^{-1})	Reference (cm mol^{-1})
NH ₃	1070	1.7×10^{-17}	D’Hendecourt & Allamandola (1986)
CH ₄	1304	8.0×10^{-18}	Bouilloud et al. (2015)
C ₂ H ₆	2976	1.1×10^{-17}	Moore & Hudson (1998)
C ₂ H ₄	1436	2.9×10^{-18}	Moore & Hudson (1998)
C ₂ H ₂	742	2.4×10^{-17}	Hudson et al. (2014a)

Table 4.1: Ice infrared data values for the NH₃:C_xH_y experiments.

4.3.2 Temperature Programmed Desorption

Temperature-Programmed Desorption (TPD) provides a complementary product identification tool to infrared spectroscopy. The basic principle behind TPD is that different molecules have different desorption temperatures. Therefore, species sublime from the ice at different times when heated up and their m/z fragments are detected by the QMS. During TPD experiments, we employ a ramp rate of 2 K min⁻¹ and we set a goal temperature in the range 150-180 K. The initial ice components are identified through their characteristic mass fragments, for example (this is not a comprehensive list): $m/z = 17$, NH₃; $m/z = 16$, CH₄; $m/z = 30$, C₂H₆; $m/z = 28$, C₂H₄; $m/z = 26$, C₂H₂; $m/z = 28$, N₂. In addition, we monitor a range of m/z that could originate from plausible ice chemistry products. We put a particular emphasis on $m/z = 27$ as it can correspond to HCN and $m/z = 41$ as it could be indicative of CH₃CN formation. The presence of either of these at

the 'right' desorption temperatures of HCN or CH₃CN would suggest that nitrile formation is successfully taking place.

4.4 Experimental Design: NH₃ & Hydrocarbons

For our NH₃:C_xH_y experiments, we prepare a mixture of gases in the ratio 1:1. We opt for this ratio because it is the simplest ratio that can be explored, and therefore it provides a good starting point to study these reactions. The gases come directly from steel canisters and need no further preparation: ¹⁴NH₃ (Sigma Aldrich, ≥ 99.98%), ¹²C₂H₆ (Sigma Aldrich, ≥ 99.99%), ¹²C₂H₄ (Sigma Aldrich, ≥ 99.5%), ¹²C₂H₂ (Matheson Tri Gas, ≥ 99.6%). The total pressure of gases in the line was 2 Torr, and we continue dosing until we reach a thickness of 50 monolayers (ML; more on IR spectral band analysis in §4.3.1). Because of the corrosive nature of NH₃, we use the corrosive gas line at 90°. During the dosing process we take one IR spectrum (averaged over 64 interferograms) every 60 seconds. The 1:1 NH₃:C_xH_y mixtures are prepared by adding 2.64 Torr of each NH₃ and the hydrocarbon to separate bulbs on the gas-mixing line. Five minutes before dosing, we open the bulbs containing the mixture components and let them flow into the gas line. This is to ensure mixing of the gases. Once the ices are deposited, we take an IR spectrum at 180° and 225°. We then turn the substrate so that it is facing the Deuterium lamp and we begin VUV-irradiation for 6 hours. During this time, we take one spectra (averaged over 64 interferograms) every 15 minutes. We conclude with a TPD (more in §4.3.2) up to 150-180 K. We take a spectra every 5 K (therefore, every 150 seconds).

The three irradiation temperatures of 30 K, 40 K and 50 K were chosen because

CHAPTER 4. EXPERIMENTAL METHODS

we expect radical diffusion in the ice to increase with increasing temperature so we expect more successful recombinations at higher temperatures (although this is ultimately not what we observe). We do not go above 50 K as the hydrocarbons start desorbing at ~ 55 K so we do not want any sublimation taking place during irradiation (Behmard et al. 2019). We investigate NH_3 chemistry since this molecule is one of the most abundant N-reservoirs in protoplanetary disks (abundance is suspected to be as high as 15% of interstellar ices) and so it is a good candidate for the source of the N in nitriles ($-\text{C}\equiv\text{N}$) in both disks and these reactions (Bottinelli et al. 2010). Our target species, CH_3CN , has 2 C atoms so we choose the hydrocarbons C_2H_6 , C_2H_4 and C_2H_2 as are the simplest sources of 2C. Initially, these experiments were carried out with an ice thickness of 400 ML to try to maximise the concentration of radicals in the ice, however, we observed very little chemistry and so we decreased the thickness to 100 ML. A summary of the experiments is given in Table 4.2.

Experiment	Ice	Temperature [K]	Thickness [ML]	Ratio	Irr. Time [min]	Ph. Flux [$10^{12} \text{ cm}^{-2} \text{ s}^{-1}$]	Ph. Fluence [10^{17} cm^{-2}]
1	NH ₃ :C ₂ H ₆	30	100 ± 20	1:0.8	360	81.4 ± 8.1	17.6
2	NH ₃ :C ₂ H ₆	40	73 ± 15	1:1	360	60.4 ± 6.0	13.1
3	NH ₃ :C ₂ H ₆	50	95 ± 19	1:1.1 ^c	360	67.7 ± 6.8	14.6
4	NH ₃ :C ₂ H ₄	30	101 ± 20	1.1:1	360	73.1 ± 7.3	15.8
5	NH ₃ :C ₂ H ₄	40	105 ± 21	1:1	360	68.2 ± 6.8	14.7
6	NH ₃ :C ₂ H ₄	50	117 ± 23	1.1:1	360	82.4 ± 8.2	17.2
7	NH ₃ :C ₂ H ₂	30	71 ± 14	1:1.1	360	45.8 ± 4.6	9.9
8	NH ₃ :C ₂ H ₂	40	139 ± 28	1:1.1	360	73.1 ± 7.3	15.8
9	NH ₃ :C ₂ H ₂	50	97 ± 19	1:1.3	360	74.1 ± 7.4	16.0

Table 4.2: Experimental parameters for VUV-irradiation experiments for NH₃:C_xH_y ice mixtures.

Chapter 5

Experimental Results

In this chapter, we present the results of the irradiation of $\text{NH}_3:\text{C}_x\text{H}_y$ ice mixtures. Our chosen hydrocarbons are C_2H_6 , C_2H_4 , C_2H_2 . We find that the photo-processing of these ices yields a variety of products from CH_3CN (acetonitrile) to CH_4 (mC_2H_6). Here, we will focus on the analysis of nitrogen-containing products (imines, amines and nitriles). The growth curves for hydrocarbons formed during irradiation can be found in Appendix A.1. We begin this chapter by giving a general overview of the analysis and the steps that we will take to process our data (§5.1). Then, we lay out our findings and results in §5.2- 5.4. Finally, we provide a summary of results in §5.5.

5.1 Analysis Overview

We identify products by examining the IR spectrum pre- and post- irradiation and pinpointing any changes (such as newly formed peaks). In order to do so, we first

CHAPTER 5. EXPERIMENTAL RESULTS

apply a global baseline to flatten the spectra and move the baseline to 0. This allows for a more precise calculation of the integrated absorbance of the peaks. We also apply a local linear baseline (first degree polynomial) for the selected regions of the spectrum that present features of interest. The majority of peaks are identified using ice spectra from astronomical literature and databases (for example, the Goddard Ice Database and the Kinetic Ice Database for Astrochemistry) (Moore et al. 2007; Wakelam et al. 2012). Alternatively, we use the IR Spectrum Table Chart by Sigma Aldrich¹ to pin down the source of our observed features. Table 5.1 offers an overview of the main products that we observe during the irradiation of the $\text{NH}_3\text{:C}_x\text{H}_y$ ice mixtures.

Analysing the peaks from the IR spectra alone is not sufficient to confirm the identities of our products. We complete the identification by examining the TPD traces of different m/z values and assigning them to a particular photoproduct by combining known desorption temperatures reported in the literature, and m/z QMS fractionation patterns reported at NIST². Table 5.2 shows the m/z values of the masses that we monitor during our experiments and their associated parent molecule.

As discussed in §4.3.1, the integrated absorbances can be used to calculate the number of monolayers of each species, assuming that we can identify a feature with a specific molecule or molecular group and the band strength of the spectral feature

¹Available at <https://www.sigmaaldrich.com/technical-documents/articles/biology/ir-spectrum-table.html>.

²Available at: <https://webbook.nist.gov/chemistry/>

CHAPTER 5. EXPERIMENTAL RESULTS

Species	Mode	Lit wn [cm ⁻¹]	Ref	Observed wn [cm ⁻¹]	Experiments
C ₂ H ₄	CH ₃ rocking	951	1	958	1-9
C ₄ H ₄ or C ₄ H ₂	overtone/combination	1240	8	1230	7-9
CH ₄	CH ₄ deformation	1298	6	1300	1-9
CH ₃ CH=NH	mixed modes	1358	7	1363	4-6
C ₂ H ₄	CH ₂ scissoring	1435	1	1435	1-9
CH ₃ CH=NH	C=N stretch	1652	7	1650	3-9
C≡C≡C	C≡C asym stretch	2090	3	2090	7-9
CH ₃ CN	C≡N stretch	2252	2	2250	4, 7-9
C ₂ H ₆	CH ₃ stretch	2880	4	2880	4-6, 7-9
C ₂ H ₆	CH ₃ stretch	2968	6	2990	4-6, 7-9
C ₂ H ₄	CH ₂ asym stretch	3095	1	3090	1-3
C ₂ H ₂	CH stretch	3240	5	3235	5-6
C ₂ H ₂	CH stretch	3267	1	3258	3

Table 5.1: List of all products identified in the irradiation of NH₃:C_xH_y ices. References: (1) Bennett et al. (2006) (2) D’Hendecourt & Allamandola (1986) (3) Duley & Hu (2009) (4) Hudson & Moore (2004) (5) Hudson et al. (2014b) (6) Moore & Hudson (2003) (7) Stolkin et al. (1977) (8) Zhou et al. (2010).

CHAPTER 5. EXPERIMENTAL RESULTS

Mass Fragment m/z	Parent Molecule
15, 16, 17	NH ₃
24, 25	C ₂ H ₂
26	C ₂ H ₆ , C ₂ H ₄ , C ₂ H ₂
27	C ₂ H ₆ , C ₂ H ₄
28	CH ₃ CH ₂ NH ₂ , C ₂ H ₆ , C ₂ H ₄
30	CH ₃ CH ₂ NH ₂ , C ₂ H ₆
39	CH ₃ CN, CH ₃ CH=NH
40	CH ₃ CN
41	CH ₃ CN, CH ₃ CH=NH
44	CH ₃ CH ₂ NH ₂
45	CH ₃ CH ₂ NH ₂

Table 5.2: The mass fragments that we use for our analysis and their potential parent molecule. The fractionation patterns of each of these molecules is obtained from the NIST Chemistry WebBook.

in question is known. Using the band strengths shown in Table 4.2, we are able to calculate the amount of NH₃ and C_xH_y destroyed during the irradiation experiments. The results are summarised in Table 5.3.

Once the products have been identified, and the depletion of the reactants has been quantified we can proceed with the plotting growth curves. The first step is to calculate the photochemical yield by using the number of monolayers of reactant that have been destroyed and the number of monolayers of product that have been formed. We calculate this quantity using the equation:

$$\text{Photochemical Yield}[\%] = \frac{\text{Product Formed [ML]}}{\text{Reactant Destroyed [ML]}} \times 100 \quad (5.1)$$

The photochemical yield can then be plotted as a function of time or photon fluence.

CHAPTER 5. EXPERIMENTAL RESULTS

Exp	Ice	Temperature	Initial Thickness	Destroyed NH ₃		Destroyed C _x H _y	
		[K]	[ML]	[ML]	[% initial]	[ML]	[% initial]
1	NH ₃ :C ₂ H ₆	30	100	10	18	7	15
2		40	73	8	21	10	27
3		50	95	7	15	13	26
4	NH ₃ :C ₂ H ₄	30	101	20	35	23	50
5		40	105	12	23	23	50
6		50	117	7	14	14	48
7	NH ₃ :C ₂ H ₂	30	71	17	51	23	64
8		40	139	32	46	40	55
9		50	97	20	39	36	55

Table 5.3: Summary of reactant depletion during the irradiation of our NH₃:C_xH_y ices.

To fit the data in our experiments we use a pseudo-first order rate equation given by:

$$[\text{product}]_t = N_{ss}(1 - e^{\sigma_{form} \cdot \phi}), \quad (5.2)$$

where N_{ss} is the photochemical yield once the system reaches steady state, σ_{form} represents the formation cross section normalised to the steady-state of the product (i.e., represents how quickly the reaction in question is approaching steady-state) in cm², and ϕ is the photon fluence in cm⁻² (Bergner et al. 2019; Martín-Doménech et al. 2020). We use Scipy’s `curvefit` function to minimise χ -squared and find the best-fit curve for our desired parameters. By plotting these growth curves and depletion curves (for the reactants), we are able to calculate the photochemical yield of each product. This is the amount of product that is formed expressed as a percentage of the amount of destroyed reactant. For the hydrocarbon products, we give the yield as a percentage of the destroyed C₂H₆, C₂H₄ or C₂H₂. For imines and

nitriles, we express their photochemical yield as a percentage of the destroyed NH_3 .

5.2 $\text{NH}_3:\text{C}_2\text{H}_6$ Ice Mixtures

Figure 5.1 shows the spectra of the $\text{NH}_3:\text{C}_2\text{H}_6$ 1:1 ice mixtures before and after 6 hours of VUV irradiation at 30 K, 40 K, and 50 K.

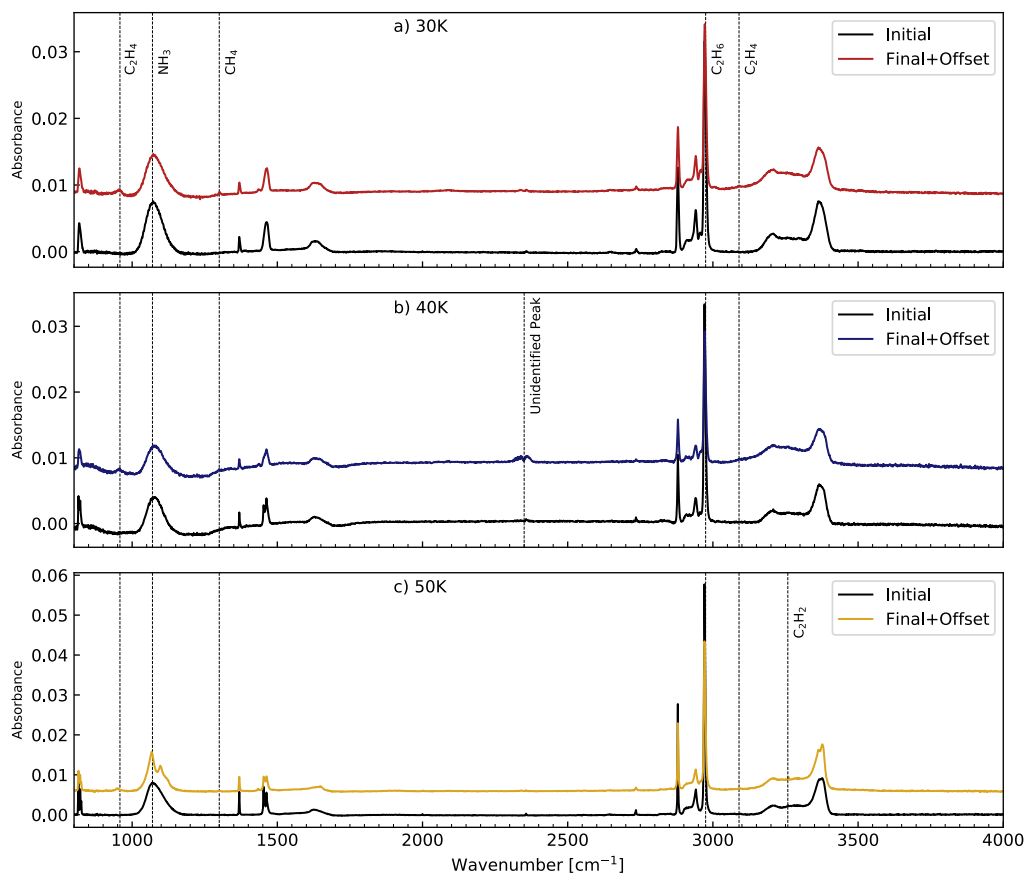


Figure 5.1 The pre- and post-irradiation spectra for $\text{NH}_3:\text{C}_2\text{H}_6$ at different temperatures: 30 K (a), 40 K (b), 50 K (c).

To check for more subtle change, we subtract the spectrum pre-irradiation from the post-irradiation spectrum. The resulting subtracted spectra are shown in Figure 5.2.

CHAPTER 5. EXPERIMENTAL RESULTS

By doing this, we are able to identify a new feature forming at 1650 cm^{-1} during the irradiation at 50 K. Table 5.1 lists all the new features observed in each experiment. We also calculate the number of monolayers of destroyed NH_3 and destroyed C_2H_6 . These are reported in Table 5.3. The percentage of destroyed NH_3 with respect to the initial amount varies between 15-21% without following any clear trend. The depletion of C_2H_6 is in the range 15-27%.

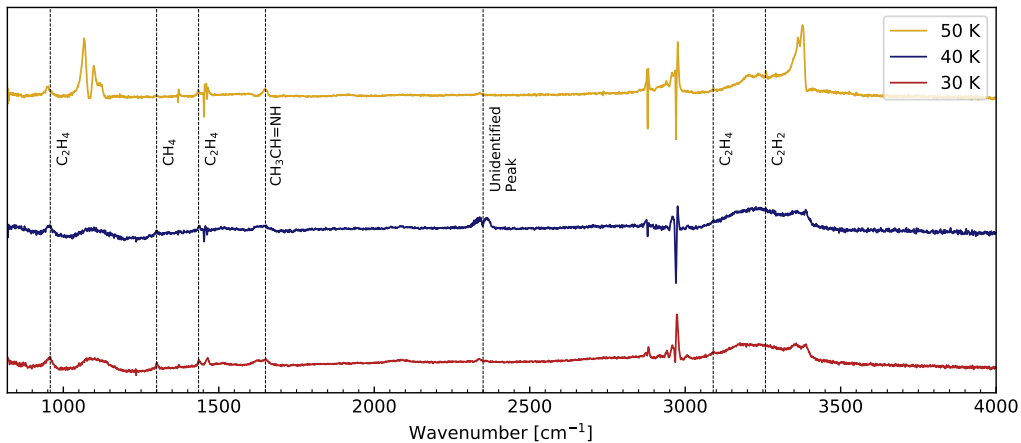


Figure 5.2 The initial spectrum at each temperature is subtracted from the post-irradiation spectrum. This highlights any changes that may have occurred and are too subtle to observe in the original spectrum alone.

From Figure 5.1, we observe that the new peaks form during irradiation at all temperatures. Most of these features correspond to vibrational modes associated with hydrocarbons, and there appears to be little interaction between NH_3 and hydrocarbon radicals. From comparing the pre- and post-irradiation spectra we identify the following products at all three irradiation temperatures: C_2H_4 (958 cm^{-1}) and CH_4 (1300 cm^{-1}) (Bennett et al. 2006; Moore & Hudson 2003). In addition to these hydrocarbon species, the 50 K irradiation also yields C_2H_2

CHAPTER 5. EXPERIMENTAL RESULTS

(3258 cm^{-1}) (Bennett et al. 2006). We also note a slight change in morphology for the peak at $\sim 1620\text{ cm}^{-1}$. From the 50 K subtracted spectrum in Figure 5.2 and from the zoom-in in Figure 5.3a, we confirm that there is indeed a feature growing at 1650 cm^{-1} , which we attribute to $\text{CH}_3\text{CH}=\text{NH}$ (ethanimine). To check for other N-containing products, we zoom into the regions of the spectra where we would expect to see nitriles amines. We observe no new features, thus we conclude that the irradiation of $\text{NH}_3:\text{C}_2\text{H}_6$ does not yield either of these species.

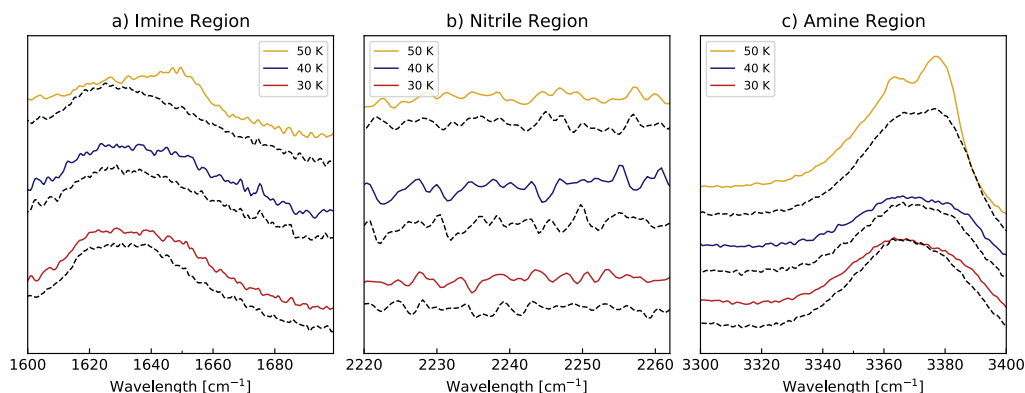


Figure 5.3 Close-up of the nitrile region (Panel a) and amine region (Panel b). The dotted lines show the pre-irradiation spectra at each irradiation temperature. The spectra post-irradiation are shown as solid lines. We observe no significant changes in either of these regions. These are based on laboratory ice spectra from Danger et al. (2011) for the imine, (D’Hendecourt & Allamandola 1986) for the nitrile region and from our own experiments (§.2) for the amine.

As previously mentioned, the IR feature at 1650 cm^{-1} seen in the 50 K irradiation is suspected to belong to an imine. This assignment is made comparing our findings to the work done by Danger et al. (2011), as they observed the same change peak arising during the irradiation of pure $\text{CH}_3\text{CH}_2\text{NH}_2$ ices and attributed it to the

CHAPTER 5. EXPERIMENTAL RESULTS

formation of an imine intermediate. The most likely candidate for our imine, given the identity of our reactants, is $\text{CH}_3\text{CH}=\text{NH}$ (ethanimine) since we would expect the C_2H_6 to contribute to the 2-C chain of $\text{CH}_3\text{CH}=\text{NH}$ and NH_3 to provide the N. There are no known TPD traces for $\text{CH}_3\text{CH}=\text{NH}$, however, we notice that the peak at 1650 cm^{-1} begins to disappear at $\sim 90\text{ K}$ and is completely gone by 120 K . We notice that the QMS trace, obtained during the TPD, for mass fragments with m/z value of 39 and 41 (shown in Figure 5.4) follow the same pattern of desorption that the $\text{CH}_3\text{CH}=\text{NH}$ peak does. Therefore, we conclude that these TPD traces are likely arising from the desorption of CH_3CHNH . To quantify the imine production we use the calculated IR spectra of Melli et al. (2018). The band strength of the 1650 cm^{-1} feature is unknown; however, we can calculate it by comparing the intensity of our peak of interest to the intensity of other peaks in the CH_3CHNH with known A_i (since the band strength is a measure of how intense the IR features are). We use the CH_3 in-plane scissoring mode, which has band strength $2.9 \times 10^{-18}\text{ cm}^{-1}$, and we calculate that the peak at 1650 cm^{-1} is approximately $4\times$ more pronounced. Therefore, we calculate a band strength of $1.2 \times 10^{-17}\text{ cm}^{-1}$ for the feature at 1650 cm^{-1} . Using this value we can express the amount of $\text{CH}_3\text{CH}=\text{NH}$ formed as a percentage of both the initial and destroyed amount of NH_3 . The resulting growth curves are shown in Figure 5.5.

Overall, the formation of hydrocarbons is favoured over the production of nitrogen-containing products and the reactions leading to hydrocarbon products are more efficient at lower temperatures. This is because photochemical yields compared to the depleted C_2H_6 range between 2.1% at 50 K and 28% at 30 K for CH_4 , and between 29%-12% for C_2H_4 . At 50 K , approximately 8% of the depleted C_2H_6

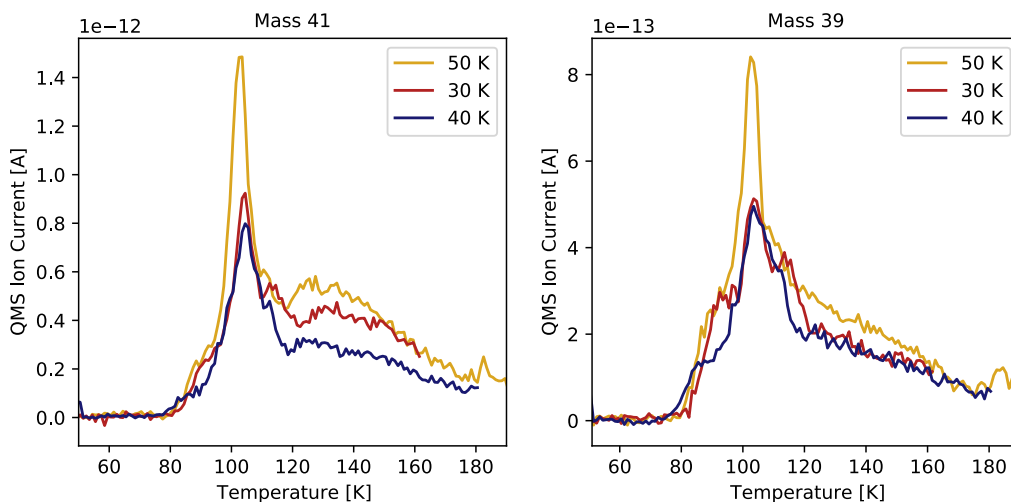


Figure 5.4 The TPD traces for m/z values 39 and 41. These cannot belong to any of our hydrocarbon products as we see from the spectra taken during TPD that they completely desorb by 85 K. The only remaining candidates are amines, imines and nitriles, and based on the infrared spectra, we conclude that this is due to imine formation in the ice.

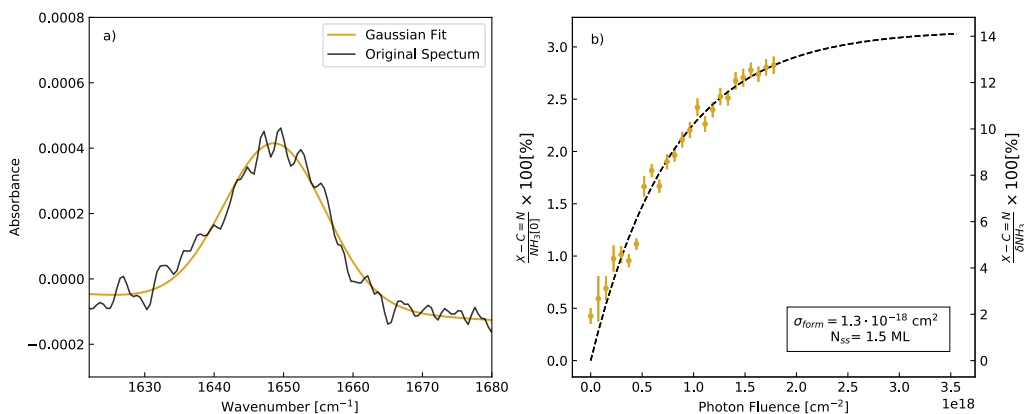


Figure 5.5 Panel a) Gaussian fitting of the imine spectral feature at 1650 cm^{-1} for the final spectra of the $\text{NH}_3:\text{C}_2\text{H}_6$ 50 K experiment. Panel b) left axis - the amount of imine formed as a percentage of the destroyed NH_3 (10 ML); right axis - the amount of imine formed as a percentage of the initial amount of NH_3 (45 ML).

goes into $\text{CH}_3\text{CH}=\text{NH}$ formation whereas over 15% is involved in the production of hydrocarbons, which strengthens the idea that the production of hydrocarbon products is more efficient than the formation of nitrogen-based products. We also note the formation of a large peak at $\sim 2350\text{ cm}^{-1}$ during the irradiation at 40 K; however, this remains unidentified as it remains largely intact past the maximum TPD temperature, which suggests that a mixture of complex molecules are forming in these experiments. We can estimate their importance by comparing the total amount of depleted ethane or ammonia and determine how much is unaccounted for by the identified products. In total it appears as if 80% and 100% (since we see no other N-based product) of the depleted C_2H_6 and NH_3 respectively, was used for the formation of our observed products. This suggests that these complex molecules that we see forming are one of the main products of this irradiation and so they should be further identified.

5.3 $\text{NH}_3:\text{C}_2\text{H}_4$ Ice Mixtures

Figure 5.6 shows the spectra of the $\text{NH}_3:\text{C}_2\text{H}_4$ ice mixtures before and after 6 hours of VUV irradiation at 30 K, 40 K, and 50 K. Similarly to what we did for the irradiation of $\text{NH}_3:\text{C}_2\text{H}_6$ ices, we subtract the initial spectra from all the subsequent irradiation spectra to detect more subtle changes. This results in Figure 5.7.

We begin our analysis by quantifying NH_3 and C_2H_4 depletion at the three irradiation temperatures. The results are summarised in Table 5.3. Overall, we see that the amount of C_2H_4 destroyed during these irradiation experiments is approximately 50% of the initial C_2H_4 amount for all three temperatures. On the other hand, the

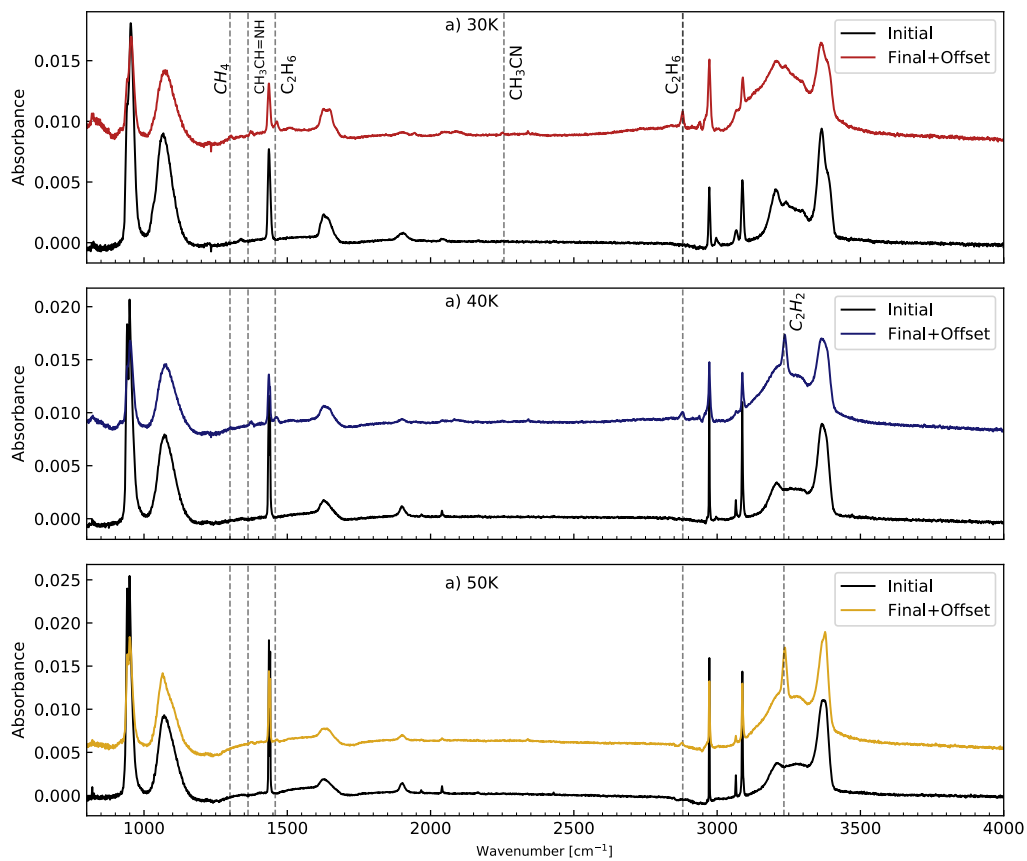


Figure 5.6 The pre- and post-irradiation spectra for $\text{NH}_3:\text{C}_2\text{H}_4$ at different temperatures: 30 K (a), 40 K (b), 50 K (c).

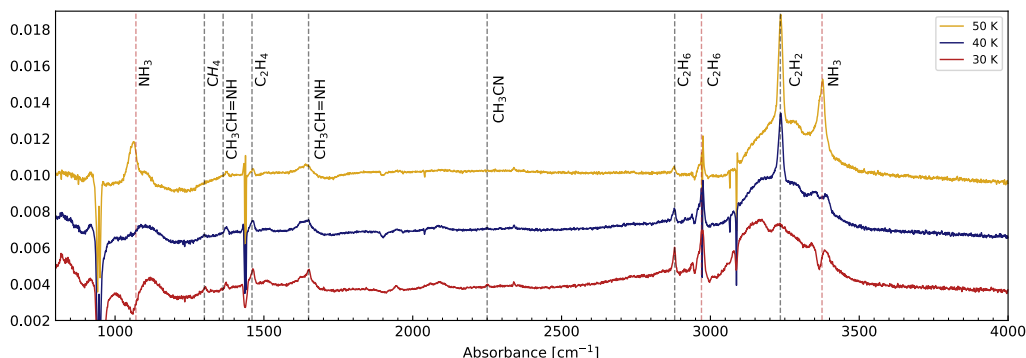


Figure 5.7 The initial spectrum at each irradiation temperature is subtracted from the final spectrum after irradiation to highlight subtle changes. The red spectrum is for the reaction at 30 K, blue is at 40 K and golden is at 50 K. The black dashed lines indicate newly formed peaks which are better characterised in Table 5.1. The red dashed lines highlight changes that have occurred in pre-existing peaks.

amount of NH_3 decreases as the temperature increases. The percentage of NH_3 destroyed during each experiment varies between 7-20 ML, which corresponds to a percentage range of 14-35% of the initial amount of NH_3 . We notice that the amount of destroyed NH_3 decreases by roughly $\sim 40\%$ between 30 K and 40 K, and again between 40 K and 50 K.

From the spectra in Figure 5.6, we see that the products CH_4 (1300 cm^{-1}) and C_2H_6 (2880 cm^{-1}) are common to all three irradiation temperatures (Bennett et al. 2006). We also see a peak at 1350 cm^{-1} , which we identify as belonging to an imine product. We confirm the presence of this species by looking at the subtracted spectra shown in 5.7 as we notice a new feature growing at 1650 cm^{-1} which represents the imine $\text{C}=\text{N}$ stretch (Stolkin et al. 1977). We suspect that the species giving rise to this peak is $\text{CH}_3\text{CH}=\text{NH}$. In addition to these common products, the irradiation of

$\text{NH}_3:\text{C}_2\text{H}_4$ ice mixtures at 40 K and 50 K also yields sharp C_2H_2 peaks at 3235 cm^{-1} (Hudson et al. 2014b). We also that the spectrum of the irradiation at 30 K presents a peak at 2250 cm^{-1} that does not form at 40 K nor at 50 K. We confirm these findings by looking at a close-up of this region of the spectrum for all three irradiation temperatures, as shown in the left panel Figure 5.8. The growth of this peak over 6 hours of irradiation at 30 K is also shown in the right panel of Figure 5.8. It is clear that there are no obvious changes in the post-irradiation spectrum at 40 K and 50 K. We identify this peak as belonging to a nitrile and we suspect that the species giving rise to this feature is CH_3CN (acetonitrile). Finally, we notice that the spectrum of the irradiation carried out at 30 K undergoes a change in morphology between $\sim 3000\text{--}3500\text{ cm}^{-1}$. This broad absorption can be associated with the formation of amines ($-\text{RNH}_2$) (Förstel et al. 2017). Given the identity of our nitrile and imine, we hypothesise that the amine being formed is ethylamine.

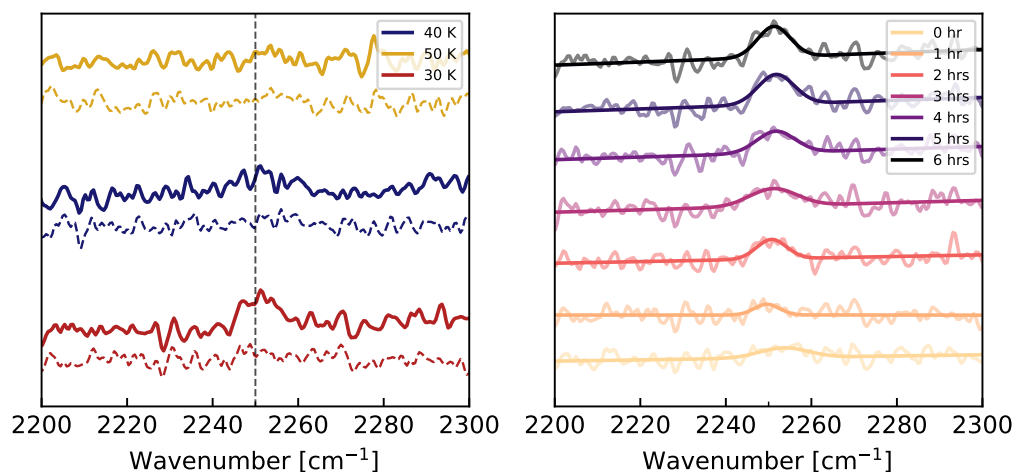


Figure 5.8 Left panel shows the three irradiation temperatures and their initial and final spectrum. The dashed line indicated where we would expect to see nitriles. Right panel shows the hourly growth of the nitrile peak formed at 30 K.

CHAPTER 5. EXPERIMENTAL RESULTS

The nitrile peak forming at 2250cm^{-2} during the 30 K irradiation can be attributed to CH_3CN . The thermal desorption of CH_3CN ice takes place between 120 K and 150 K according to (Collings et al. 2004). This is in good accordance with our findings as we see that in the IR spectra taken during TPD, this peak starts to desorb around 120 K and continues until ~ 150 K. The pattern is matched by the TPD trace for mass fragment with m/z value equal to 41, which is the strongest signal in CH_3CN based on the NIST Chemistry WebBook’s mass fractionation pattern for this molecule. This confirms our assignment of CH_3CN . To quantify CH_3CN production during irradiation at 30 K, we use a band strength of $A_i = 2.2 \times 10^{-18}\text{cm molecule}^{-1}$ (D’Hendecourt & Allamandola 1986). The resulting growth curves, along with an example of a Gaussian fit, are shown in Figure 5.9.

Imine formation can be observed quite clearly as a sharp, albeit small, new peak at 1650 cm^{-1} in the final spectrum of the irradiation at 30 K and as a broader feature in the subtracted spectra at 40 K and 50 K. By performing our Gaussian fitting and monolayer analysis, we obtain the curves shown in Figure 5.10. We suspect that the imine being formed is $\text{CH}_3\text{CH}=\text{NH}$ and the fact that CH_3CN is being produced at 30 K strengthens this idea, assuming that the imine is part of the pathway leading to the formation of nitriles. Further, we find the same TPD peaks with m/z 39 and 41 that we attributed to the imine in the $\text{NH}_3:\text{C}_2\text{H}_6$ experiments (shown in Figure 5.11). We find that in this instance, the imine seems to desorb in two steps and this is also supported by the spectra taken during heating, which show the imine significantly decreasing in size between $\sim 95\text{-}110$ K and then completely disappearing between 120 K-140 K. The mass 41 signal at 30 K is much higher than that of 50 K and 40 K as CH_3CN is also desorbing in that temperature range. Interestingly, we

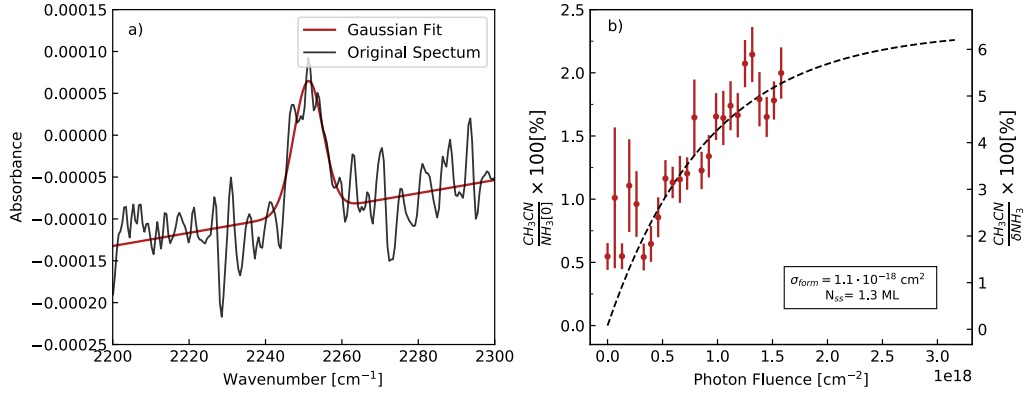


Figure 5.9 The growth curve for CH₃CN during irradiation of NH₃:C₂H₄ ices. Panel a) shows an example of Gaussian fit for the final post-irradiation spectrum of each experiment. Panel b) depicts the amount of CH₃CN formed as a percentage of the initial amount of NH₃ (left axis) and as a percentage of the destroyed NH₃ (left axis; 20 ML). The formation cross section, f_{form} , and the steady state abundance, N_{ss} , both as a percentage of initial C₂H₄ and as an absolute number of monolayers, are also highlighted.

CHAPTER 5. EXPERIMENTAL RESULTS

can see from both the growth curves in Figure 5.10 and Figure 5.11 that there seems to be a correlation between imine and nitrile production. We calculate the ratio between the absolute number of monolayers of formed nitrile and of formed imine at 30 K and we obtain a value of 1:7. The two irradiation temperatures that do not present production of $\text{C}\equiv\text{N}$ compounds also seem to be approaching the imine steady-state during irradiation. On the other hand, the imine at 30 K (where we see CH_3CN production) is still in the linear phase of the exponential growth, which means that it is in the early stages of formation. In general, the photochemical yield at the end of each experiment compared to the depleted NH_3 remains fairly constant across all three temperatures (between 7-10%); however, the photon fluence at which steady-state is reached is greater for 30 K than it is for 40 K and the latter is greater than that at 50 K. This may suggest that the initial step of imine formation depends on radical mobility which explains why steady-state is reached at lower fluences at 40 K and 50 K compared to 30 K, however, the conversion between imine and nitrile is negatively impacted by a higher temperature.

From Figure 5.6 we see that there is a significant change in the morphology of spectra between $3000\text{-}3500\text{ cm}^{-1}$, as we see an increase in the absorbance of the region as well as a peak forming at 3400 cm^{-1} . A similar result was obtained by Förstel et al. (2017) and Kim & Kaiser (2011) upon the irradiation of $\text{NH}_3\text{:CH}_4$ ices and they attributed this change to the formation of an amine group. We adopt the same strategy and we identify the amine formed by looking at common TPD traces for potential candidates ($\text{C}_n\text{H}_{2n+1}\text{NH}_2^+ = 31, 45, 59, 73, 87$) and we pinpoint an unidentified peak desorbing between 110-160 K for mass fragment with m/z value 30. This corresponds to $\text{CH}_3\text{CH}_2\text{NH}_2$'s strongest signal based on the mass

CHAPTER 5. EXPERIMENTAL RESULTS

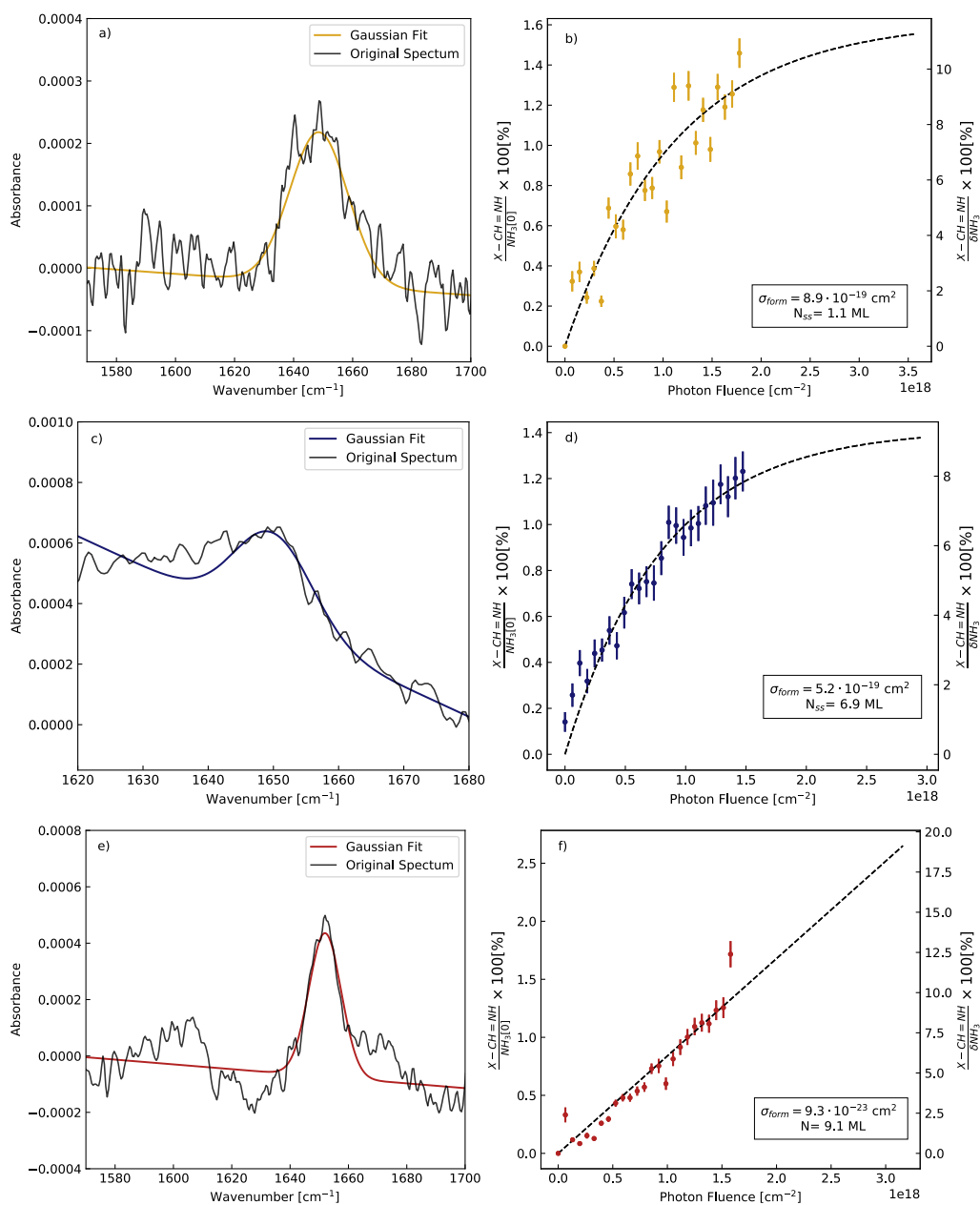


Figure 5.10 Panel a, c, e) show the Gaussian fitting of the imine peak at 50 K, 40 K and 30 K for the final post-irradiation spectrum of each experiment. Panel b, d, f) show the growth curves for $\text{CH}_3\text{CH}=\text{NH}$ during the irradiation of $\text{NH}_3:\text{C}_2\text{H}_4$ ices. The right axis represents the amount of imine formed as a percentage of the initial abundance of NH_3 . The right axis depicts the amount of imine being produced as a percentage of the destroyed NH_3 .

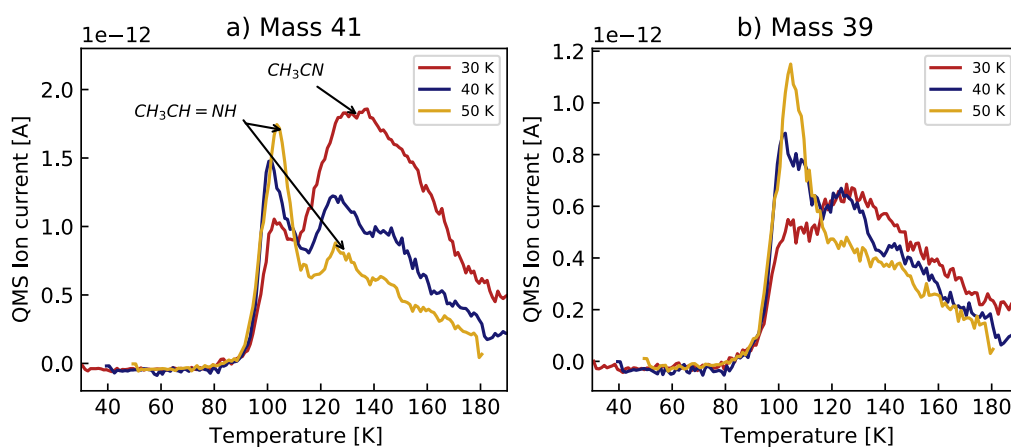


Figure 5.11 TPD traces for mass fragments 41 (a) and 39 (b). The species that are thought to give rise to these peaks are also shown. Given the low ion currents (10^{-12} A), the initial TPD curve was extremely noisy. Therefore, we bin the data in 1 K wide bins and we take the mean signal in each of these bins. The mean signal is then plotted, and results in the TPD traces shown in these panels.

fractionation from the NIST Chemistry WebBook. We confirm the detection of this amine by looking at mass 45 and mass 44, as shown in Figure 5.12. We note that we do not observe peaks in the TPD trace of mass 28, as the strength of the signal from the hydrocarbon drowns out the weak amine signal. Although we are not able to quantify the amount of amine being formed as we lack specific IR features, we are able to see that the intensity of the QMS peaks decreases with increasing temperature, thus implying that less $\text{CH}_3\text{CH}_2\text{NH}_2$ is formed at higher temperatures.

Just like with the $\text{NH}_3:\text{C}_2\text{H}_6$ ices, we see differences in the products that are formed at different temperatures; however, in this instance, the trends are reversed: the higher temperatures (40 K and 50 K) present more hydrocarbon products, whereas, the lower temperatures are more nitrogen-chemistry rich. This difference between the $\text{NH}_3:\text{C}_2\text{H}_6$ and $\text{NH}_3:\text{C}_2\text{H}_4$ suggests that there is a difference in the pathways that lead to the formation of nitriles, and that both of these have a common imine intermediate.

5.4 $\text{NH}_3:\text{C}_2\text{H}_2$ Ice Mixtures

Figure 5.13 shows the spectra of the $\text{NH}_3:\text{C}_2\text{H}_2$ ice mixtures before and after 6 hours of VUV irradiation at 30 K, 40 K, and 50 K. Similarly to what we have previously done, we also present the spectrum resulting from the subtraction of the pre-irradiation spectrum from the post-irradiation spectrum. This is shown in Figure 5.14. Each of the peaks is characterised and assigned to a species in Table 5.1.

Table 5.3 shows the number of destroyed monolayers of NH_3 and C_2H_2 both as

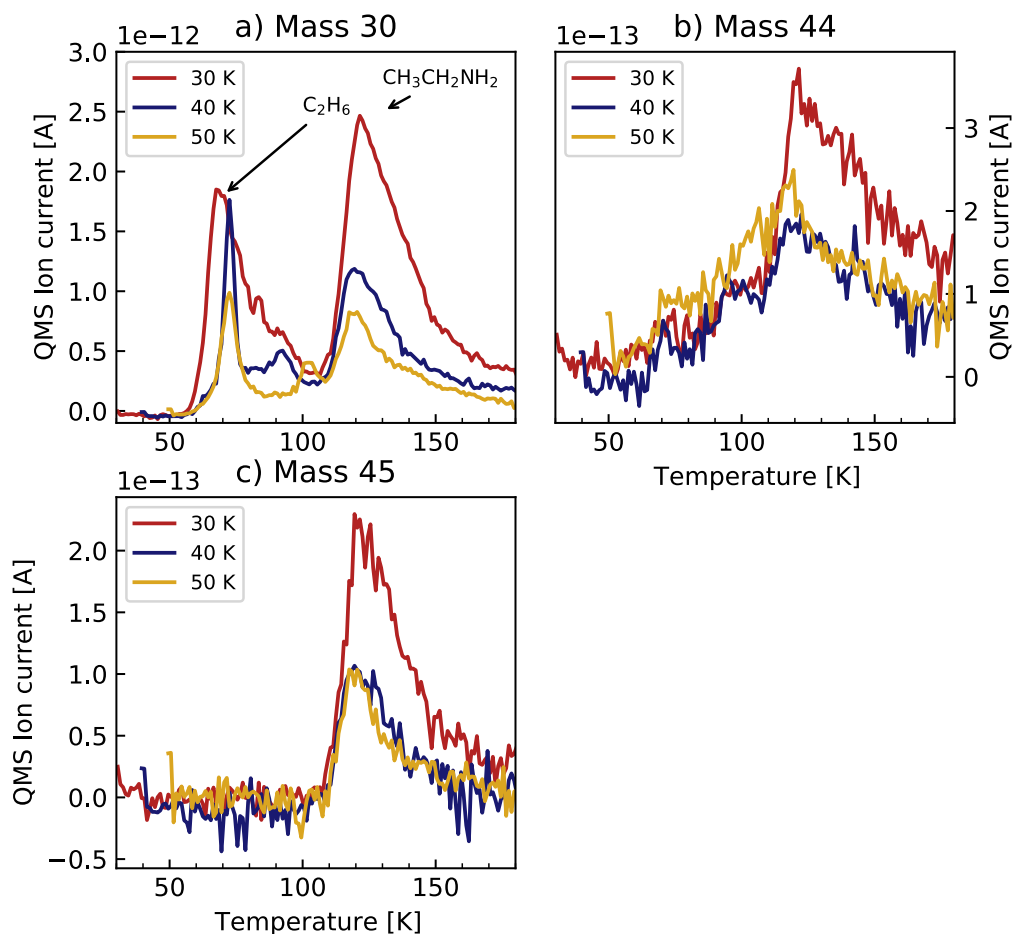


Figure 5.12 The TPD trace for fragments with m/z value 30 ($CH_2NH_2^+$), 44 ($CH_3CHNH_2^+$), 45 ($CH_3CH_2NH_2$). These are the strongest fragments for $CH_3CH=NH$. We find a desorption temperature 110 K and 160 K, and peaking at 124 K.

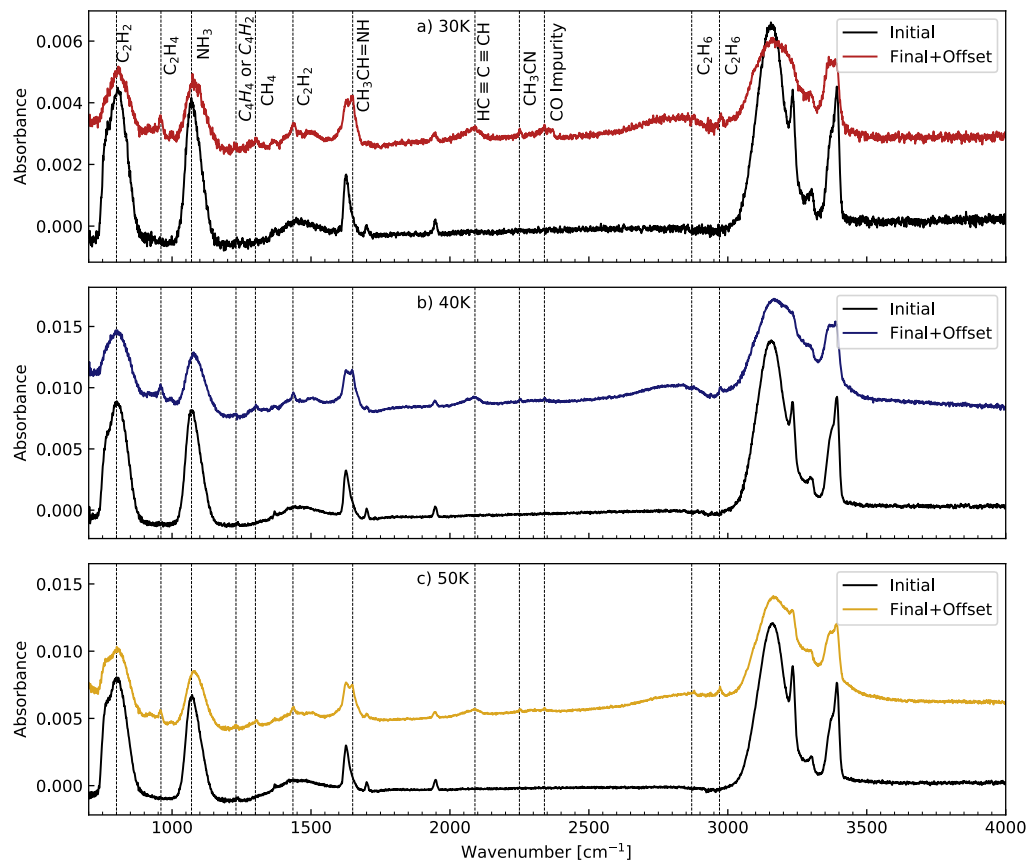


Figure 5.13 The pre- and post-irradiation spectra for NH₃:C₂H₂ at different temperatures: 30 K (a), 40 K (b), 50 K (c).

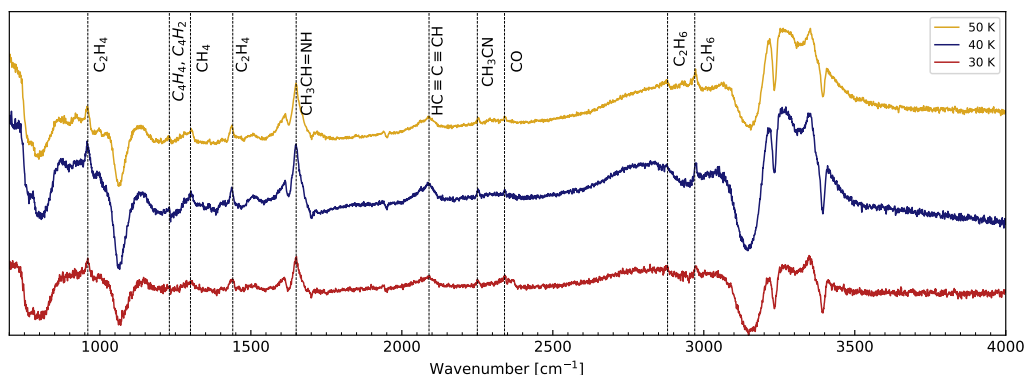


Figure 5.14 The initial spectrum at each irradiation temperature is subtracted from the final spectrum after irradiation to highlight subtle changes. The red spectrum is for the reaction at 30 K, blue is at 40 K and golden is at 50 K. The black dashed lines indicate newly formed peaks which are listed in Table 5.1.

an absolute number and as a percentage of the initial amount of reactant present. The amount of destroyed C_2H_2 remains relatively stable across the three irradiation temperatures, ranging between 55-64% of its initial amount, and no clear trend between the three temperatures. On the other hand, the amount of destroyed NH_3 decreases with increasing temperatures from 51% at 30 K to 39% at 50 K. From the TPD trace of fragments with mass 26 and 27, we find that C_2H_2 desorbs around 100-137 K and NH_3 between 75-105 K in all three experiments.

Most of the products of this irradiation (pre- and post- irradiation spectrum shown in Figure 5.13) can be identified as simple hydrocarbons, such as C_2H_4 and C_2H_6 , but we also see features that can be associated with more complex organics. The broad peak at 2090 cm^{-1} , for instance, suggests the presence of a complex polyyne group and we also notice that once the target temperature of 180 K is reached during warm-up, there are leftover products on the substrate, thus suggesting the

CHAPTER 5. EXPERIMENTAL RESULTS

presence of larger, more complex molecules. We also see the formation of a nitrile (2250 cm^{-1}) at all irradiation temperatures. We suspect that CH_3CN is the nitrile responsible for the formation of this peak. In addition to this, we notice that the feature at 1620 cm^{-1} begins to split during the irradiation. From the subtracted spectra shown in Figure 5.14 we see that this change in morphology is due to a peak growing at 1650 cm^{-1} . We associate this peak to the formation of an imine and more specifically, to the production of $\text{CH}_3\text{CH}=\text{NH}$. A complete summary of the products with their associated vibrational modes is given in Table 5.1.

Unlike the $\text{NH}_3:\text{C}_2\text{H}_4$ experiments where nitriles were only produced at 30 K, we find that $\text{C}\equiv\text{N}$ -bearing species are formed in all three experiments during the irradiation of $\text{NH}_3:\text{C}_2\text{H}_2$ ices. We identify the produced nitrile as CH_3CN . This can be inferred from the TPD trace of the main m/z fragments associated with CH_3CN based on the NIST Chemistry WebBook: mass 39, 40, and 41 (shown in Figure 5.15). By looking at the traces for these fragments, we see that desorption begins around 120 K and continues past 150 K. This is in good accordance with what was found by Collings et al. (2004) when they investigated the thermal desorption of astrophysically relevant molecules, including CH_3CN . Therefore, we are able to confirm our identification of the species as CH_3CN . This is also supported by the IR spectra during TPD since we see that the peak at 2250 cm^{-1} begins to shrink at ~ 120 and continues to do so until it disappears at ~ 170 K. However, it can be seen from the TPD traces shown in Figure 5.15 that the QMS signal is still high at that temperature. We hypothesise that there might be some contribution from a desorbing imine to m/z 39, 40 and 41 at all experimental temperatures. Once we have identified our nitrile, we can quantify its formation and the growth curves

CHAPTER 5. EXPERIMENTAL RESULTS

for CH_3CN at the three different irradiation temperatures are shown in Figure 5.16. We observe no clear trend with regards to the photochemical yield of nitrile as a function of temperature, however, we do find that the ratio of monolayers of produced nitrile to the number of monolayers of imine remains relatively constant for all three irradiation temperatures. In fact, the ratio at 30 K is 1:4, at 40 K it is 1:3 and at 50 K it is 1:3.

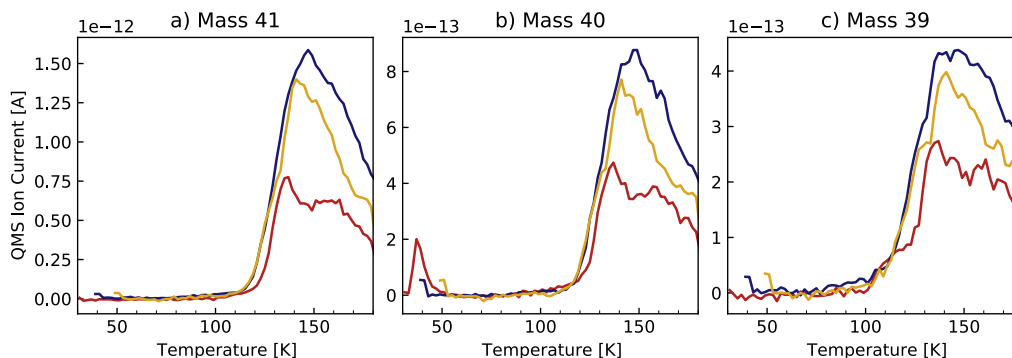


Figure 5.15 The TPD traces for fragments with mass 39, 40, 41. These are the strongest signals for CH_3CN . We find that desorption begins at ~ 120 K and continues past 180 K. These curves were obtained by binning the data in 1 K-wide bins and taking the mean in each bin to remove the high levels of noise.

A priori, we identify the peak at 1650 cm^{-1} as belonging to the species $\text{CH}_3\text{CH}=\text{NH}$. This is because of the identity of our nitrile, CH_3CN , and because of the imine data obtained from the previous experiments. We are unable to use the TPD traces that we usually use, namely m/z 39, 41, as there is contribution from many different species (i.e., CH_3CN , $\text{CH}_3\text{CH}=\text{NH}$) which means that it is impossible to distinguish the peaks as they all blend together into one curve, as shown by Figure 5.15. We notice from the IR spectra taken during the TPD that the peak begin disappearing at ~ 95 K but instead of completely disappearing by 120 K, which is what we would

CHAPTER 5. EXPERIMENTAL RESULTS

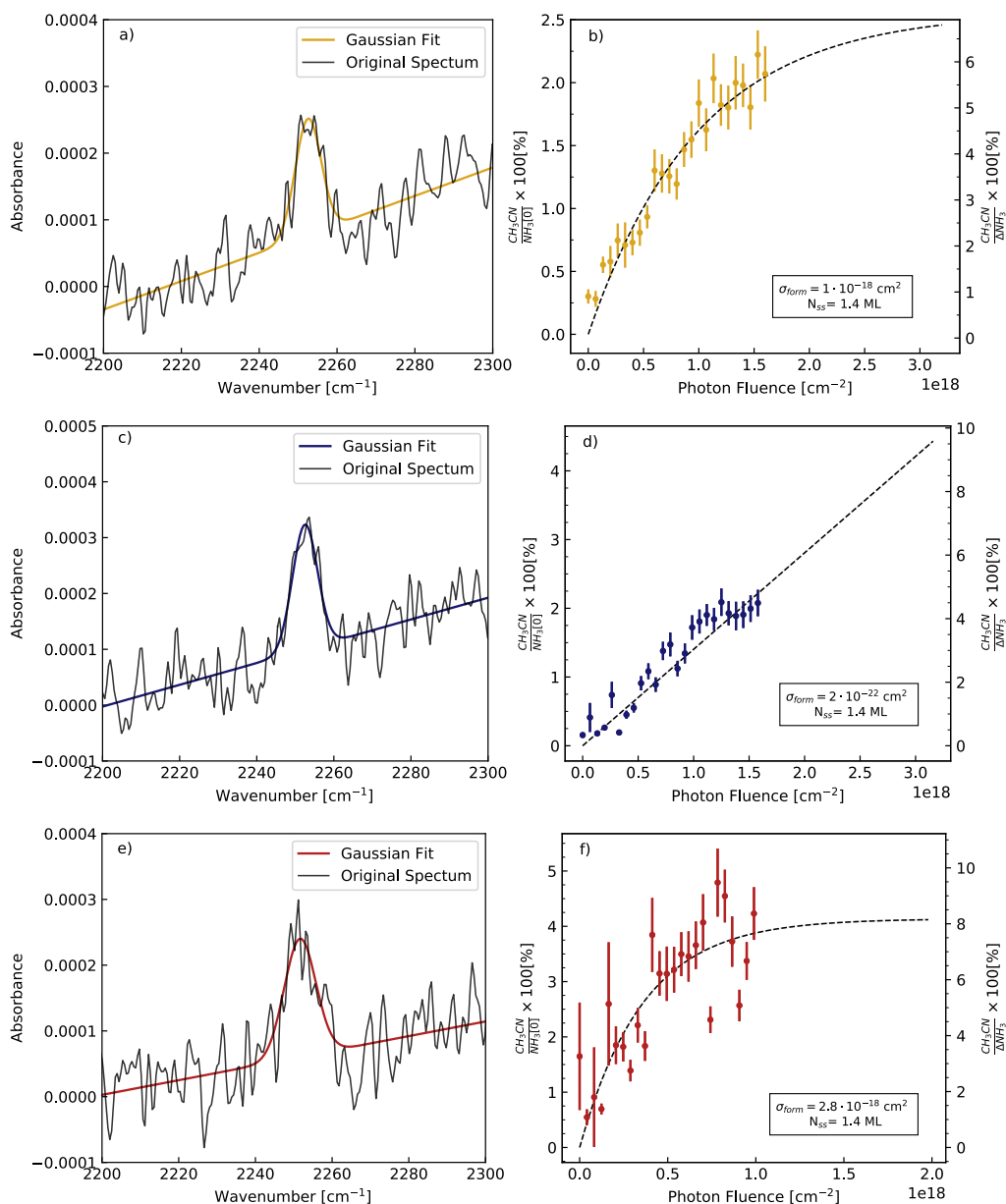


Figure 5.16 Panel a, c, e) show the Gaussian fitting of the CH₃CN peak at 50 K, 40 K and 30 K for the final post-irradiation spectrum of each experiment. Panel b, d, f) show the growth curves for the CH₃CN species during the irradiation of NH₃:C₂H₂ ices. The right axis represents the amount of nitrile formed as a percentage of the initial abundance of NH₃. The left axis depicts the amount of CH₃CN produced as a percentage of the destroyed NH₃.

CHAPTER 5. EXPERIMENTAL RESULTS

expect if $\text{CH}_3\text{CH}=\text{NH}$ only was formed, the peak remains past 180 K as shown by Figure 5.17. This had not previously been observed with any of the other ice mixtures. We attempt to quantify the amount of imine that does not desorb by first looking at the total number of monolayers of this species assuming that the peak is due to the formation of $\text{CH}_3\text{CH}=\text{NH}$ only. The imine growth curves at each temperature are shown in Figure 5.18. From this analysis, we are able to obtain the absolute number of monolayers formed during the irradiation: 3.3 at 30 K, 5.6 at 40 K, and 4.3 at 50 K. We then use the last spectrum taken during warm-up once the temperature had reached 180 K, we calculate the integrated absorbance and we convert into monolayers. At 180 K, 1.9 ML, 2.5 ML and 1.3 ML of imine remain on the substrate for the reaction carried out at 30 K, 40 K and 50 K respectively. This corresponds to 58%, 45% and 30% of the total imine formed. Therefore, it appears as if the amount of complex imine formed decreases with increasing irradiation temperature.

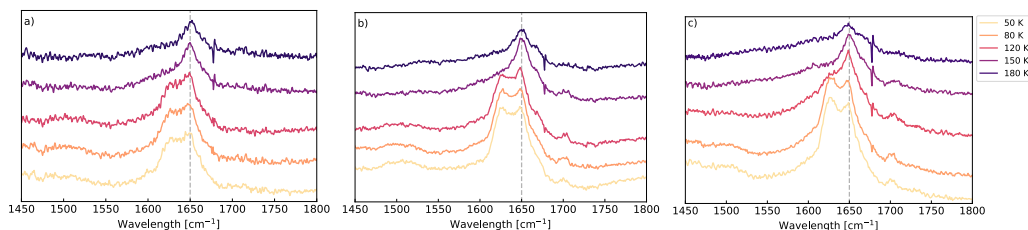


Figure 5.17 Close-up of the imine region during warm-up. Panel a,b,c are for irradiation carried out at 30 K, 40 K, 50 K respectively.

Overall, the formation of all products during the irradiation of $\text{NH}_3:\text{C}_2\text{H}_2$ ices seems to have a negative temperature dependence. This is because both the final and steady-state photochemical yields are highest at 30 K for all products (with the exception of CH_4). The final yields of the imine remain approximately constant

CHAPTER 5. EXPERIMENTAL RESULTS

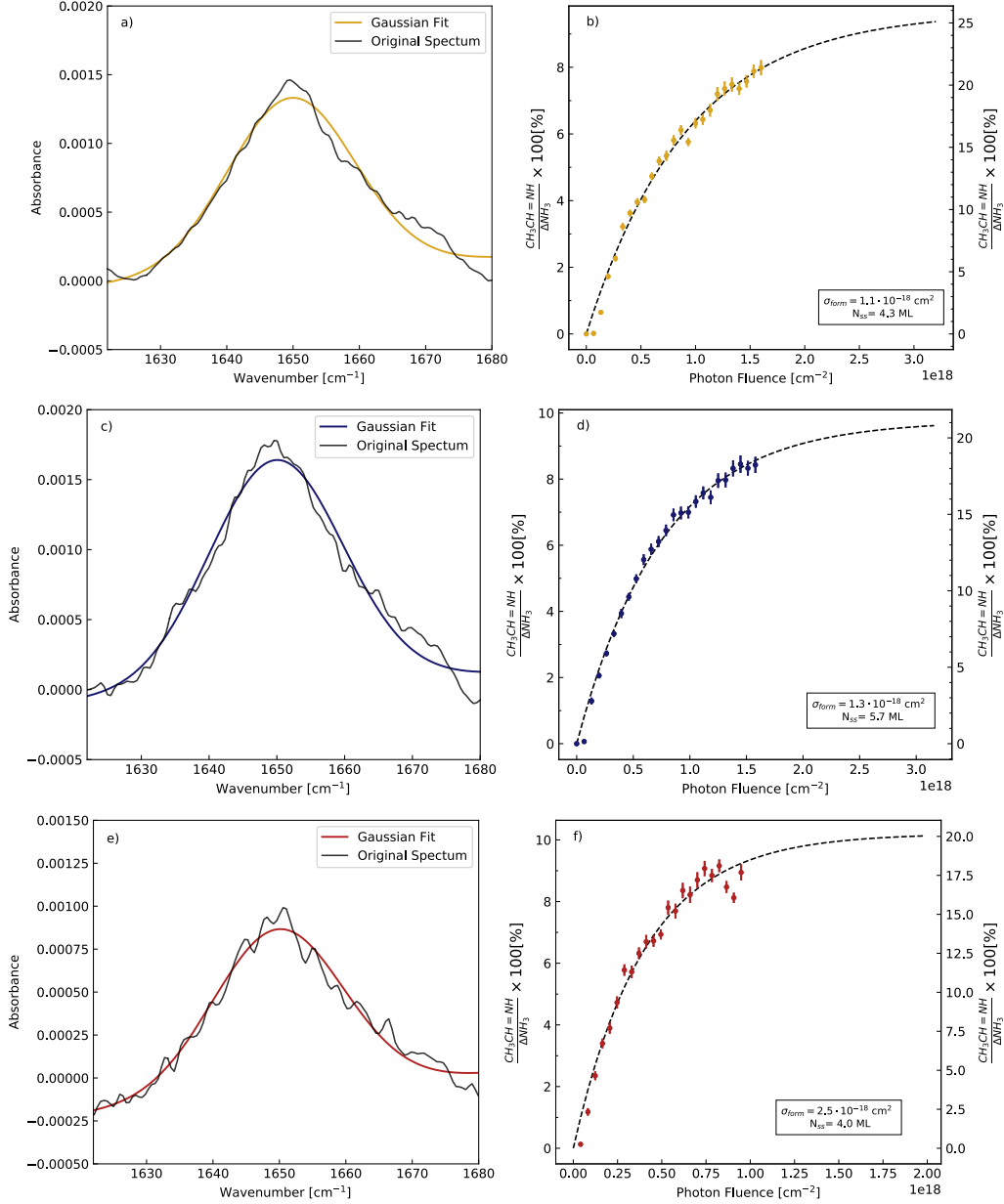


Figure 5.18 Panel a, c, e) show the Gaussian fitting of the imine peak at 50 K, 40 K and 30 K. We use the final subtracted spectrum for this part of the analysis as it better isolates the imine peak. Panel b, d, f) show the growth curves for the imine species during the irradiation of $\text{NH}_3:\text{C}_2\text{H}_2$ ices. The right axis represents the amount of imine formed as a percentage of the initial abundance of NH_3 . The left axis depicts the amount of imine produced as a percentage of the destroyed NH_3 .

across the three irradiation temperatures, ranging between 19% and 25% of the destroyed NH_3 . On the other hand, the CH_3CN yield decreases sharply between 30 K and 40 K, going from 9% to 4%. This seems to imply that the production of imine is less temperature dependent than the formation of nitriles.

5.5 Results Summary

The products, associated TPD masses, desorption temperatures, normalised formation cross-sections and photochemical yields are summarised in Table 5.5. We conclude this chapter by presenting an overview of the photochemical yields for each experiment after a fluence of $1 \times 10^{18} \text{cm}^{-2}$. We pick this fluence because it was the lowest recorded fluence in all of our experiments and we use the interpolate function in Numpy to obtain the photochemical yield of all the experiments with fluence beyond $1 \times 10^{18} \text{cm}^{-2}$. We notice that for the majority of hydrocarbons, the yield decreases as temperature increases except for C_2H_2 and CH_4 during the irradiation of $\text{NH}_3:\text{C}_2\text{H}_4$ ices. For the N-containing species, namely $\text{CH}_3\text{CH}=\text{NH}$ and CH_3CN , we notice that the yield is highest at 30 K, followed by 50 K and it is lowest at 40 K.

CHAPTER 5. EXPERIMENTAL RESULTS

Table 5.4. Experiment Summary

Ice	Products	TPD Trace	Desorption Temp [K]	σ_{form} [10^{-18} cm ²]			Photochemical Yield [%]		
				30 K	40 K	50 K	30 K	40 K	50 K
NH ₃ :C ₂ H ₆	CH ₄	16, 15	60-85	0.89	2.0	1.3	15[28]	5.7[6.7]	2.0[2.1]
	C ₂ H ₄	28, 27, 26	60-85	2.3	5.7	3.5	29[29.5]	13[13]	12[12]
	C ₂ H ₂	26, 27	60-85	-	-	12.1	-	-	1.4[1.5]
	CH ₃ CH=NH	39, 41 (suspected)	95-120	-	-	1.3	-	-	13[14]
NH ₃ :C ₂ H ₄	CH ₄	16, 15	60-85	0.3	0.7	-	6.2[14]	3.4[4.8]	-
	C ₂ H ₆	27, 28, 30	60-85; 95-110	2.0	2.2	1.6	24[26]	16[16]	9.2[9.7]
	C ₂ H ₂	26	70-85; 90-100	-	4.1	1.4	-	28[29]	84[90]
	CH ₃ CH=NH	39, 41 (suspected)	95-120	9.3×10^{-5}	0.52	0.89	12.3	7.2[14]	10[12]
	CH ₃ CN	41	140-180	1.1	-	-	5.8[6.7]	-	-
NH ₃ :C ₂ H ₂	CH ₄	15, 16	60-85	0.51	3.8	2.4	9.0[21]	18[18]	11[12]
	C ₂ H ₆	28, 27, 26	80-100	1.24	0.47	1.2×10^{-4}	2.7[3.3]	2.3[4.6]	2.8
	C ₂ H ₄	29, 27, 26	100-120	6.1	2.6	2.6	4.0[4.3]	4.5[4.5]	3.2[3.2]
	X-CH=NH	39, 41 (suspected)	120-?	2.5	1.3	1.1	19[20]	18[21]	21[26]
	CH ₃ CN	41, 40, 39	120-170	2.8	2×10^{-4}	1.0	7.4[8.1]	4.5	5.5[6.9]

Note. — Table summarising the experiments. The photochemical yield refers to the number of monolayers of the product over the number of monolayers of the starting material (either NH₃ for amines, imines and nitriles or the hydrocarbon for alkanes, alkenes and alkynes). We report the yield at the end of the experiment and in the square brackets we present the steady-state yield. If no steady-state yield is indicated, the growth curve resulted in a linear fit and therefore there was no steady-state.

CHAPTER 5. EXPERIMENTAL RESULTS

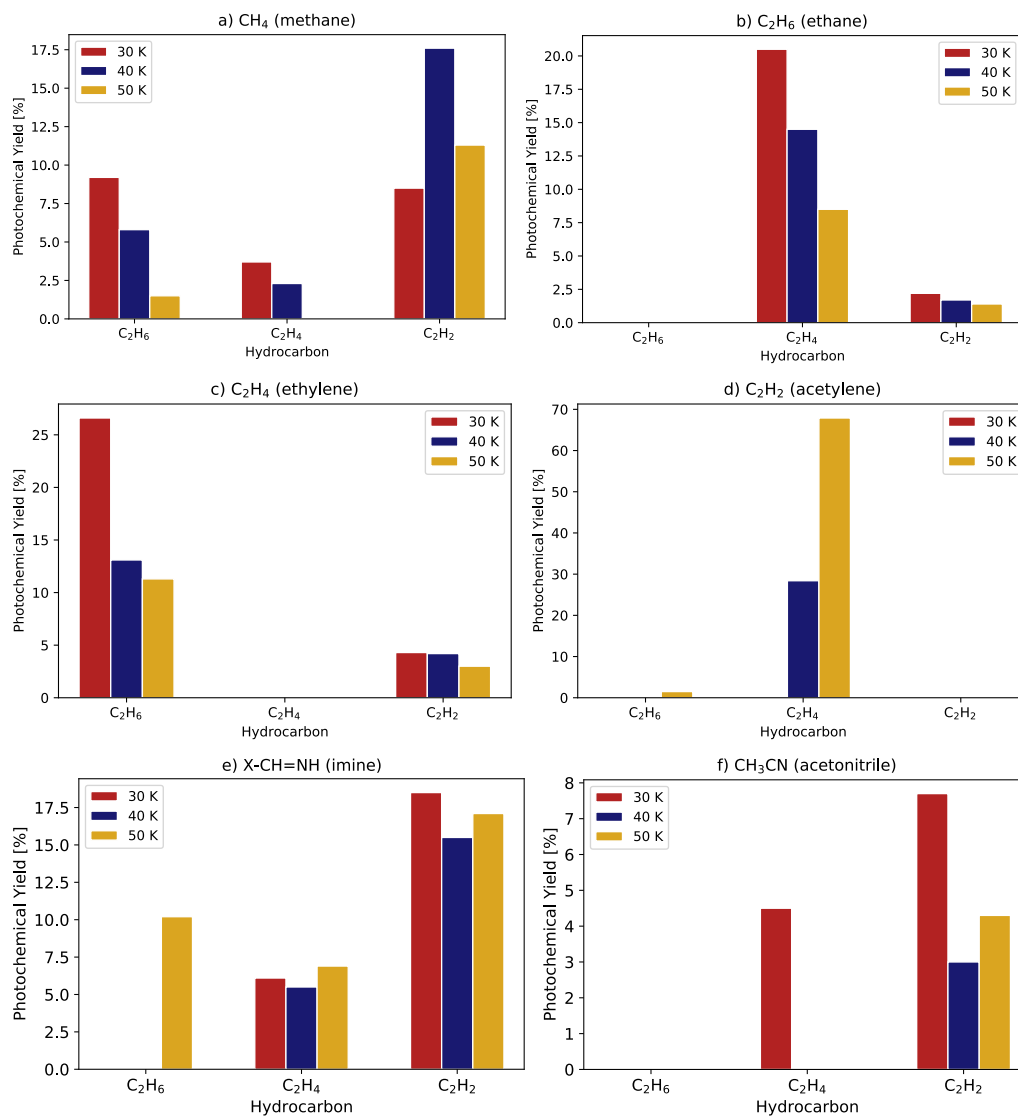


Figure 5.19 Histogram comparing the photochemical yields of each product at a fluence of $1 \times 10^{18} \text{ cm}^{-2}$. This was the lowest fluence recorded ($NH_3:C_2H_2$ experiment).

Chapter 6

Discussion II: Formation of Nitriles during VUV Photoprocessing

In this chapter, we discuss the results from our experiments and their implications for the formation of nitriles in protoplanetary disks. We identify potential pathways responsible for the formation of the observed products and attempt to provide an explanation for the differences in the chemistry between the three $\text{NH}_3:\text{C}_x\text{H}_y$ ice mixtures. We also take a closer look at the temperature dependence of these reactions. Finally, we discuss how NH_3 , C_xH_y and CH_3CN abundances in clouds compare to our findings.

6.1 Comparing Hydrocarbons

Figure 6.1 summarises the proposed reaction pathways for the irradiation of ammonia with the hydrocarbons C_2H_6 , C_2H_4 , and C_2H_2 .

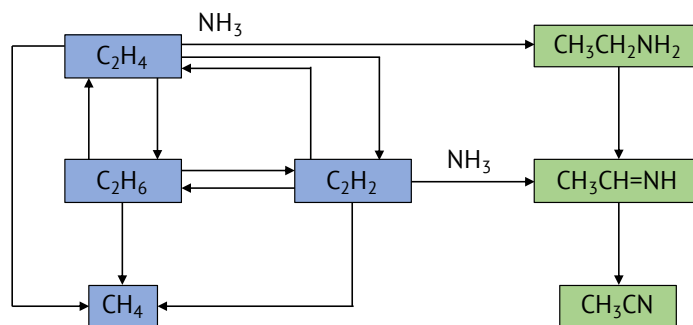
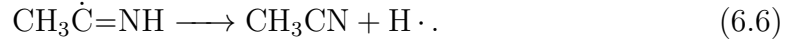
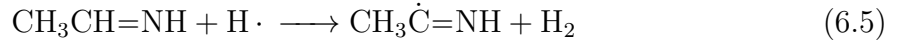
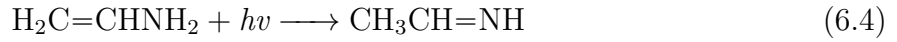
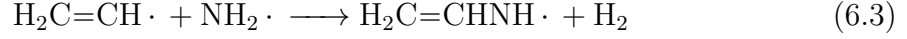
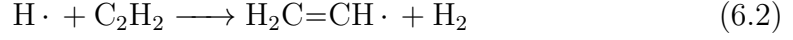
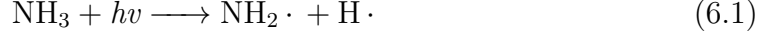


Figure 6.1 Proposed reaction network for the irradiation of ammonia with C_2H_6 , C_2H_4 and C_2H_2 .

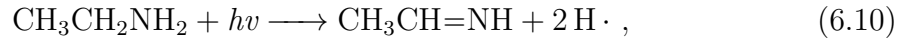
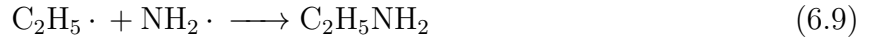
Overall, we find that among the 2-carbon hydrocarbons, production of CH_3CN increases with decreasing saturation. We find that C_2H_6 only yields a small amount of $\text{CH}_3\text{CH}=\text{NH}$ product at 50 K, and we only observe nitriles at 30 K in the C_2H_4 experiments. On the other hand, C_2H_2 is the only one of our hydrocarbons to yield nitriles at all irradiation temperatures. Regardless of the starting hydrocarbon, we hypothesise that a $\text{CH}_3\text{CH}=\text{NH}$ intermediate needs to be formed first, and then hydrogen abstraction of this species leads to the formation of CH_3CN . A possible explanation for the different experimental outcomes across the three $\text{NH}_3:\text{C}_x\text{H}_y$ ice mixtures is that C_2H_2 reacts with NH_3 radicals and directly forms $\text{CH}_3\text{CH}=\text{NH}$, whereas C_2H_4 and C_2H_6 have to be converted into an additional intermediate before being able to react to form $\text{CH}_3\text{CH}=\text{NH}$. From our experimental data, we hypothesize that the identity of this intermediate is C_2H_2 for C_2H_6 and $\text{CH}_3\text{CH}_2\text{NH}_2$ for C_2H_4 . The production of $\text{CH}_3\text{CH}_2\text{NH}_2$ is unique to the C_2H_4 mixtures, as it is not observed in neither the C_2H_2 , nor the C_2H_6 experiments. This results in two different pathways that become active depending on the kind of hydrocarbon that is being irradiated. Ferris & Ishikawa (1987) proposed the following mechanism for the

CHAPTER 6. NITRILE FORMATION

main reaction between NH_3 and C_2H_2 undergoing photoprocessing:



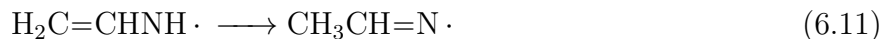
On the other hand, the formation of nitriles in $\text{NH}_3:\text{C}_2\text{H}_2$ mixtures is proposed to take place as follows:



once the $\text{CH}_3\text{CH}=\text{NH}$ is formed, then the reaction proceeds as shown in Equation 6.5 and 6.6 (Keane 2017). These pathways are supported by our findings from the irradiation of $\text{NH}_3:\text{C}_2\text{H}_2$ and $\text{NH}_3:\text{C}_2\text{H}_4$. First of all, both reaction mechanisms predict the presence of the imine $\text{CH}_3\text{CH}=\text{NH}$, which we observe in all reactions involving C_2H_2 and C_2H_4 ices. In addition to this, we have mentioned that the imine peak in the C_2H_2 experiments desorbs in two steps, first between $\sim 90\text{-}120\text{ K}$, and then after 180 K . Although we were not able to pinpoint the species responsible for

CHAPTER 6. NITRILE FORMATION

this high desorption temperature, the pathway laid out in Equation 6.1- 6.6 suggests that more complex imines could form as follows:



(Ferris & Ishikawa 1987). This would explain the presence of large species with desorption temperatures greater than 180 K. In addition to this, these pathways predict that CH_3CN formation in C_2H_4 -containing ices is due to the photoprocessing of $\text{CH}_3\text{CH}_2\text{NH}_2$ into $\text{CH}_3\text{CH}=\text{NH}$, whereas CH_3CN in C_2H_2 ices is formed as a result of the direct reaction between acetylene and ammonia radicals via a $\text{C}=\text{N}$ -containing species. Hence, nitrile production in $\text{NH}_3:\text{C}_2\text{H}_4$ ice mixtures is slowed down by the extra steps of $\text{CH}_3\text{CH}_2\text{NH}_2$ production and subsequent conversion into $\text{CH}_3\text{CH}=\text{NH}$. The presence of $\text{CH}_3\text{CH}_2\text{NH}_2$ in the C_2H_4 ices proposed pathway is once again consistent with our findings as we observe $\text{CH}_3\text{CH}_2\text{NH}_2$ in the $\text{NH}_3:\text{C}_2\text{H}_4$ ice mixtures but not in the $\text{NH}_3:\text{C}_2\text{H}_6$ or $\text{NH}_3:\text{C}_2\text{H}_2$ reactions. We also note that $\text{CH}_3\text{CH}_2\text{NH}_2$ production seems to be highest at 30 K and progressively decrease as temperature increases, which is in good accord with the fact that CH_3CN is only produced at 30 K in the C_2H_4 experiment. As part of a different experimental series, we irradiated pure $\text{CH}_3\text{CH}_2\text{NH}_2$ ices which resulted in some CH_3CN production. The results of this experiment are shown in Appendix .2. We show that the ratio of depleted $\text{CH}_3\text{CH}_2\text{NH}_2$ to formed nitrile is 5:1 at both 50 K and 70 K, which suggests that a certain amount of amine needs to be formed for nitrile production to take place. Reasons why the production of $\text{CH}_3\text{CH}_2\text{NH}_2$, and of the subsequent nitrile, show a temperature dependence will be discussed in Section 6.2.

The mechanism of imine and hydrocarbon production during irradiation of C_2H_6 with NH_3 presents two key differences compared to the irradiation of $\text{NH}_3:\text{C}_2\text{H}_4$ and $\text{NH}_3:\text{C}_2\text{H}_2$ ices. Namely, the lack of nitrile production and the fact that the highest photochemical yield of $\text{CH}_3\text{CH}=\text{NH}$ is recorded during the reaction at 50 K. These phenomena can be partly attributed to radical mobility and hydrogen escape, and will be further discussed in Section 6.2.

6.2 Temperature Dependence

The reactions that we have observed during these experiments can be broadly divided into three distinct categories: hydrocarbon formation, imine formation and nitrile production. We find that the general trend for almost all of the products that we see is that the photochemical yield is highest at 30 K and decreases as temperature increases (with a few exception i.e. production of C_2H_2 from C_2H_4 ices and $\text{CH}_3\text{CH}=\text{NH}$ production in C_2H_6 mixtures). Dissociation by VUV-photons does not have a reaction barrier, therefore we would not expect a temperature dependency from dissociation alone. While the formation of radicals does not depend on temperature, we expect the subsequent steps of radical recombination to be affected by this factor. The ability of radicals to move within the ice matrix (radical mobility) and the concentration of hydrogen radicals in the ice are both temperature-dependent processes and they are some of the main constraints on the rate of formation of $\text{CH}_3\text{CH}=\text{NH}$ and CH_3CN , therefore makes these $\text{NH}_3:\text{C}_x\text{H}_y$ irradiations sensitive to temperature.

As the temperature increases, the rate of hydrogen escape also increases. A key

CHAPTER 6. NITRILE FORMATION

component of the pathways described in §6.1 is the formation of $\text{H}\cdot$ and subsequent addition of these radicals to form H_2 . This molecule has a very low desorption temperature (between 15 K and 35 K) and thus it sublimates from the ices during the course of the irradiation, especially for those that are carried out at 40 K and 50 K (Wakelam et al. 2017). The significance of this process for the formation of our products can be seen from Figure 5.19, as we observe that in the majority of cases, the photochemical yield is highest at 30 K and decreases as temperature increases. This response is particularly evident in the formation of saturated hydrocarbons from the more unsaturated ones. For example, the formation of C_2H_6 from C_2H_4 where we see that the photochemical yield for C_2H_6 is halved between 30 K and 50 K or alternatively, a similar trend can be observed in the formation of C_2H_4 from the more unsaturated C_2H_2 .

Hydrogen escape likely does not play an important role in imine formation under our experimental conditions. We reach this conclusion in view of the fact that the photochemical yields for the formation of $\text{C}=\text{N}$ containing species are fairly constant across all temperature points for all hydrocarbons, except for C_2H_6 (since the pathway for imine formation in C_2H_6 ices is only accessible if C_2H_2 is present, and this is only the case at 50 K). This implies that the presence of hydrogen is not the main factor governing the reactions presented in Equation 6.1-6.4 and 6.7-6.10. Rather, increased radical mobility or the concentration of $\text{NH}_2\cdot$ and $\text{H}_2\text{C}=\text{CH}\cdot$ or $\text{C}_2\text{H}_5\cdot$ radicals may be a bigger constraint during these reactions. If the concentration of ammonia radicals is not high enough, hydrocarbon radicals will be more likely to react together than to react with ammonia radicals, which results in less production of nitrogen-containing compounds and a higher yield of hydrocarbons. On the other

hand, the subsequent production of CH_3CN from $\text{CH}_3\text{CH}=\text{NH}$ seems to be highly influenced by hydrogen escape as there is a sharp drop in the photochemical yield of CH_3CN between 30 K and 40 K. This is unsurprising as Equation 6.5-6.6 show that the conversion between the imine intermediate and the nitrile relies on the presence of hydrogen radicals for H abstraction. The increase in the yield of nitrile between 40 K and 50 K may suggest that the inhibiting effects of hydrogen escape are partially offset by other factors such as increased thermal diffusion in higher temperature ices.

6.3 Astrophysical Implications

In this section, we will attempt to estimate $\text{CH}_3\text{CH}=\text{NH}$ and CH_3CN production through $\text{NH}_3:\text{C}_x\text{H}_y$ ice UV chemistry in different astrophysical environments. We have explored the chemistry of $\text{NH}_3:\text{C}_2\text{H}_6$, $\text{NH}_3:\text{C}_2\text{H}_4$ and $\text{NH}_3:\text{C}_2\text{H}_2$ ices while undergoing photoprocessing by VUV photons. Our irradiation time of 360 min resulted in photon fluences up to $2 \times 10^{18} \text{ cm}^{-2}$, so we can estimate when ices are exposed to a comparable fluence in different astrophysical environments. We assume a minimum FUV-photon flux of $10^8 \text{ cm}^{-2}\text{s}^{-1}$ at the edge of a molecular cloud and a flux of $10^4 \text{ cm}^{-2}\text{s}^{-1}$ in its core, where radiation penetration is strongly decreased by the shielding of gas and dust (Shen et al. 2004). In disks, the flux would likely be much higher as there would be contribution from the central star, whereas these estimates only take into consideration the ISRF. With these parameters, obtaining the fluence used in this experiments would take ~ 700 years at the edge of the cloud, and $\sim 7 \times 10^6$ years in the core. These are lower estimates for the formation of nitriles

CHAPTER 6. NITRILE FORMATION

in disks. On average, clouds will have a lifetime of $\sim 1\text{--}10$ Myrs, which means that the reactions that we have investigated are plausible candidates for the formation of nitriles in these environments. We further note that the UV flux in photodissociating regions (PDRs) is often much higher than our assumed flux, which means that the reaction that we have explored would take place on an even smaller timescales in the cloud edges (Hollenbach & Tielens 1997).

While $\text{CH}_3\text{CH}=\text{NH}$ has only been detected in the massive star formation complex Sgr B2, CH_3CN has been observed in a variety of astronomical bodies including comets, hot cores, interstellar diffuse clouds and protoplanetary disks (Snyder & Buhl 1971; Belloche et al. 2009; Codella et al. 2009; Loomis et al. 2013; Öberg et al. 2015). Interestingly, a survey of four molecular clouds carried out by Liszt et al. (2018) showed that the fractional abundance of CH_3CN relative to H_2 was ubiquitous and had a value of 0.85×10^{-10} . The fractional density of NH_3 around low-mass young stellar objects (LYSOs) is 2.6×10^{-6} (Boogert et al. 2015). The fractional abundance of 2-carbon hydrocarbons in LYSOs are unknown, but we expect them to be approximately one order of magnitude lower than NH_3 based on comet abundances. In our experiments, the percentage of formed CH_3CN to the initial amount of NH_3 varies between 2 and 4%. Therefore, these pathways are plausible candidates for the production of CH_3CN . This is because, assuming a 1:1 ratio for these $\text{NH}_3\text{:C}_x\text{H}_y$ reactions, we would expect only 10% of the available ammonia to react given the hydrocarbon abundances. We would expect to lose approximately another order of magnitude of NH_3 as astronomical ices are not pure, and therefore the presence of radicals from other parent molecules means that the efficiency of the reactions between NH_3 and C_xH_y decreases. While these reactions

CHAPTER 6. NITRILE FORMATION

seem possible when considering the ratio of NH_3 and CH_3CN alone, comparing the column density of $\text{CH}_3\text{CH}=\text{NH}$ and CH_3CN in the molecular cloud Sgr B2 suggests otherwise. The combined column density of E- and Z- $\text{CH}_3\text{CH}=\text{NH}$ is $\sim 9.3 \times 10^{13} \text{ cm}^{-2}$ in Sgr2, whereas the column abundance of CH_3CN is $\sim 2 \times 10^{15} \text{ cm}^{-2}$.

We found that CH_3CN was approximately 30-35% of formed $\text{CH}_3\text{CH}=\text{NH}$ in our experiments. If the explored pathways were responsible for the formation of nitriles then we would expect $\text{CH}_3\text{CH}=\text{NH}$ to be more abundant than CH_3CN . This implies that there must be other mechanisms governing the abundance of nitriles.

One factor that should be further explored is the contribution of cosmic ray ionisation to nitrile chemistry. This would generate a cascade of electrons capable of unlocking different chemical pathways, which would potentially lead to a more efficient formation of $\text{C}\equiv\text{N}$ compounds. This process would exploit the second most abundant species in clouds, N_2 , as incidence with cosmic causes the dissociation of this molecule into its constituent N radicals, which can continue to react with other nearby species and lead to the formation of simple nitriles such as CH_3CN (Chin et al. 2016). The role of electron bombardment of N_2 ices warrants further experiments.

Via our experiments, we were able to explore a low-temperature formation pathway to $\text{CH}_3\text{CH}=\text{NH}$ and to the simple nitrile CH_3CN . Previous studies have shown strong evidence that CH_3CN is formed through the VUV irradiation of CH_3CN by sequential hydrogen atom addition (Woon 2002). However, through this experimental series we have demonstrated that the opposite is also true and that $\text{CH}_3\text{CH}=\text{NH}$ is a key intermediate for the formation of CH_3CN . Further, we have shown that the production of imine via VUV irradiation of $\text{NH}_3:\text{C}_x\text{H}_y$ ices produces

CHAPTER 6. NITRILE FORMATION

a higher yield of imine than nitrile for all hydrocarbons (photochemical yield is ~ 2.5 times larger for imines) which suggests that the reactions that we have investigated may be more suited for the formation of imines than $\text{C}\equiv\text{N}$ -containing compounds. However, the chemistry of these reactions needs to be modelled further to ensure that the ratio of produced imine to produced nitrile remains the same over time.

Chapter 7

Summary & Conclusions

Constraining the abundance and distribution of nitriles in protoplanetary disks allows us to understand the chemical evolution of these species and how it affects the molecular composition of nascent planets. In this thesis, we first focus on the detection of a new nitrile species, CH_2CN , and its relationship to the previously detected CH_3CN (acetonitrile). Next, we investigate the VUV-irradiation of $\text{NH}_3:\text{C}_x\text{H}_y$ ices and how it contributes to the abundance of CH_3CN in protoplanetary disks. Combining observations and experimental data helps us answer the overarching question of what makes a newly-forming planet chemically habitable.

7.1 Summary

Based on our observations of CH_2CN in the TW Hya protoplanetary disk we find that:

CHAPTER 7. CONCLUSIONS

1. Six detected lines that belong to the molecule ortho-CH₂CN. This is the first-time this molecule has ever been observed in a planet-forming environment.
2. Using rotational diagram analysis, we find an excitation temperature of 38 ± 5 K and a column density of $3.5 \pm 0.3 \times 10^{12} \text{cm}^{-2}$ which corresponds to $4.7 \pm 0.3 \times 10^{12} \text{cm}^{-2}$ when accounting for a ortho:para ratio of 3:1.
3. At high spatial resolution, this molecule appears in a ring morphology centered at 24 au. Planet formation occurs in the inner radii of the disks, therefore the fact that we observe the strongest CH₂CN emission in the first 25 au of the disk suggests that this molecule could be incorporated in nascent planets. This morphology is approximately reproduced by our model, and suggests a radial goldilocks zone for CH₃CN formation.
4. Comparison with CH₃CN total column density shows that CH₂CN is 5 times more abundant. This result is consistent with chemical models for TW Hya, where CH₂CN \gg CH₃CN at all disk radii. In light of this discovery complex nitriles may be much more abundant in disks compared to previous estimate based on CH₃CN abundances alone.

From our laboratory experiments, we observe that:

1. For NH₃:hydrocarbon ices, nitrile formation is very sensitive to the saturation of the hydrocarbon. Experiments conducted with ethane did not yield any nitrile formation, whereas CH₃CN is formed during the irradiation of NH₃:C₂H₄ at 30 K and at all reaction temperatures when NH₃:C₂H₂ ices were irradiated.

CHAPTER 7. CONCLUSIONS

2. The production of CH_3CN occurs via an $\text{CH}_3\text{CH}=\text{NH}$ (ethanimine) intermediate. We find that the photochemical yield of this intermediary is consistently 2-10 times higher than that of CH_3CN . This explored chemistry then seems more suited to the production of $\text{CH}_3\text{CH}=\text{NH}$ than CH_3CN .
3. In the reactions of C_2H_2 ices, the $\text{CH}_3\text{CH}=\text{NH}$ intermediate is formed through a combination of photodissociation, radical reactions, and H abstraction. In $\text{NH}_3:\text{C}_2\text{H}_6$ ices, C_2H_6 is first converted to C_2H_2 then it can proceed to form $\text{CH}_3\text{CH}=\text{NH}$. In the C_2H_4 experiments, $\text{CH}_3\text{CH}=\text{NH}$ is formed through the photoprocessing of $\text{CH}_3\text{CH}_2\text{NH}_2$.
4. CH_3CN formation shows higher temperature dependence than the production of $\text{CH}_3\text{CH}=\text{NH}$. This is because the photochemical yield of $\text{CH}_3\text{CH}=\text{NH}$ remains approximately constant across all three reaction temperatures for C_2H_2 and C_2H_4 ices. On the other hand, we observe sharp drops in the yield of CH_3CN when moving from lower to higher reaction temperatures.

7.2 Conclusions & Future Work

The ice chemistry of nitriles in astronomical environments remains largely unexplored. New detections of nitriles and related species, as well as new laboratory experiments are key to constrain the chemical processes and pathways that lead to the formation of nitriles. Our observational data for CH_2CN , combined with that taken by Loomis et al. (2018) for the detection of CH_3CN , suggest that these two species are chemically related in the TW Hya disk. However, by comparing

CHAPTER 7. CONCLUSIONS

observational data to Le Gal et al. (2019b)’s model we observe that while the abundance of CH_2CN is well constrained by standard disk models, that of CH_3CN is underestimated. Observations of CH_2CN and CH_3CN in other disks are needed to see whether the presence of CH_2CN is common and whether the $\text{CH}_2\text{CN}:\text{CH}_3\text{CN}$ observed in TW Hya is replicated in other protoplanetary disks. If this is not the case, it would be interesting to investigate factors (e.g., star type) that affect the presence of CH_2CN and the $\text{CH}_2\text{CN}:\text{CH}_3\text{CN}$ ratio.

We attempt to identify reactions that could contribute to the abundance of CH_3CN by looking at the photoprocessing of $\text{NH}_3:\text{C}_2\text{H}_6$, $\text{NH}_3:\text{C}_2\text{H}_4$, $\text{NH}_3:\text{C}_2\text{H}_2$ ices. While we do see production of CH_3CN upon irradiation of $\text{NH}_3:\text{C}_2\text{H}_4$ and $\text{NH}_3:\text{C}_2\text{H}_2$ ices, these pathways seem to be more suited to the production of the imine $\text{CH}_3\text{CH}=\text{NH}$ than for the formation of CH_3CN . We also observe that nitrile production is highest at 30 K for both C_2H_2 and C_2H_4 ices, which suggests that CH_3CN production is most efficient at lower temperature. Expanding our experimental parameter space, so repeating the same experiments at lower temperatures (e.g. at 10 K and 20 K), will allow us to further test this hypothesis. In addition, the same experiments could be carried out with different ratios of $\text{NH}_3:\text{C}_x\text{H}_y$ to test the dependence on the initial concentration of reactants. Isotopic substitution of NH_3 and of the hydrocarbon could be used to confirm the identity of our observed products. Alternatively, the electron bombardment (analogous to cosmic rays in the disk) of $\text{N}_2:\text{C}_x\text{H}_y$ ices could be investigated to see if this is a better candidate for explaining the observed CH_3CN abundances in disks. If successful, it would also be interesting to see if the same chemistry produces CH_2CN . Distinguishing between CH_3CN and CH_2CN in a standard reaction set-up is challenging due to their similarities, however, the

CHAPTER 7. CONCLUSIONS

ion CH_2CN^- can be separated from CH_3CN by using Plasma Desorption Mass Spectrometry (Ribeiro et al. 2020).

Appendix A

Additional Experimental Results

.1 Ammonia & Hydrocarbons

.1.1 $\text{NH}_3\text{:C}_2\text{H}_6$

A priori, the feature at 958 cm^{-1} could be due to either C_2H_4 (ethylene), or C_4H_{10} (butane). We distinguish between these two species by analyzing the TPD spectra and we find that the feature at 1435 cm^{-1} and that at 3090 cm^{-1} (both of which are associated with C_2H_4) begin to desorb at 60 K and are fully sublimated by 95 K. This is also the case for the peak at 958 cm^{-1} , therefore we conclude that the peak belongs to C_2H_4 . We are unable to confirm these findings using our data from the QMS, as the m/z values of these species are very similar, and the signal from C_2H_6 drowns out the C_2H_4 signal. Instead, we compare the expected ratio between the relative intensities of the main C_2H_4 and C_2H_6 fragments ($m/z = 28$,

APPENDIX A. APPENDIX

27, 26; obtained from NIST Chemistry WebBook¹) with the ratio of ion currents from our experiments. We expect a 28:27:26 ratio equal to 1:0.37:0.23 for C₂H₆ and 1:0.62:0.58 for C₂H₄. By looking at the TPD traces (shown in Fig .1) for these 3 masses, we calculate a ratio of 1:0.49:0.32. The proportion of mass 27 and 26 both increased by a factor of 1.4 compared to what we would expect for C₂H₆, thus suggesting the presence of another species. We conclude this is C₂H₄. The CH₄ and C₂H₂ features (highlighted in Table 5.1) also disappear in the same temperature range as C₂H₄ and C₂H₆. Once again, the shared m/z fragments do not allow us to distinguish them from their TPD trace. However, we are cautiously confident in our identification as these are often reported as belonging to C₂H₂ and CH₄ in astronomical literature (Bennett et al. 2006; Kim et al. 2010, e.g.,). The growth curves for methane, ethylene are shown in Figure .2 and .3 respectively.

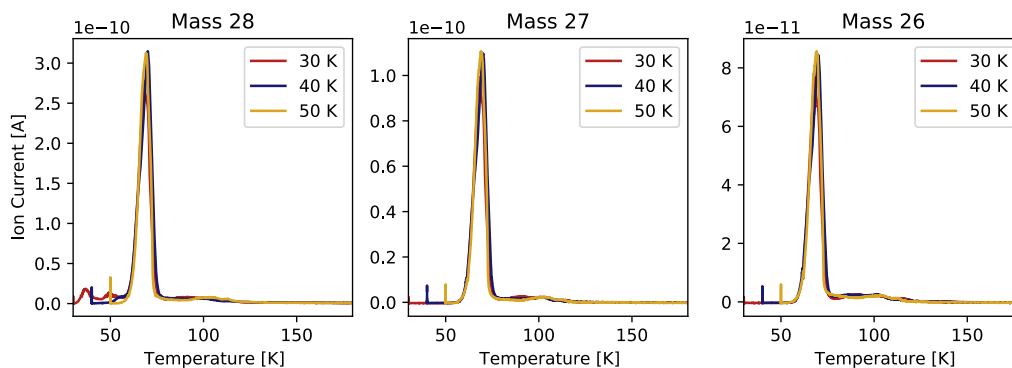


Figure .1 The TPD trace for m/z values 28, 27, 26. To confirm the presence of C₂H₄ in our products we calculate the ratio of the ion current of masses 28:27:26.

¹Available at <https://www.nist.gov>

APPENDIX A. APPENDIX

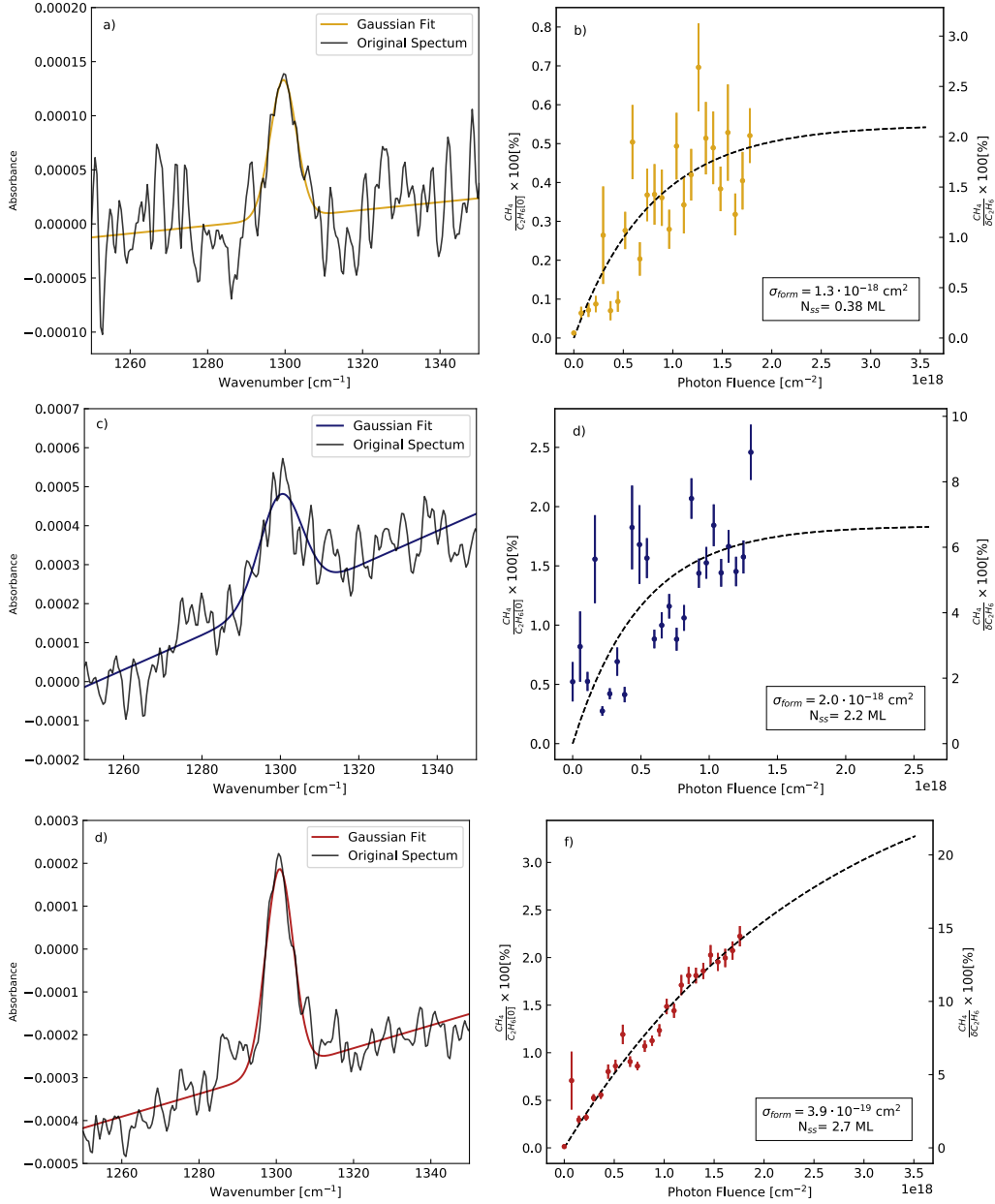


Figure .2 Panel a, c, e) show the Gaussian fitting of the methane peak at 50 K, 40 K and 30 K. Panel b, d, f) show the growth curves for methane during the irradiation of ammonia:ethane ices. The right axis represents the amount of CH₄ formed as a percentage of the initial abundance of ethane. The left axis depicts the amount of methane being produced as a percentage of the depleted ethane.

APPENDIX A. APPENDIX

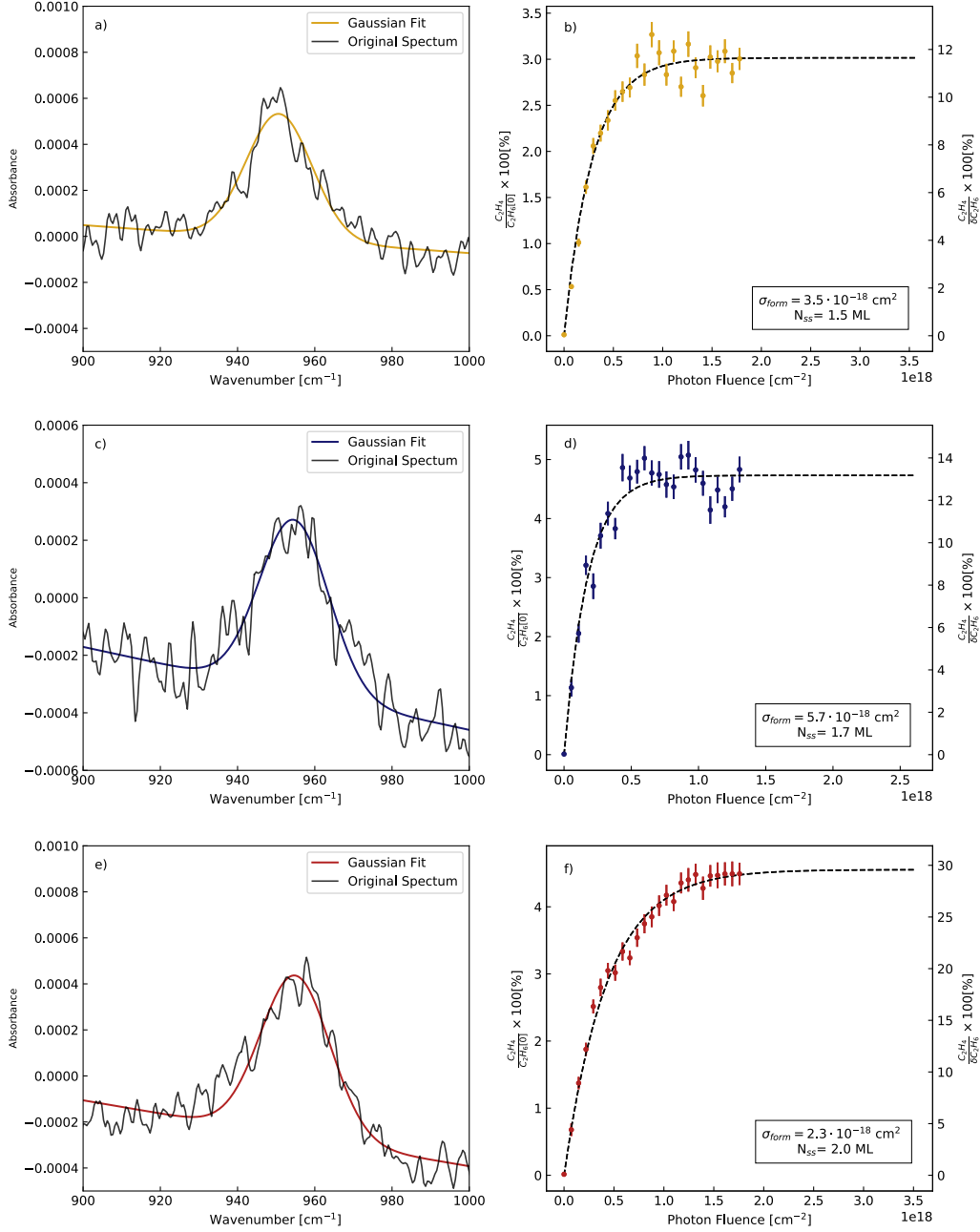


Figure .3 Panel a, c, e) show the Gaussian fitting of the ethylene peak at 50 K, 40 K and 30 K. Panel b, d, f) show the growth curves for ethylene during the irradiation of ammonia:ethane ices. The right axis represents the amount of C₂H₄ formed as a percentage of the initial abundance of ethane. The left axis depicts the amount of ethylene being produced as a percentage of the depleted ethane.

.1.2 NH₃:C₂H₄

The growth curves for methane, ethane and acetylene are shown in Figure .5, .6 and .7 respectively. By observing the spectra in Figure 5.6 and 5.7, we conclude that the most of the new product peaks are the same across temperatures and can be identified with hydrocarbons, especially CH₄ and other alkanes. Ethane and butane are the most likely candidates and we distinguish between the two by looking at the TPD traces. We note that the main mass fragment of butane, $m/z = 43$, presents no signal and therefore we rule out this species. To ensure that the alkane is indeed C₂H₆, we examine the spectra taken during TPD and we see that the IR peaks associated with the alkane disappear in two steps: the greatest desorption occurs between ~ 65 and 80 K, followed by another, significantly smaller desorption wave between 95 K and 102 K. This pattern is matched quite well by the mass fragments 28, 27, 26 (shown in Figure .4) which confirms the identity of C₂H₆ as these are this species' strongest m/z values. After having identified the alkane, we match the other hydrocarbon products to their respective TPD peaks by looking at when each peak disappears in the spectra taken during TPD. The growth curves for the hydrocarbon products are shown in Appendix .1.2.

.1.3 NH₃:C₂H₂

The growth curves for methane, ethane and ethylene are shown in Figure .8, .9 and .10 respectively. We also suspect that a larger, more complex molecule was formed which contained a polyne group. We also see a trace of the radicals at 1230cm⁻¹. These contribute to reactions that lead to the observed products.

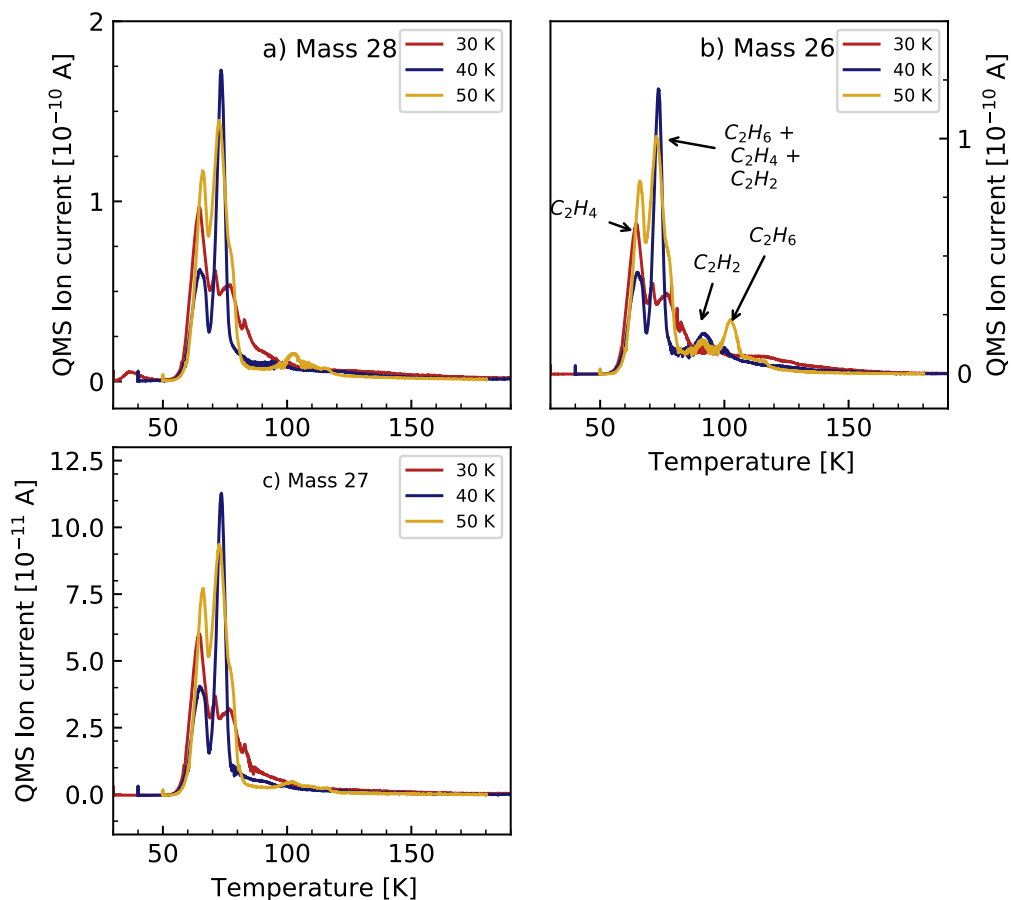


Figure .4 The TPD traces for mass fragments 28, 27, 26. These are the main fragments shared by all the hydrocarbons that we are interested in: C_2H_6 , C_2H_4 and C_2H_2 . Combining the TPD data with the spectra taken during heating, we are able to identify the species giving rise to each peak as shown in Panel b.

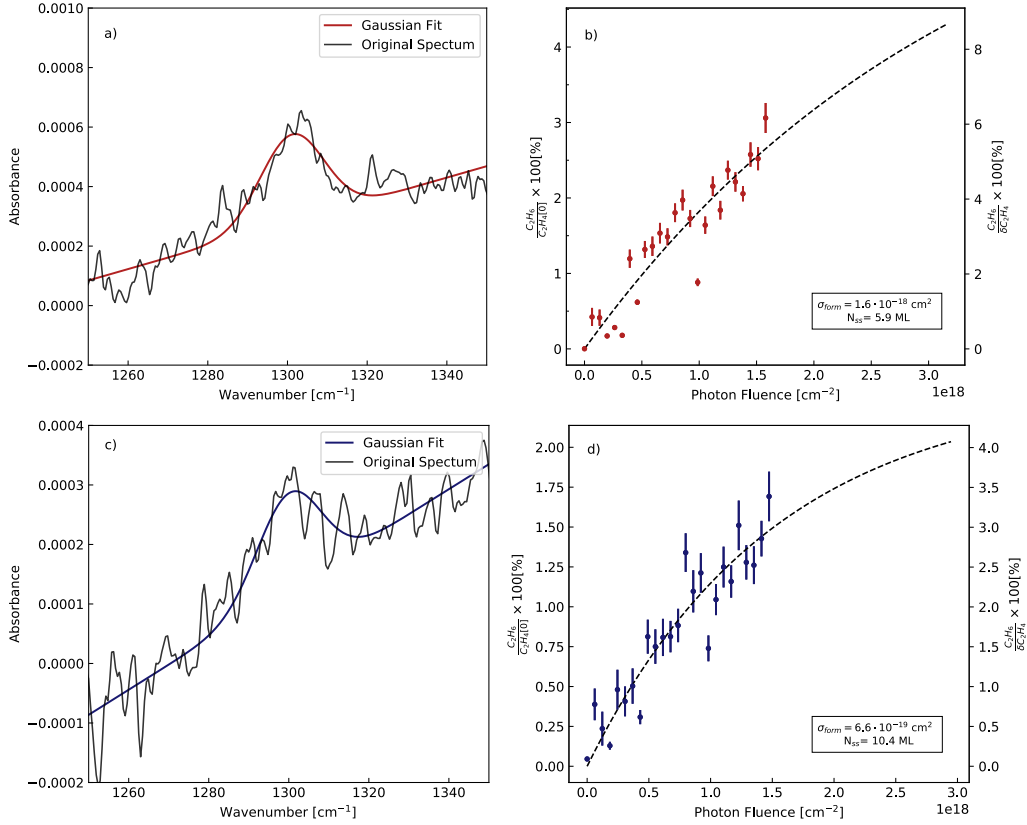


Figure .5 Panel a, c, e) show the Gaussian fitting of the methane peak at 50 K, 40 K and 30 K. Panel b, d, f) show the growth curves for methane during the irradiation of ammonia:ethylene ices. The right axis represents the amount of CH_4 formed as a percentage of the initial abundance of ethylene. The left axis depicts the amount of methane being produced as a percentage of the depleted ethylene.

APPENDIX A. APPENDIX

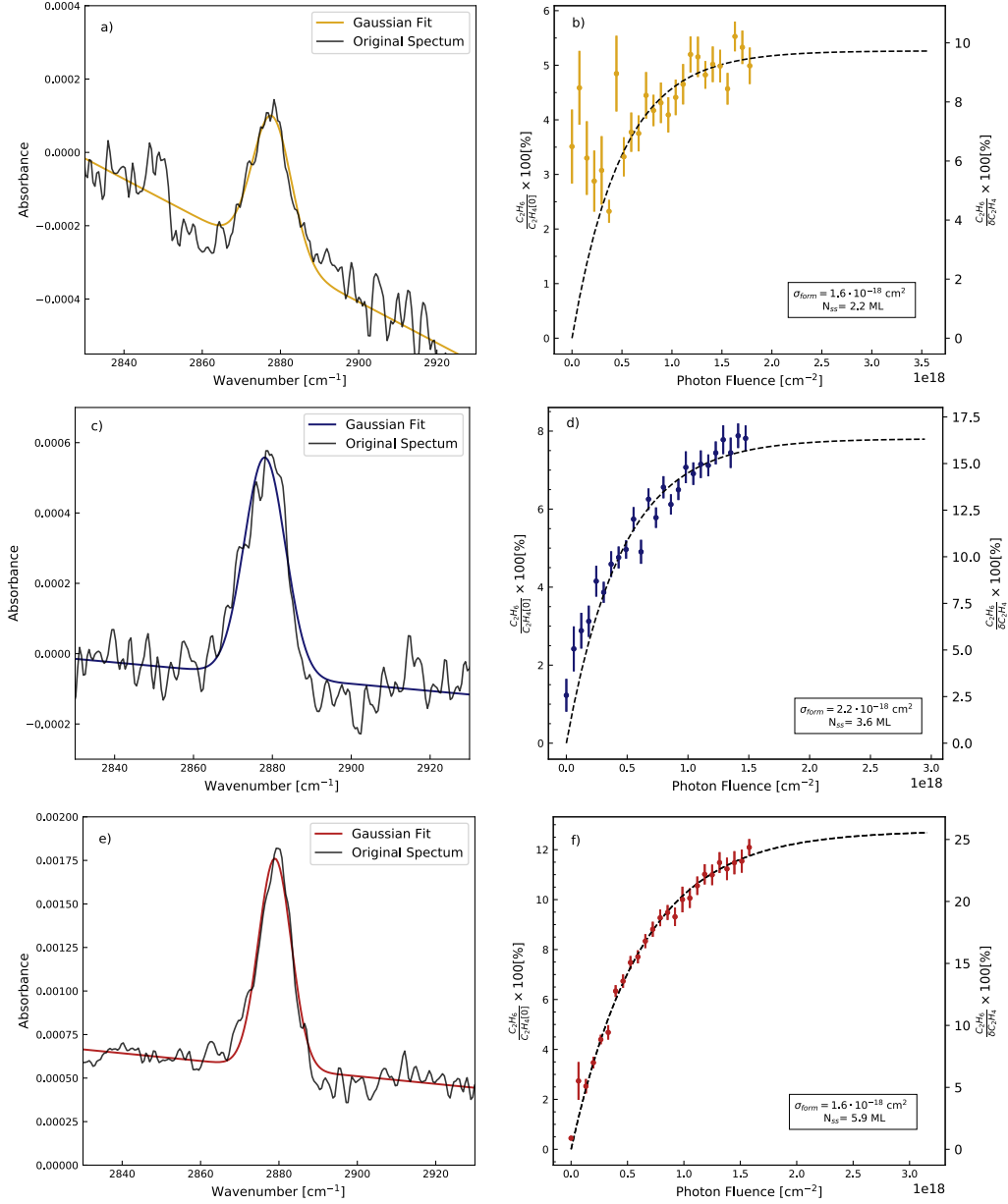


Figure .6 Panel a, c, e) show the Gaussian fitting of the ethane peak at 50 K, 40 K and 30 K. Panel b, d, f) show the growth curves for ethane during the irradiation of ammonia:ethylene ices. The right axis represents the amount of C₂H₆ formed as a percentage of the initial abundance of ethylene. The left axis depicts the amount of ethane being produced as a percentage of the depleted ethylene.

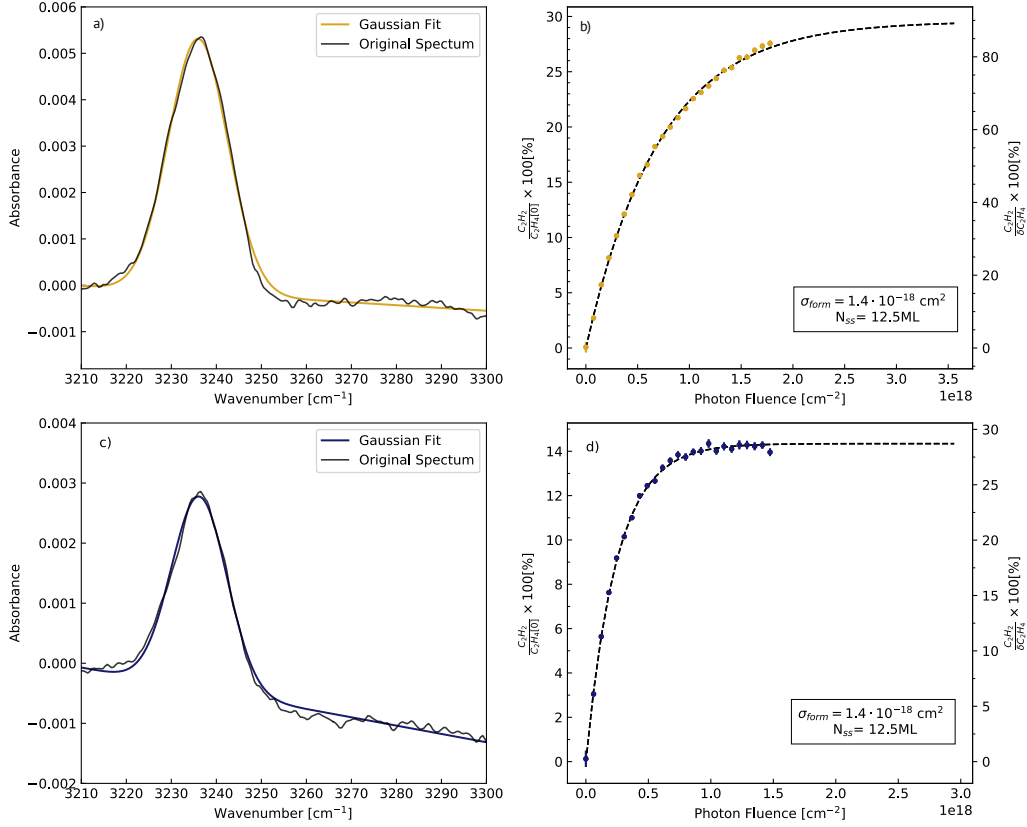


Figure .7 Panel a, c, e) show the Gaussian fitting of the acetylene peak at 50 K, 40 K and 30 K. Panel b, d, f) show the growth curves for C₂H₂ during the irradiation of ammonia:ethylene ices. The right axis represents the amount of C₂H₂ formed as a percentage of the initial abundance of ethylene. The left axis depicts the amount of acetylene being produced as a percentage of the depleted ethylene.

APPENDIX A. APPENDIX

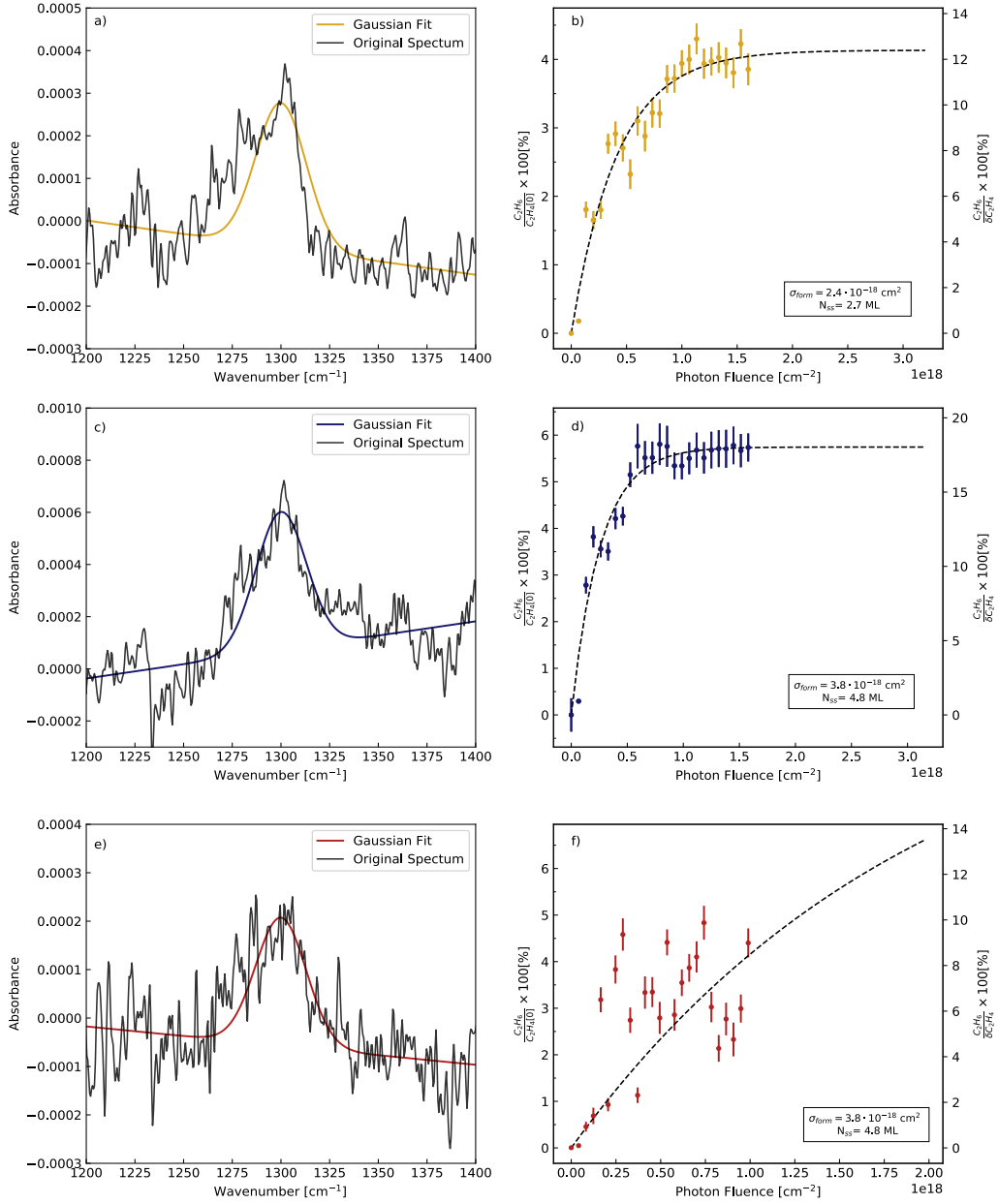


Figure .8 Panel a, c, e) show the Gaussian fitting of the methane peak at 50 K, 40 K and 30 K. Panel b, d, f) show the growth curves for methane during the irradiation of ammonia:acetylene ices. The right axis represents the amount of CH₄ formed as a percentage of the initial abundance of acetylene. The left axis depicts the amount of methane being produced as a percentage of the depleted acetylene.

APPENDIX A. APPENDIX

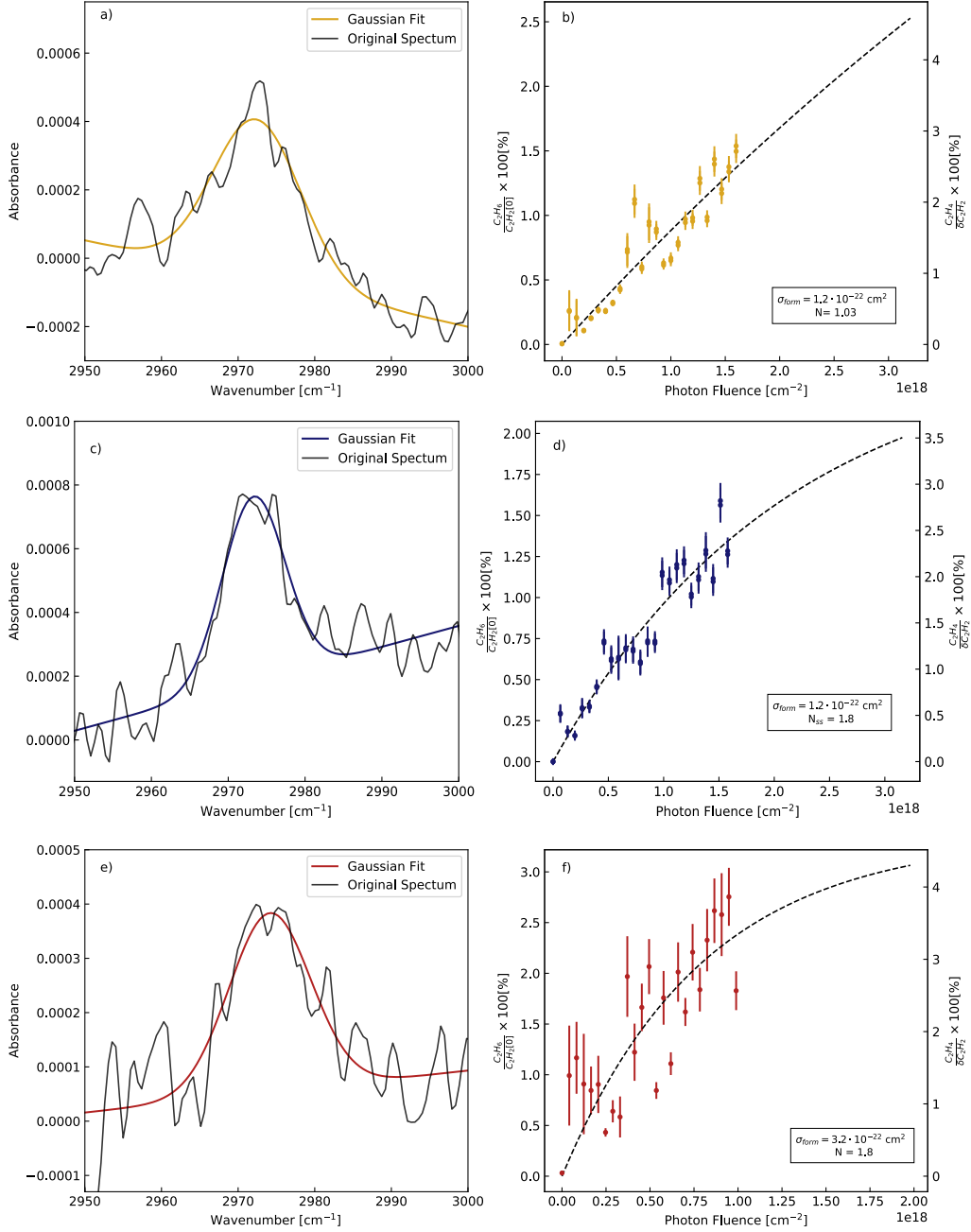


Figure .9 Panel a, c, e) show the Gaussian fitting of the ethane peak at 50 K, 40 K and 30 K. Panel b, d, f) show the growth curves for ethane during the irradiation of ammonia:acetylene ices. The right axis represents the amount of C₂H₆ formed as a percentage of the initial abundance of acetylene. The left axis depicts the amount of ethane being produced as a percentage of the depleted acetylene.

APPENDIX A. APPENDIX

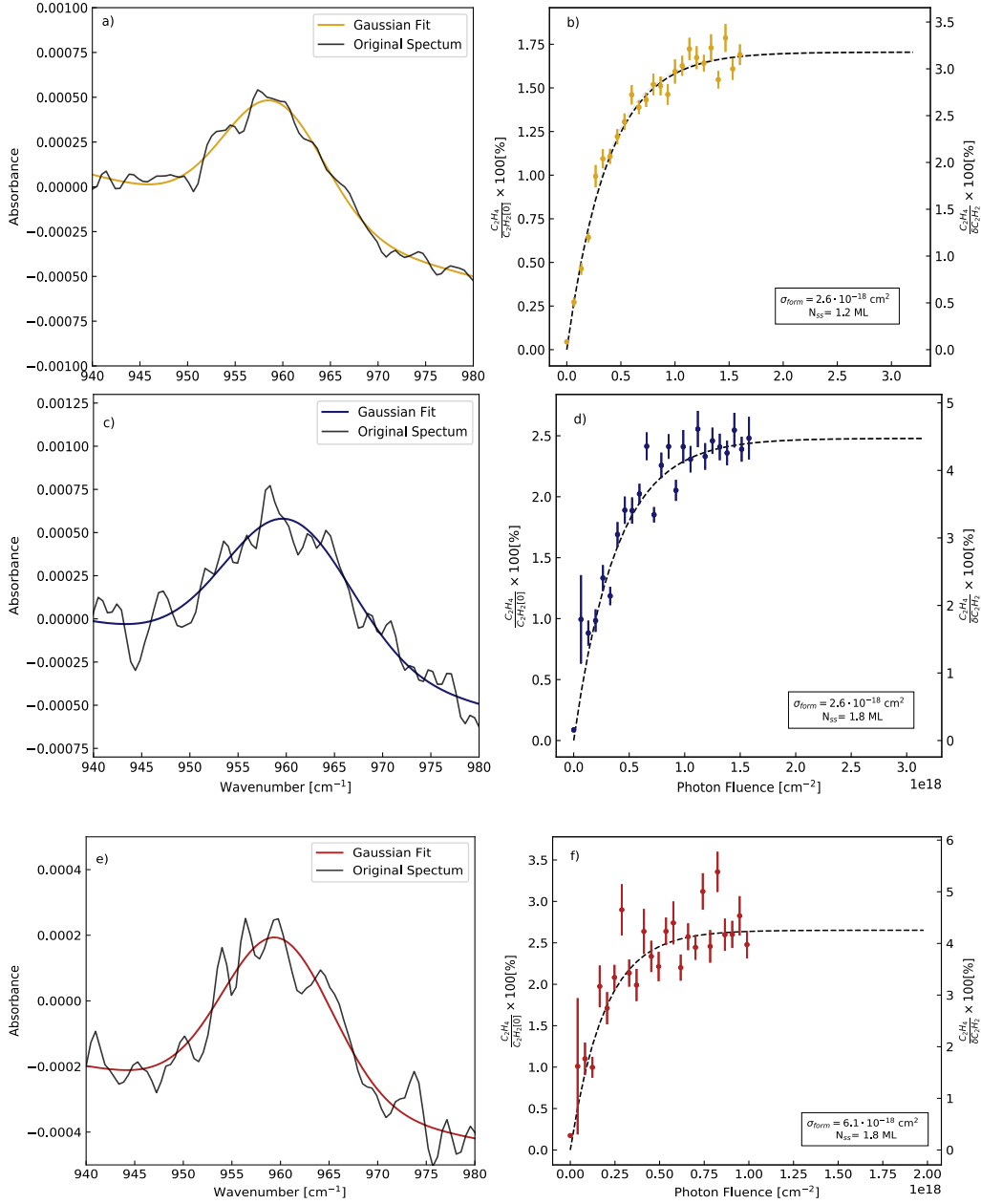


Figure .10 Panel a, c, e) show the Gaussian fitting of the ethylene peak at 50 K, 40 K and 30 K. Panel b, d, f) show the growth curves for ethylene during the irradiation of ammonia:acetylene ices. The right axis represents the amount of C₂H₄ formed as a percentage of the initial abundance of acetylene. The left axis depicts the amount of ethylene being produced as a percentage of the depleted acetylene.

.2 Ethylamine ($\text{CH}_3\text{CH}_2\text{NH}_2$)

Figure .11 shows the pre- and post- irradiation spectra for the 9 hour irradiation of pure ethylamine at 50 K (Panel a) and 70 K (Panel b).

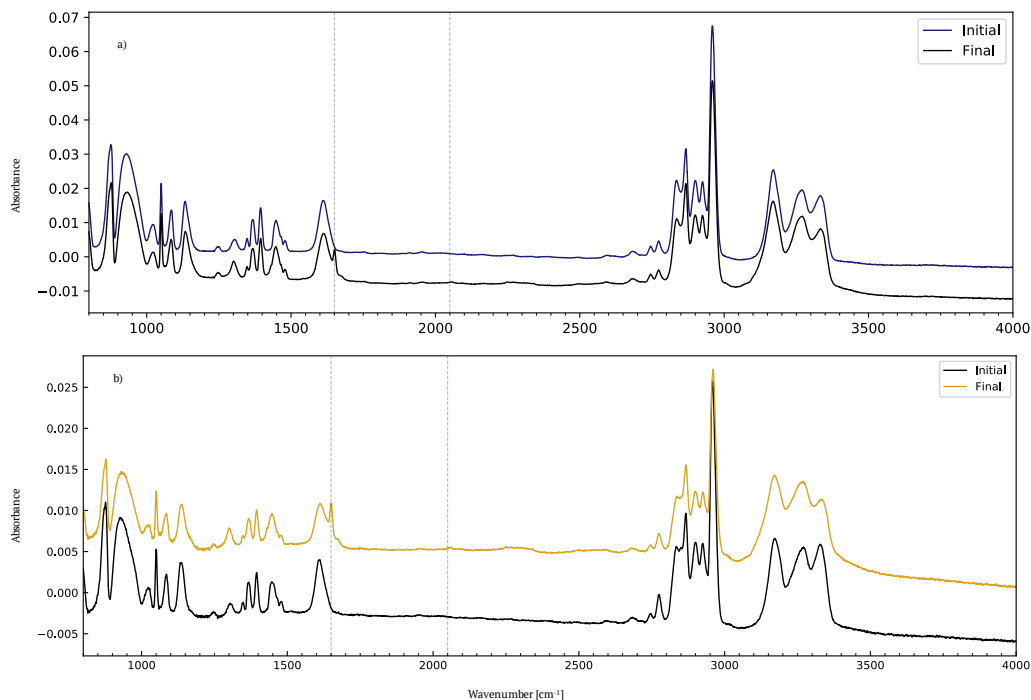


Figure .11 The pre- and post- irradiation spectra for ethylamine at 50 K (a) and 70 K (b)

In both spectra we detect a nitrile peak at 2250 cm^{-1} . We are unable to identify this species as is overlap between the m/z values of ethylamine and both HCN and CH_3CN . However, we are able to identify from the IR spectra that we obtain during TPD, that the peak diappers at $\approx 120\text{ K}$. This does not allow us to confidently distinguish which nitrile has been formed as both candidates have similar desorption temperatures. We use a band strength of $2.2 \times 10^{-18}\text{ cm molecule}^{-1}$ and we obtain

APPENDIX A. APPENDIX

the growth curves shown in Figure .12.

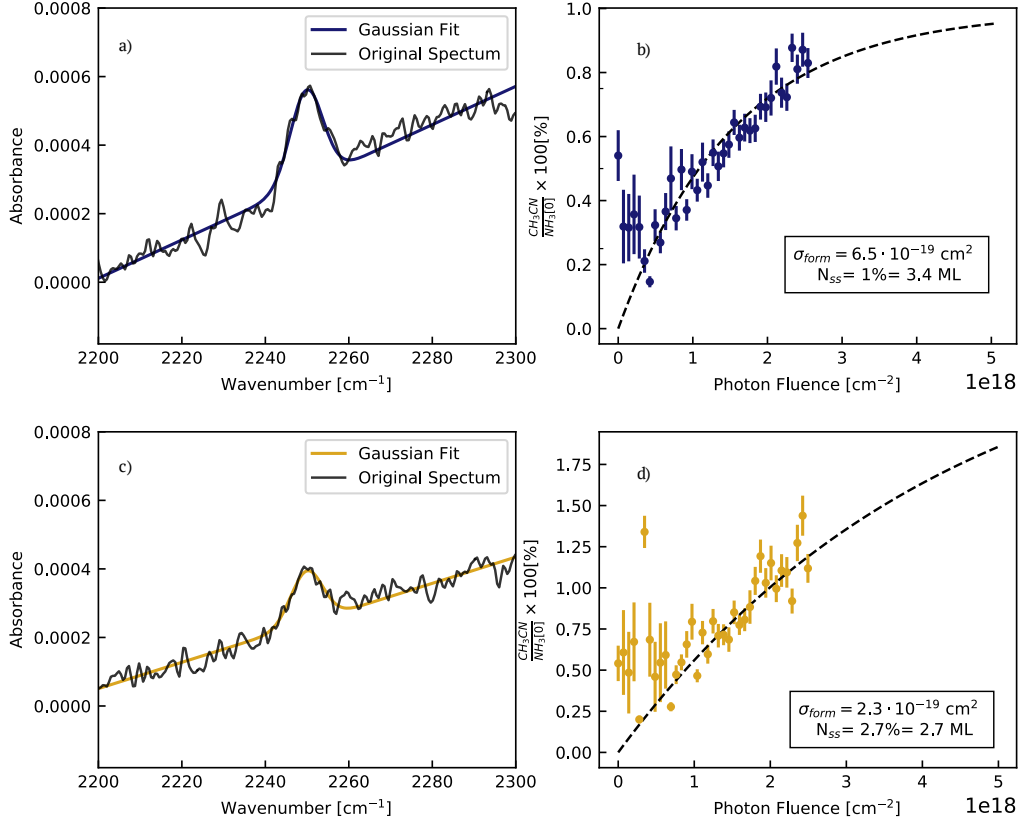


Figure .12 The growth curves for nitriles during irradiation of pure ethylamine ice. Panel a, c) show an example of Gaussian fit. Panel b, d) depict the amount of nitrile formed as a percentage of the initial amount of $\text{C}_2\text{H}_5\text{NH}_2$. The formation cross section, σ_{form} , and the steady state abundance, N_{ss} , both as a percentage of initial ethylene and as an absolute number of monolayers, are also highlighted. Blue represents the experiment at 50 K, whereas yellow is for the experiment at 70 K.

We find a formation cross-section of $6.5 \times 10^{-19} \text{cm}^2$ for the experiment at 50 K, with 3.4 ML forming (1% of the initial amount of ethylamine). For the experiment at 70 K, we obtain a formation cross-section of $2.3 \times 10^{-19} \text{cm}^2$ with a total number of monolayers of nitrile equal to 2.7. This is 2.7% of the initial ethylamine abundance.

APPENDIX A. APPENDIX

Next, we calculate the photodissociation yield, equal to 12% for the experiment at 50 K and 6.1% for the experiment at 70 K. The resulting curves are shown in Figure .13.

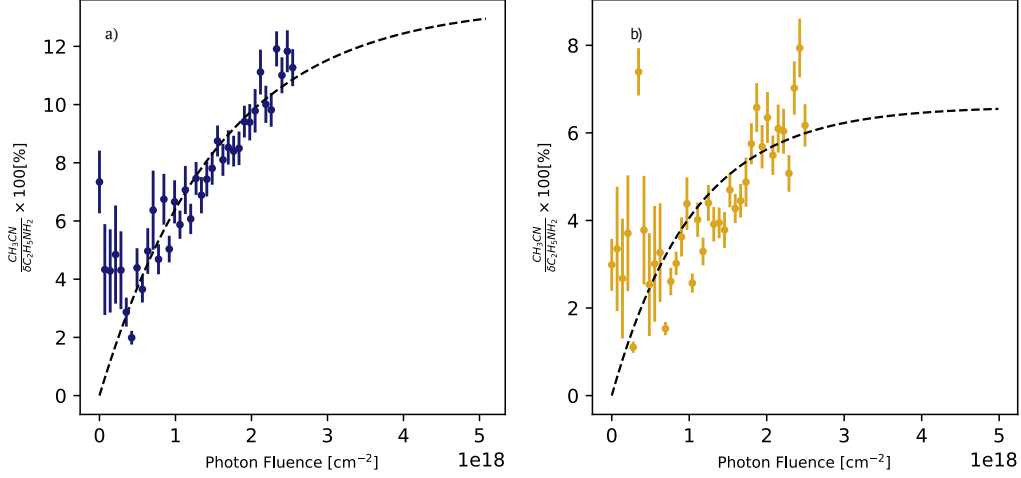


Figure .13 The number of monolayers of the forming nitrile expressed as a percentage of the depleted amine. Panel a) for the experiment at 50 K; panel b) for 70 K

We repeat the same process for the imine peak that we observe (growth curves shown in Figure .14). This results in a σ_{form} of $1.1 \times 10^{-18} \text{ cm}^2$, and we obtained 16 ML which correspond to 6.4% of the initial ethylamine and 87% of the depleted ethylamine (Figure .15) for the 50 K experiment. At 70 K, we obtain a σ_{form} of $1.4 \times 10^{-18} \text{ cm}^2$, with 9.7 ML forming (9.7% of the initial amount of ethylamine). The photodissociation yield for this product is 54%.

Due to the strength of the amine signal and the relative weakness of the signal of the products, we were not able to observe any of the newly formed species. However, we in Figure .16 we present the TPD trace for the strongest ethylamine fragments. We use these to confirm the production of ethylamine during the irradiation of

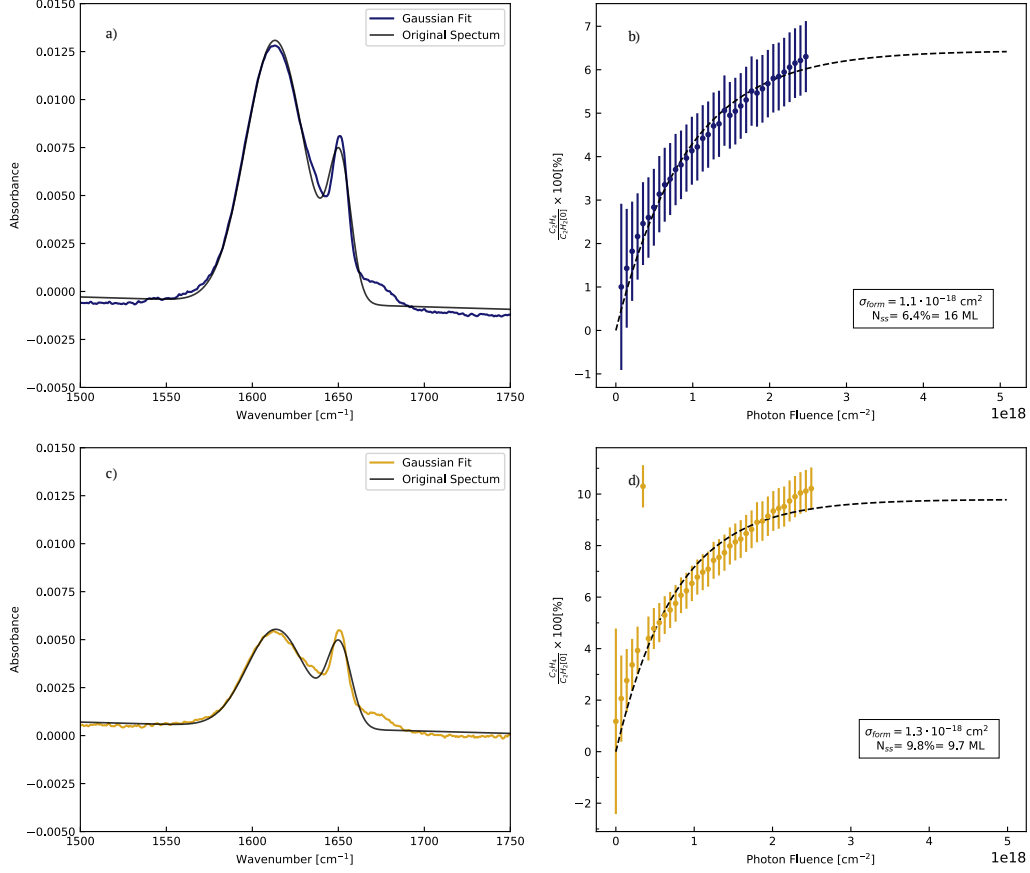


Figure .14 The growth curves for the imine peak during irradiation of pure ethylamine ice. Panel a, c) show an example of Gaussian fit. Panel b, d) depict the amount of imine formed as a percentage of the initial amount of $C_2H_5NH_2$. The formation cross section, f_{form} , and the steady state abundance, N_{ss} , both as a percentage of initial ethylene and as an absolute number of monolayers, are also highlighted. Blue represents the experiment at 50 K, whereas yellow is for the experiment at 70 K.

APPENDIX A. APPENDIX

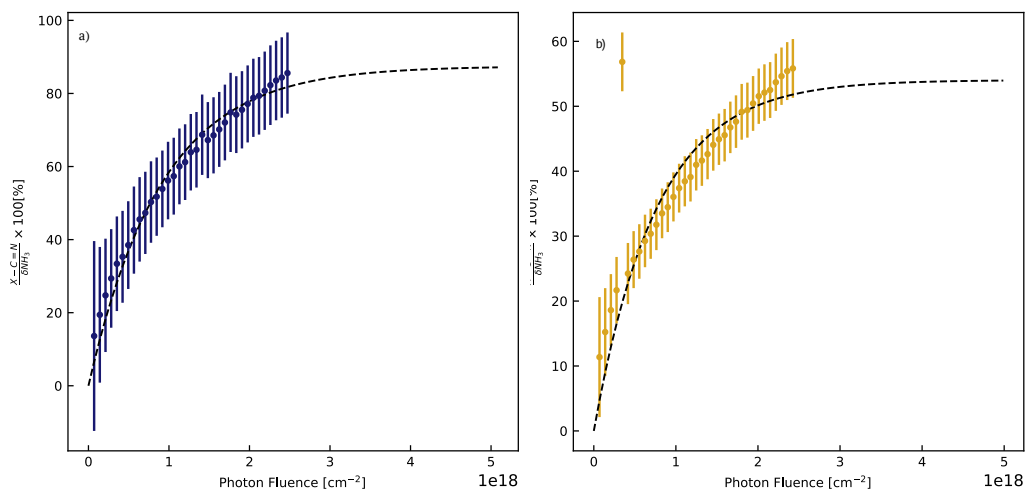


Figure .15 The number of monolayers of the forming imine expressed as a percentage of the depleted amine. Panel a) for the experiment at 50 K; panel b) for 70 K

$\text{NH}_3:\text{C}_2\text{H}_4$ ices.

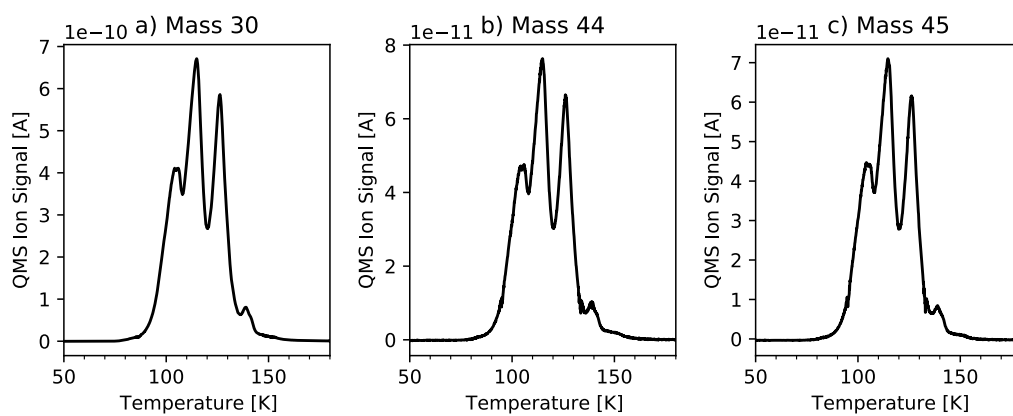


Figure .16 The TPD traces for mass 30, 44, and 45 after the irradiation of pure ethylamine samples. These correspond to the strongest signals in this molecule.

.3 The First Detection of CH₂CN in TW Hya

The observational component of this thesis was also written as a scientific article. It was accepted by *The Astrophysical Journal* and it is currently undergoing revisions before the final submission.

The first detection of CH₂CN in a protoplanetary disk

ALESSANDRA CANTA,¹ RICHARD TEAGUE,¹ ROMANE LE GAL,¹ AND KARIN I. ÖBERG¹

¹Center for Astrophysics / Harvard & Smithsonian, 60 Garden Street, Cambridge, MA 02138, USA

ABSTRACT

In this paper, we report the first detection of the molecule cyanomethyl, CH₂CN, in a protoplanetary disk. Until now, CH₂CN had only been observed at earlier evolutionary stages, in the giant molecular clouds TMC-1 and Sgr 2, and the prestellar core L1544. We detect six transitions of ortho-CH₂CN towards the disk around nearby T Tauri star TW Hya. An excitation analysis reveals that the disk-averaged column density, N_{tot} , for ortho-CH₂CN is $(3.5 \pm 0.3) \times 10^{12} \text{ cm}^{-2}$, which is rescaled to reflect a 3:1 ortho-para ratio, resulting in a total column density of $4.7_{-0.4}^{+0.4} \times 10^{12} \text{ cm}^{-2}$. We calculate a disk-average rotational temperature, $T_{\text{rot}} = 38 \pm 5 \text{ K}$, while a radially resolved analysis shows that T_{rot} remains relatively constant across the radius of the disk. This high rotation temperature suggests that in a static disk and if vertical mixing can be neglected, CH₂CN is largely formed through gas-phase reactions in the upper layers of the disk, rather than solid-state reactions on the surface of grains in the disk midplane. The integrated intensity radial profiles show a ring structure consistent with molecules such as CN and DCN. We note that this is also consistent with previous lower-resolution observations of centrally peaked CH₃CN emission towards the TW Hya disks, since the observed emission gap disappears when convolving our observations with a larger beam size. We obtain a CH₂CN/CH₃CN ratio ranging between 4 and 10. This high CH₂CN/CH₃CN is reproduced in a chemical model of the TW Hya disk that employs standard static disk chemistry model assumptions, i.e. without any additional tuning.

Keywords: astrochemistry — protoplanetary disk — pre-biotic astrochemistry — surface ices — T Tauri stars

1. INTRODUCTION

The composition of planets, and therefore their suitability to host biological life, is largely dictated by the physical structure and chemical composition of ice and dust grains in the protoplanetary disks surrounding young stars (e.g., Nomura et al. 2016; Andrews et al. 2012). Nitriles are of specific interests since they have, in fact, often been identified as key precursors in the synthesis of RNA and amino acids (Powner et al. 2009; Patel et al. 2015). Observations of comets and meteors reveal that molecules such as HCN and CH₃CN were present in the chemical environment of our early Solar Nebula, and were likely available for prebiotic reactions (Mumma & Charnley 2011; Altwegg et al. 2020). Nitrile existence in both our early Solar system and in the disks of young stars has implications for our understanding of the trajectory of the organic chemistry as it evolves during planet formation. This is important to estimate the organic inventory on newly-formed planets and to determine what factors contribute to the chemical habitability of nascent planets (Bergner et al. 2018).

HCN and CN were among the first compounds to be observed in a protoplanetary disk, and since their detection in 1997 over 25 new species have been identified in disks (Kastner et al. 1997; McGuire 2018). However, it was not until the advent of ALMA that more complex molecules such as acetonitrile, CH₃CN, and methanol, CH₃OH, were observed (Öberg et al. 2015; Walsh et al. 2016). Other nitriles that have been detected include HNC and cyanopolyne, HC₃N, as well as various isotopologues of HCN and CN, including H¹³CN, HC¹⁵N, DCN and C¹⁵N (Dutrey et al. 1997; Chapillon et al. 2012; Guzmán et al. 2015; Qi et al. 2003; Hily-Blant et al. 2017). Together these nitriles constitute a substantial fraction of the detected organics in disks, which points to an interesting variations in chemical composition at different stages of a star’s life: the early stellar stages seem to have significantly less oxygen-rich species than protoplanetary disks (Öberg & Bergin 2020). This could be as a result of the oxygen being locked up in molecules such as CO and H₂O and thus unavailable for chemistry, or of a generally oxygen-poor grain-surface chemistry (Öberg & Bergin 2020).

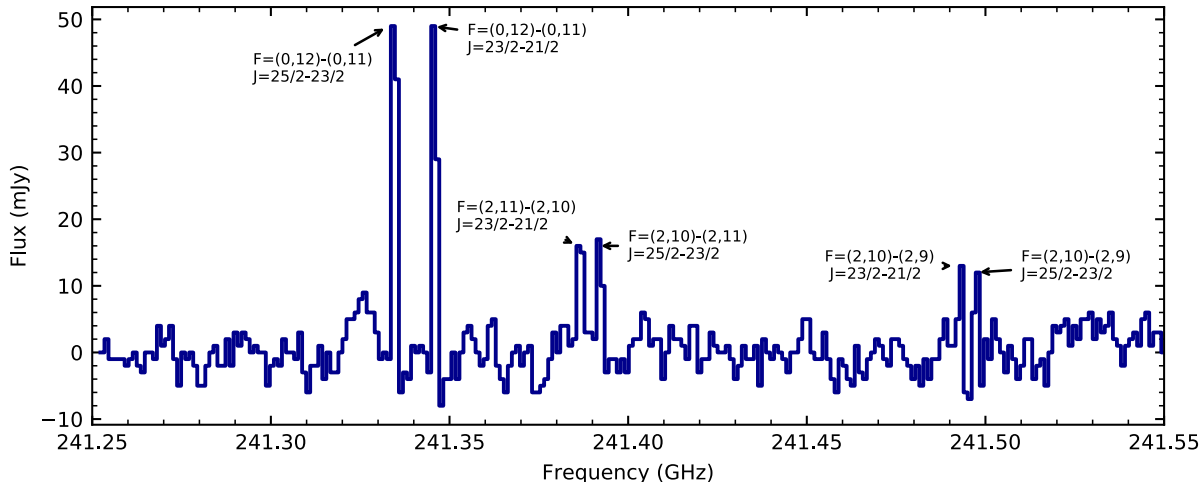


Figure 1. Spectrum of the observed CH_2CN transitions. The 6 brightest peaks are shown with their quantum numbers. The noise is calculated to be 2.9 mJy.

The formation of complex organic molecules (COMs) in protoplanetary disks can happen via two distinct pathways: through grain-surface or gas-phase reactions. Freeze-out reactions on the surface of grains seem to be the greatest contributors to the abundance of COMs in disks, and they involve the absorption of UV radiation from both the central star and the interstellar radiation field (ISRF), formation of radicals and subsequent rearrangement into more complex organics (Oberg 2016). Gas-phase reactions are dominated by a variety of reactions including radiative association (molecules collide and emit a photon), neutral-neutral and neutral-ion reactions and dissociative recombination, where a positive ion recombines with an electron. This was found to be the main reaction pathway for the formation of CH_3CN in TW Hya and of CH_2CN in the protostellar core L1544 (Loomis et al. 2018; Vastel et al. 2015). Whether this is also the case for CH_2CN in disks has not previously been possible to evaluate since there have been no reported observations of this molecule.

In this paper, we report the first observation of the molecule CH_2CN (in its ortho state) in a protoplanetary disk, specifically in the disk around the nearby T Tauri star TW Hya. This molecule has previously been observed in diffuse molecular clouds SgrB2 and TMC-1, and in the pre-stellar core L1544, but never in a protoplanetary disk (Vastel et al. 2015; Irvine et al. 1988). TW Hya is a $\sim 0.8M$ solar-like T Tauri star that is often used in astrochemical observations because of its proximity (60.1 pc Bailer-Jones et al. 2018) and its face-on orientation, $i \approx 5^\circ$, which allows for easier interpretation of the data. The details of the detection, the data reduction and the observational results are outlined in §2. In §??, we proceed by using a disk-averaged rotational

diagram analysis to obtain the total column density, N_t and an excitation temperature, T_{rot} . We also perform a radially resolved analysis to obtain radial profiles for our T_{rot} and N_t . In §4 we compare our findings to a chemical model of TW Hya, which we use to complement our discussion of the chemistry of both CH_3CN and CH_2CN . Finally, we present a summary of our findings in §5.

2. OBSERVATIONS

These observations were taken as part of an ALMA project 2018.A.00021 (PI: Teague). The correlator set-up included a single frequency divided mode (FDM) window centered on 241.5 GHz to provide continuum on which to self-calibrate. In this window six strong emission lines were detected and identified as CH_2CN lines, and a single C_{34}S line.

2.1. Data Reduction

The data consists of six executions, two in a compact configuration with baselines spanning 15 m – 500 m on April 4th 2019, and four in a more extended configuration with baselines ranging between 15 m and 2.62 km on September 29th 2019. The shorter baseline executions included 41.7 minutes on-source integration while the longer baseline executions used 51.1 minutes on-source for a total on-source time of 4.9 hours. The quasar J1037-2934 was used for both bandpass and flux calibration for all executions while the phase calibration was performed with J1147-3812 for the short baseline data and J1126-3828 for the long baseline data.

Initial calibration was performed using the standard pipeline procedure in CASA v5.6.2 (McMullin et al. 2007). The data were then self-calibrated following the self-calibration procedure used in the DSHARP program

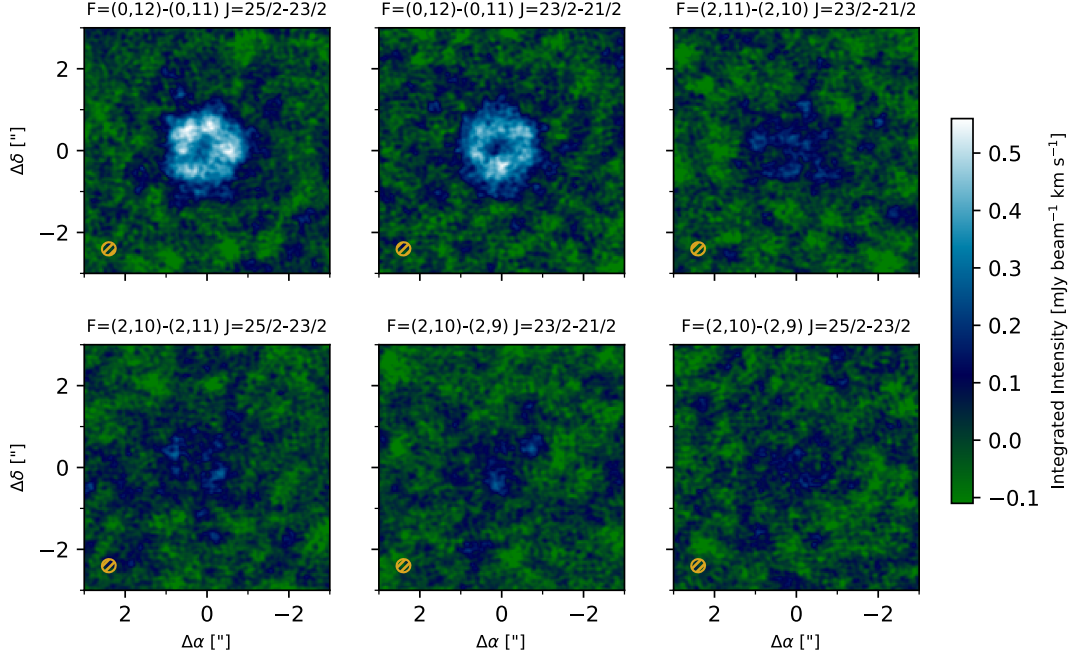


Figure 2. Integrated intensity images of individual observed transitions. All the panels share the same intensity scale. The synthesised beam is shown in the bottom left corner. We find σ to be $0.06 \text{ mJy beam}^{-1} \text{ km s}^{-1}$.

Table 1. Observed CH_2CN Transitions

$N' - N''$	K_a	K_c	$J' - J''$	ν_0	g_u	A_{ul}	$S_{ij} \mu^2$	E_{upper}	Int. Flux Density
				(GHz)		(s^{-1})	(D^2)	(K)	(mJy km s^{-1})
12-11	0 - 0	12 - 11	25/2 - 23/2	241.3335423	234	9.62×10^{-4}	1376.0	75	126.1 ± 6.0
12-11	0 - 0	12 - 11	23/2 - 21/2	241.3458390	216	9.59×10^{-4}	1265.6	75	109.3 ± 6.0
12-11	2 - 2	11 - 10	23/2 - 21/2	241.3860255	216	9.33×10^{-4}	1230.5	128	43.4 ± 6.0
12-11	2 - 2	11 - 10	25/2 - 23/2	241.3913950	234	9.36×10^{-4}	1337.7	128	37.8 ± 6.0
12-11	2 - 2	10 - 9	23/2 - 21/2	241.4925510	216	9.34×10^{-4}	1230.6	128	25.2 ± 6.0^a
12-11	2 - 2	10 - 9	25/2 - 23/2	241.4970603	234	9.37×10^{-4}	1337.7	128	25.2 ± 6.0

NOTE—All data for column $N''-N''$ through to E_{upper} was obtained from The Cologne Database for Molecular Spectroscopy (CDMS; Müller et al. 2001).

^aThis peak includes two distinct transitions: the one that we observe and the another one associated with para- CH_2CN . The latter has a significantly lower A_{ul} ($\sim 3.5 \times 10^{-6} \text{ s}^{-1}$), thus we assume that all the integrated flux observed comes from the ortho line Endres et al. (2016).

(Andrews et al. 2018). In brief, all spectral windows were used, masking out any lines in each spectral window. These line-free observations were used to solve for the phase solutions which were then applied to the entire dataset. Prior to combining the different executions, the executions were aligned to the same phase center and the continuum fluxes were compared. All executions yielded fluxes that were within 2% of one another, except for the final long baseline execution which varied by about 10%.

The final long baseline execution was rescaled using the `gaincal` task such that the total flux matched that of the other three long baseline executions. The continuum was subtracted using the `uvcontsub`.

The continuum FDM window was imaged using the multi-scale CLEAN algorithm and adopting a Briggs weighting with a robust parameter of 2 (similar to natural weighting) yielding a synthesized beam of $0''.34 \times 0''.32$ at a position angle of 104.8° . The data was imaged at

the native spectral resolution of the FDM window of 1.4 km s^{-1} .

Figure 1 shows the six detected transitions in the form of three sets of doublets with their associated quantum labelling. These are also depicted as integrated intensity (moment-0) maps in Figure 2. While four of the six lines are fairly weak, the two at 241.3335423 and 241.3458390 GHz are robustly detected, exhibiting a clear ring morphology. To better visualize the CH_2CN morphology, we create a high signal-to-noise map by stacking the 6 transitions together. The resulting image is shown in the left panel of Figure 3.

For a more direct comparison with the results presented in Loomis et al. (2018), we create a version of the images which were smoothed to the same spatial resolution, $1''.05 \times 0''.83$, using the `imsmooth` task in `CASA`. As the weaker transitions are more clearly detected in the smoothed images, we use the smoothed images for both the radially-resolved analysis in §3.3 and the disk-averaged analysis in §3.2. The higher spatial resolution data is only used in the plotting of the channel maps (Figure 2) and of the radial profile in Figure 3) to better constrain the ring morphology.

2.2. Observational Results

The disk-averaged integrated flux measurements reported in Table 1 were obtained by integrating the peaks highlighted in Figure 1 over the two independent 1.5 km/s channels showing emission out to $\sim 2.5''$ (where the intensity reaches 0 in the right panel of Figure 3). Under the assumption of spectrally independent pixels, the uncertainty in the integrated flux is calculated using the equation:

$$\delta M_0 = \sqrt{\sum_{i(I_i > 0)}^N \sigma_i^2 \cdot \Delta v_{\text{chan},i}^2}, \quad (1)$$

where δM_0 indicates the uncertainty in moment-zero (integrated intensity) values; σ_i is the signal-to-noise ratio in the spectrum; and $\Delta v_{\text{chan},i}$ is the channel width (Teague 2019).

We plot radial profiles to see how the integrated flux changes over the radius of the disk. We radially bin the integrated flux from each transition into $0.05''$ ($\sim 3 \text{ au}$)-wide bins. The beam size was $0.3''$ ($\sim 18 \text{ au}$), therefore our chosen bin size is a sixth of the beam major FWHM. We use a position angle of 152° and an inclination, $i = 5^\circ$ (Huang et al. 2018). We use the native resolution data to plot the radial profile in Figure 3, which shows the ring morphology quite clearly. For the purpose of our excitation analysis, however, we use the lower spatial resolution smoothed data, with the radial profiles from

the individual transitions using this data set shown in Fig. 4B.

The stacked image radial profile shows a ring morphology (Figure 2, which is also observed in the individual transitions in Fig 3. We fitted the radial profile in Figure 3 with a Gaussian function (right panel of Figure 3) to infer the location of the center of our ring and the ring width. We find the center to be at $0.4''$ ($\sim 24 \text{ au}$) and, full width at half maximum of $1.1''$ ($\sim 69 \text{ au}$). We also see some excess emission between $1.5''$ and $2.5''$ when compared to a single Gaussian ring, however, further characterisation of this feature requires more sensitive observations.

In contrast to the native resolution data, the smoothed data appears to be consistent with a centrally-peaked morphology which is also seen with CH_3CN (Loomis et al. 2018). The similar distribution suggests a chemical link between the two molecules, which is explored further in Section 4.

3. CH_2CN EXCITATION ANALYSIS

The rotational temperature and the total column density of CH_2CN can be constrained through the use of a rotational diagram analysis. This implicitly assumes that the molecular excitation can be described by a single temperature and that the molecules are in local thermodynamic equilibrium (LTE). These parameters allow us to draw conclusions about the physical conditions where CH_2CN is found and its potential interactions with molecules that exist in a similar environment.

3.1. Method

We start our analysis by constraining the disk-averaged rotational temperature, T_{rot} , and the total column density, N_{tot} . Following Goldsmith & Langer (1999), we obtain the rotational diagram shown in Figure 4A by using the equation

$$\ln \frac{N_u}{g_u} + \ln C_\tau = \ln N_{\text{tot}} - \ln Q(T_{\text{rot}}) - \frac{E_u}{kT_{\text{rot}}}, \quad (2)$$

where N_u is the the column density of molecules in the upper state of each transition, C_τ is the optical correction factor, and $Q(T_{\text{rot}})$ is the molecular partition function and E_u is the upper state energy. We use the molecular partition function from The Cologne Database for Molecular Spectroscopy (CDMS; Müller et al. 2001)¹ using a linear interpolation to obtain our Q values (Endres et al. 2016). Degeneracies due to the hyperfine structure are included in the calculation of Q .

¹ Available at <https://cdms.astro.uni-koeln.de>.

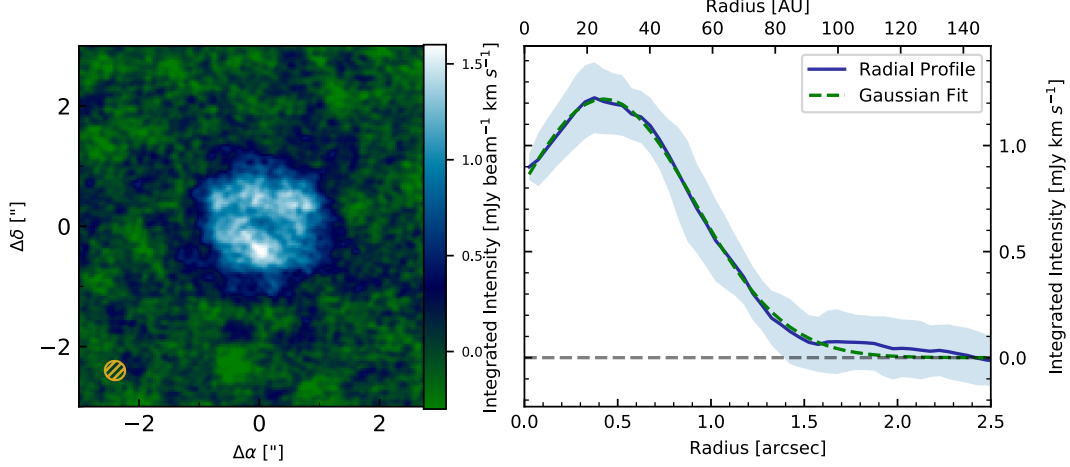


Figure 3. Left panel: Integrated intensity map made from the stacked 6 transitions. The noise is calculated to be $0.14 \text{ mJy beam}^{-1} \text{ km s}^{-1}$. Right panel: the azimuthally averaged integrated intensity radial profile obtained from the stacked native resolution data. Shaded areas represent 1σ uncertainties, where σ represents the standard deviation in each radial bin.

We calculate the N_u for each transition through the equation:

$$N_u = \frac{4\pi S_\nu \Delta v}{A_{ul} \Omega h c}, \quad (3)$$

where A_{ul} is the Einstein coefficient, S_ν is the disk-averaged integrated flux density calculated as described in §2.2 and using a bin-size of $2.5''$, Δ is the width of the two channels that we used for integration and Ω is the solid angle subtended by the source.

The optical correction factor is obtained through the equation:

$$C_\tau = \frac{\tau}{1 - e^{-\tau}}. \quad (4)$$

where the optical depth, τ , can be related to the upper level population through the equation:

$$\tau_{ul} = \frac{A_{ul} c^3}{8\pi \nu^3 \Delta v} N_u (e^{h\nu/kT_{rot}} - 1). \quad (5)$$

Given that our emission is dominated by Doppler broadening, the line width, Δv , is given by

$$\Delta v = \sqrt{\frac{2kT_{rot}}{m_u m_H}}, \quad (6)$$

with m_u being the molecular weight of CH_2CN (40 g/mol) and m_H being the mass of a hydrogen atom.

We create a model that relates N_u , C_τ and Δv to Equation 2 and we derive the values of T_{rot} and N_{tot} by matching the observed N_u/g_u values. We use Scipy's `curve_fit` function to minimize χ^2 -squared and find the best estimate of our desired parameters (Jones et al. 2001). $\ln(N_u/g_u)$ can then be plotted against the upper state energies, E_u to obtain Figure 4A, where the

slope and the y -intercept of the line respectively represent $-T_{rot}^{-1}$ and N_{tot} .

3.2. Disk-averaged Analysis

We obtain a disk-averaged rotational temperature of $38 \pm 5 \text{ K}$ and a disk-averaged total column density of $(3.5 \pm 0.3) \times 10^{12} \text{ cm}^{-2}$ for ortho- CH_2CN . As described in Le Gal et al. (2017), for a molecule containing 2 identical Hydrogen nuclei, such as CH_2CN , we expect a statistical ortho/para ratio of 3:1, and therefore we infer a total column density of $4.7 \times 10^{12} \text{ cm}^{-2}$.

Finally, having obtained T_{rot} , we calculate the optical depth, τ , of our transitions. In all cases, we obtained a value of $\tau \ll 1$, with values of range 4×10^{-4} to 3.4×10^{-3} . Therefore, our detected transitions were of negligible optical thickness. The disk-averaged values obtained in Section 3.1 are calculated out to a radius of $2.5''$. However, we can see from Figure 4B that the weaker emission lines are almost completely lost at $1.75''$. As a comparison, we calculate an average T_{rot} and N_t for the inner region of the disk where all six transitions are detected. For this, we integrated out to a radius of $1.75''$. For this inner region, we find a total column density of $(8.4 \pm 0.7) \times 10^{12}$ ($(6.3 \pm 0.5) \times 10^{12}$ for ortho- CH_2CN) cm^{-2} , and a rotational temperature of $40 \pm 5 \text{ K}$. Comparing the total column density that we obtained out to a radius $1.75''$ to that out to $2.5''$ confirms that the outer radii are contributing very little to the total column density, as we would expect from the radial profiles in Figure 4B and in the right panel of Figure 3.

3.3. Radially Resolved Analysis

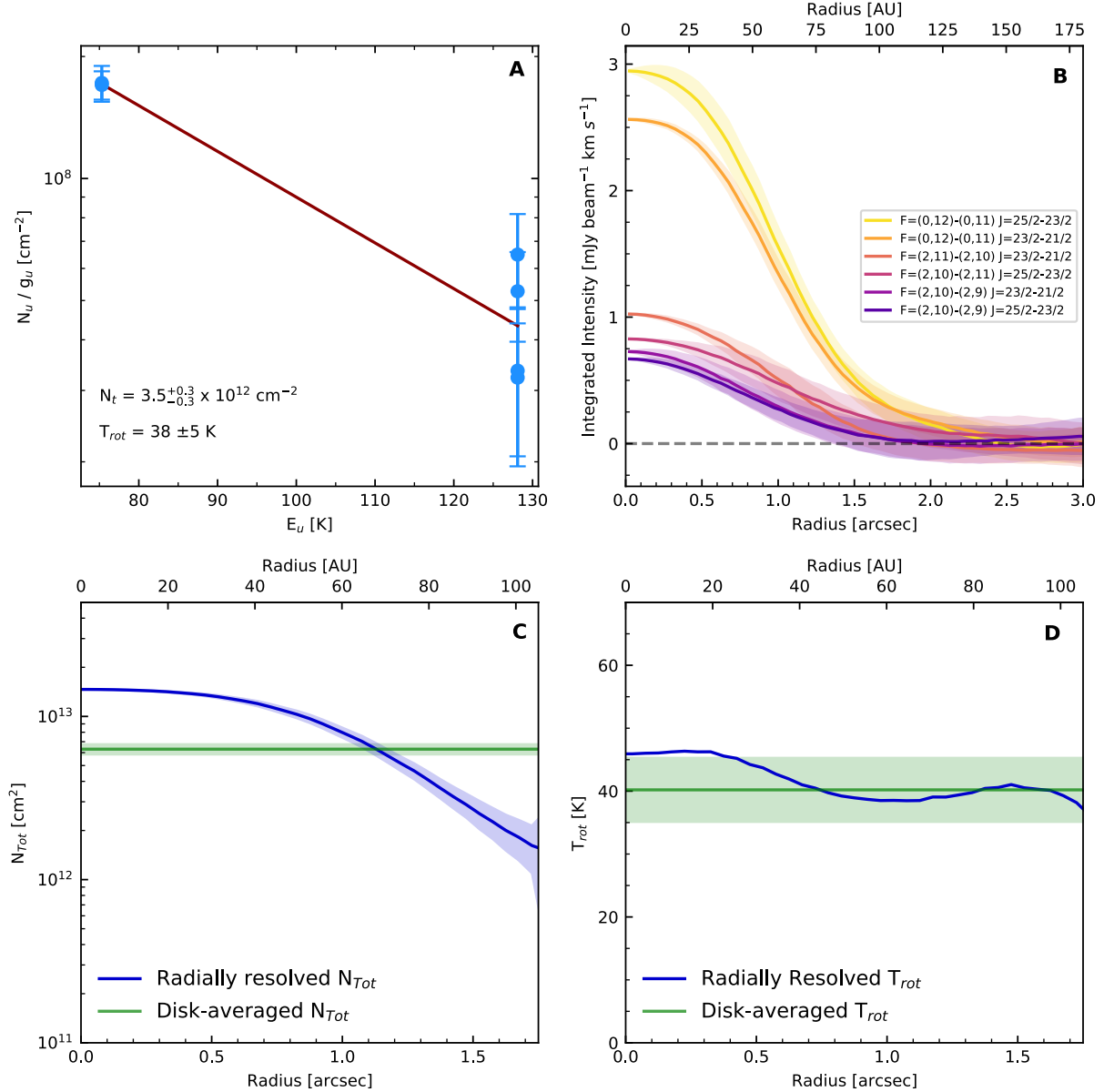


Figure 4. Panel A: ortho-CH₂CN disk-averaged rotational diagram. Panel B: the radial profiles for the six detected transitions. Shaded areas represent 1σ uncertainties. Panels C & D: radial profiles of respectively the CH₂CN total column density and the rotational temperature. The colour dark blue indicates radially resolved values, whereas green is used for values we obtained from disk-averaged analysis. Shaded areas represent 1σ uncertainties.

To further observe the behaviour of T_{rot} and N_t across the disk, we use the radial integrated intensities from each of the transitions in Figure 4B and we repeat the steps outlined in Section 3.2 to obtain rotational diagrams at different radii. The results are summarised in panel 4C and D.

Figure 4C shows that the column density decreases from 5×10^{13} to 0.6×10^{13} across the radius of the disk. This is consistent with the disk-averaged column density. The T_{rot} ranges between 45 and 37 K, which is consistent with the disk-averaged T_{rot} (38 ± 5 K). We note that this

is very similar to the CH₃CN excitation temperature of $32.7^{+3.9}_{-3.4}$ K in the same disk (Loomis et al. 2018). On the other hand, the column density of CH₃CN, $1.82^{+0.25}_{-0.19} \times 10^{12}$, is ~ 10 times lower than our observed CH₂CN's N_t . This is consistent with our chemical model, as discussed in Section 4.1.

4. DISCUSSION

4.1. CH₂CN/CH₃CN Ratio & Disk Models Results

We use the chemical models by Le Gal et al. (2019) to explore the predicted column densities of CH₂CN and

Table 2. Formation and destruction pathways for CH₂CN

Reaction Type	Reactants			Products		Mechanism	Rates of Reaction			
							α [cm^3s^{-1}]	β	γ	k rate type ^c
Formation	CN	CH ₃	→	H	CH ₂ CN	Neutral-Neutral	1.00(−10)	0.00	0.00	(1)
	N	C ₂ H ₃	→	H	CH ₂ CN	Neutral-Neutral	6.40(−11)	0.17	0.00	(1)
	C	CH ₂ NH	→	H	CH ₂ CN	Neutral-Neutral	1.00(−10)	0.00	0.00	(1)
	CH ₃ CN ⁺	e [−]	→	H	CH ₂ CN	DR ^a	2.00(−7)	−0.50	0.00	(1)
	CH ₃ CNH ⁺	e [−]	→	2 H	CH ₂ CN	DR ^a	8.00(−8)	−0.50	0.00	(1)
	s-CN ^b	s-CH ₂ ^b	→		CH ₂ CN	Grain Surface				
Destruction	CH ₂ CN	C ⁺	→	C	CH ₂ CN ⁺	Ion-Polar	1.00	1.61(−9)	5.81	(2)
	CH ₂ CN	H ₃ ⁺	→	H ₂	CH ₃ CN ⁺	Ion-Polar	1.00	2.94(−9)	5.81	(2)
	CH ₂ CN	hν	→	CN	CH ₂	Photodissociation	1.56(−9)	0.00	1.95	(3)
	CH ₂ CN	hν	→	CH ₂ CN ⁺	e [−]	Photodissociation	5.29(−10)	0.00	3.11	(3)
	CH ₂ CN		→	s-CH ₂ CN ^b		Freeze-out				

NOTE—Table showing all the possible formation and destruction pathways of CH₂CN based on the astrochemical disk model by [Le Gal et al. \(2019\)](#). The rates of reactions are reproduced from the Kinetic Database for Astrochemistry available at <http://kida.astrophy.u-bordeaux.fr> ([Wakelam et al. 2012](#)).

^aDR = Dissociative Recombination

^bs- indicates solid-state reactions, i.e. reactions occurring on the surface of grains.

^cRate formulae (1) Modified Arrhenius Equation $k(t) = \alpha(T/300)^\beta e^{-\gamma/T}$ (2) Ion-polar rate coefficient computed using Su-Chesnavich capture approach $k(t) = \alpha\beta(0.62 + 0.4767\gamma(T/300)^{0.5})$ ([Woon & Herbst 2009](#)) (3) Photo-dissociation reaction rate $k(t) = \alpha e^{-\gamma A_v}$ where A_v is the visual extinction ([Draine 1978a](#); [van Dishoeck 1994](#)).

CH₃CN as a function of radius, as shown in Figure 5. The original model has been modified to fit TW Hya using the physical parameters described in Table 3, and uses a C/O ratio of 1. The model is in good accordance with our observations as it predicts that CH₂CN is more abundant than CH₃CN at all radii. However, the CH₂CN/CH₃CN ratio in the model is larger than the ratio of ~ 10 we found observationally. Inspecting Fig. 5, we see that the model correctly predicts the column density of CH₂CN and under-predicts that of CH₃CN. This suggests that while the column density of CH₂CN is well reproduced by standard astrochemical model assumptions, there are missing chemical pathways that lead to the formation of CH₃CN. Detailed astrochemical disk modeling effort needs to be made to further constrain the main reaction pathways driving both the observed CH₃CN abundance and CH₂CN/CH₃CN ratio in the TW Hya protoplanetary disk, but they are beyond the scope of this paper.

4.2. CH₂CN Chemistry

Formation of molecular species in protoplanetary disks can occur via two distinct routes: gas-phase and grain-surface reactions, and in the case of CH₂CN both pathways are a priori possible. Based on the astrochemical disk model of [Le Gal et al. \(2019\)](#), several formation

Table 3. Physical parameters used for the disk chemistry modeling

Parameters	TW Hya ^a
Stellar mass: M_\star (M_\odot)	0.8
Characteristic radius: R_c (AU)	10
Density power-law index	1.5
Midplane temperature at R_c	20
Atmosphere temperature at R_c	104
Surface density at R_c	0.79
Temperature power-law index	0.55
Vertical temperature gradient index	2
UV Flux ^b at R_c (in Draine (1978b) ’s units)	3400

^a [Andrews et al. \(2012\)](#)

^b [Herczeg et al. \(2004\)](#)

and destruction pathways are involved in the chemistry of CH₂CN. These are summarized in Table 2.

As previously mentioned, CH₃CN and CH₂CN are found to have similar excitation temperatures and morphologies, therefore it is unsurprising that they also share a comparable chemistry. Both CH₃CN and CH₂CN share a very similar grain-surface formation chemistry where both can be formed via solid state re-

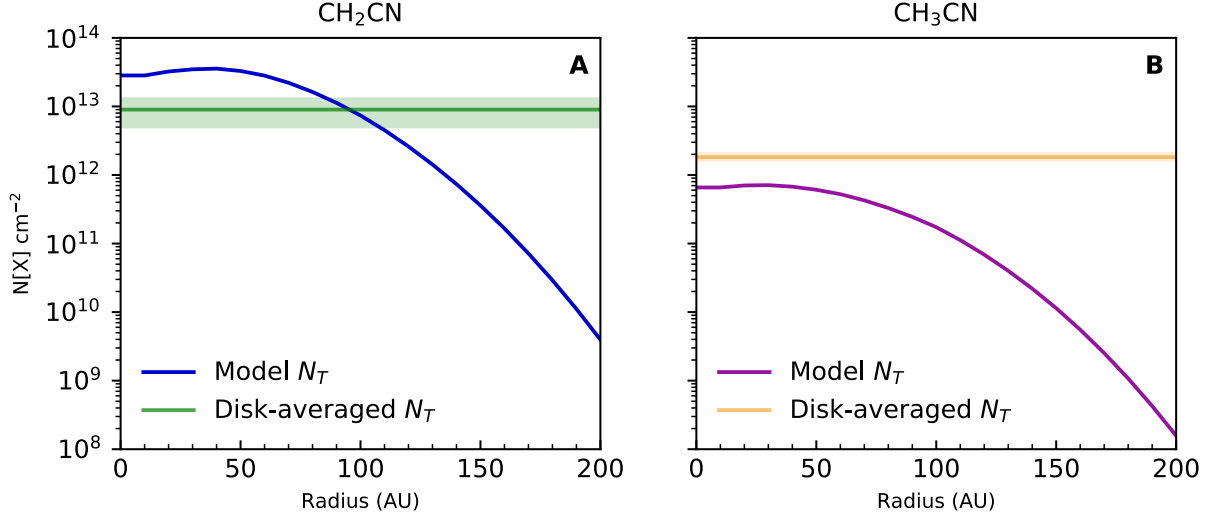
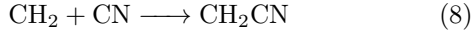
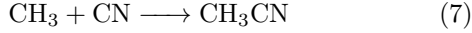
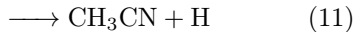


Figure 5. Total column densities of CH₂CN (Panel A) and CH₃CN (Panel B) as a function of radius, predicted by the chemical models of [Le Gal et al. \(2019\)](#) that we adapted to TW Hya as described in §4.1. The disk-averaged value derived from the observations presented in Sect. 3.2 for CH₂CN (A) and obtained by [Loomis et al. \(2018\)](#) for CH₃CN (B) are also shown.

actions with CN as follows,



([Herbst 1985](#)). From these reactions we can infer that the relative formation rates of CH₃CN and CH₂CN will depend on the relative abundance of CH₂ and CH₃ radicals on the grain surface. The similarities extend beyond these grain-surface reactions, as these molecules share a common gas-phase reaction pathway. The electronic dissociative recombination of CH₃CNH⁺ has been identified as the dominant contributor to the gas-phase formation of both CH₃CN and CH₂CN ([Vastel et al. 2015](#); [Loomis et al. 2018](#)). The full reaction route, including the formation of the ion intermediate, is as follows:



([Herbst & Leung 1990](#)). This does not seem to be the main formation pathway for CH₂CN in either the model or in ‘reality’ since the electronic dissociative recombination (DR) of CH₃CNH⁺ leads to CH₂CN/CH₃CN=0.5 (see Table 2) while we find that CH₂CN ≫ CH₃CN. In light of this, we suggest that the grain surface formation pathway is the most important source of CH₂CN in disks. A similar conclusion was made with respect to CH₃CN by ([Le Gal et al. 2019](#)) and ([Loomis et al. 2018](#)). However, grain-surface reactions are poorly constrained both theoretically and experimentally and therefore more experimental studies need to be carried

out to verify the significance of this solid-state reaction. Finally we note that CH₂CN can also form through several neutral-neutral reactions (Table 2), whose possible contributions also warrant further investigation.

4.3. Morphology

As mentioned in Section 2.2, CH₂CN is found in a ring morphology when imaged at the native resolution of ≈ 0.3″. The ring morphology is not unique to CH₂CN as CN and C₂H are also analogously distributed in TW Hya, however, their rings peak at considerably larger radii at ∼ 45 au (0.75″) and 60 au (1″), respectively ([Bergin et al. 2016](#); [Teague & Loomis 2020](#)). These nested rings of potentially chemically related species provide clues as to what processes are regulating the abundance of these molecules. One possible source of rings is the increased penetration of UV radiation beyond the edge of the dust continuum, leading to more photo-desorption of frozen out molecules from grain surfaces ([Cleeves 2016](#)). However, the edge of the dust continuum is at ∼ 60 au, which is inconsistent with the peak of the CH₂CN ring (∼ 24 au) therefore this is not a plausible explanation for the morphology of CH₂CN.

The chemical model results for CH₂CN shown in Figure 5, seem to replicate the morphology that we observed in Figure 4C. This suggests the presence of a ‘Goldilocks zone’ for the dominant formation pathway where the observed morphology can be attributed to the balance between formation and destruction reactions under fiducial disk conditions. Within this zone of the disk, the conditions may be particularly favourable for the pro-

duction of CH₂CN (i.e. optimal UV radiation flux or temperature of the disk molecular layer).

Another possible factor that could shape the distribution of CH₂CN is enhanced destruction in the inner disk due to reactions with gas-phase carbon and oxygen atoms. Chemical modeling by [Du et al. \(2015\)](#) has shown that C and O depletion is needed to reproduce the observed molecular abundances of CO and H₂O in TW Hya. Further, nitrile column density is enhanced by ~ 2 orders of magnitude where C and O depletion takes place ([Du et al. 2015](#)). One disk location that may present a rapid change in the C and O abundance is the CO snowline, where CO ice sublimates back into the gas-phase. The CO snowline zone in TW Hya is found at 17-30 au ([Schwarz et al. 2016](#); [Qi et al. 2013](#)). We find that CH₂CN peaks at ~ 24 au, so the CO snowline and the CH₂CN peak may reflect the presence of C- and O-depleted gas just exterior to the CO snowline. Exterior to this region, carbon and oxygen would primarily exist as CO ice, therefore not interfere with nitrile chemistry.

5. SUMMARY

We have presented the first detection of CH₂CN (cyanomethyl) in a protoplanetary disk. The 6 emission lines detected correspond to 6 transitions of CH₂CN in its ortho state. We find a disk-averaged rotational temperature of 38 ± 5 K and a disk-averaged total column density of $3.5^{+0.3}_{-0.3} \times 10^{12} \text{ cm}^{-2}$. Assuming a thermal ortho/para ratio of 3:1, we infer a total CH₂CN column

density of $4.7^{+0.4}_{-0.4} \times 10^{12} \text{ cm}^{-2}$. The molecule is observed to be in a ring whereas at lower spatial resolutions it presents a centrally-peaked profile consistent with previously reported CH₃CN morphology. Comparison with CH₃CN total column density shows that CH₂CN is 10 times more abundant. This result is consistent with chemical models for TW Hya, where CH₂CN \gg CH₃CN at all disk radii. We identify possible pathways that contribute to the formation and destruction of this molecule and we suggest that grain-surface reactions are the likely formation pathway for both CH₂CN and CH₃CN.

ACKNOWLEDGMENTS

This paper makes use of the following ALMA data: ADS/JAO.ALMA#2018.A.00021. ALMA is a partnership of ESO (representing its member states), NSF (USA) and NINS (Japan), together with NRC (Canada), MOST and ASIAA (Taiwan), and KASI (Republic of Korea), in cooperation with the Republic of Chile. The Joint ALMA Observatory is operated by ESO, AUI/NRAO and NAOJ. The National Radio Astronomy Observatory is a facility of the National Science Foundation operated under cooperative agreement by Associated Universities, Inc. AC acknowledges funding from the Origins of Life Initiative. This work was supported by an award from the Simons Foundation (SCOL # 321183, KÖ).

REFERENCES

- Altwegg, K., Balsiger, H., Hänni, N., et al. 2020, *Nature Astronomy*, 4, 533, doi: [10.1038/s41550-019-0991-9](#)
- Andrews, S. M., Wilner, D. J., Hughes, A. M., et al. 2012, *ApJ*, 744, 162, doi: [10.1088/0004-637X/744/2/162](#)
- Andrews, S. M., Huang, J., Pérez, L. M., et al. 2018, *ApJL*, 869, L41, doi: [10.3847/2041-8213/aaf741](#)
- Bailer-Jones, C. A. L., Rybizki, J., Founesneau, M., Mantelet, G., & Andrae, R. 2018, *AJ*, 156, 58, doi: [10.3847/1538-3881/aac621](#)
- Bergin, E. A., Du, F., Cleeves, L. I., et al. 2016, *ApJ*, 831, 101, doi: [10.3847/0004-637X/831/1/101](#)
- Bergner, J. B., Guzmán, V. G., Öberg, K. I., Loomis, R. A., & Pegues, J. 2018, *ApJ*, 857, 69, doi: [10.3847/1538-4357/aab664](#)
- Chapillon, E., Dutrey, A., Guilloteau, S., et al. 2012, *ApJ*, 756, 58, doi: [10.1088/0004-637X/756/1/58](#)
- Cleeves, L. I. 2016, *ApJL*, 816, L21, doi: [10.3847/2041-8205/816/2/L21](#)
- Draine, B. T. 1978a, *ApJS*, 36, 595, doi: [10.1086/190513](#)
- . 1978b, *ApJS*, 36, 595, doi: [10.1086/190513](#)
- Du, F., Bergin, E. A., & Hogerheijde, M. R. 2015, *ApJL*, 807, L32, doi: [10.1088/2041-8205/807/2/L32](#)
- Dutrey, A., Guilloteau, S., & Guelin, M. 1997, *A&A*, 317, L55
- Endres, C. P., Schlemmer, S., Schilke, P., Stutzki, J., & Müller, H. S. P. 2016, *Journal of Molecular Spectroscopy*, 327, 95, doi: [10.1016/j.jms.2016.03.005](#)
- Goldsmith, P. F., & Langer, W. D. 1999, *ApJ*, 517, 209, doi: [10.1086/307195](#)
- Guzmán, V. V., Öberg, K. I., Loomis, R., & Qi, C. 2015, *ApJ*, 814, 53, doi: [10.1088/0004-637X/814/1/53](#)
- Herbst, E. 1985, *ApJ*, 291, 226, doi: [10.1086/163060](#)
- Herbst, E., & Leung, C. M. 1990, *A&A*, 233, 177
- Herczeg, G. J., Wood, B. E., Linsky, J. L., Valenti, J. A., & Johns-Krull, C. M. 2004, *ApJ*, 607, 369, doi: [10.1086/383340](#)
- Hily-Blant, P., Magalhaes, V., Kastner, J., et al. 2017, *A&A*, 603, L6, doi: [10.1051/0004-6361/201730524](#)

- Huang, J., Andrews, S. M., Cleeves, L. I., et al. 2018, *ApJ*, 852, 122, doi: [10.3847/1538-4357/aaa1e7](https://doi.org/10.3847/1538-4357/aaa1e7)
- Irvine, W. M., Friberg, P., Hjalmarsen, A., et al. 1988, *ApJL*, 334, L107, doi: [10.1086/185323](https://doi.org/10.1086/185323)
- Jones, E., Oliphant, T., & Peterson, P. 2001
- Kastner, J. H., Zuckerman, B., Weintraub, D. A., & Forveille, T. 1997, *Science*, 277, 67, doi: [10.1126/science.277.5322.67](https://doi.org/10.1126/science.277.5322.67)
- Le Gal, R., Brady, M. T., Öberg, K. I., Roueff, E., & Le Petit, F. 2019, *ApJ*, 886, 86, doi: [10.3847/1538-4357/ab4ad9](https://doi.org/10.3847/1538-4357/ab4ad9)
- Le Gal, R., Xie, C., Herbst, E., et al. 2017, *A&A*, 608, A96, doi: [10.1051/0004-6361/201731566](https://doi.org/10.1051/0004-6361/201731566)
- Loomis, R. A., Cleeves, L. I., Öberg, K. I., et al. 2018, *ApJ*, 859, 131, doi: [10.3847/1538-4357/aac169](https://doi.org/10.3847/1538-4357/aac169)
- McGuire, B. A. 2018, *ApJS*, 239, 17, doi: [10.3847/1538-4365/aae5d2](https://doi.org/10.3847/1538-4365/aae5d2)
- McMullin, J. P., Waters, B., Schiebel, D., Young, W., & Golap, K. 2007, in *Astronomical Society of the Pacific Conference Series*, Vol. 376, *Astronomical Data Analysis Software and Systems XVI*, ed. R. A. Shaw, F. Hill, & D. J. Bell, 127
- Müller, H. S. P., Thorwirth, S., Roth, D. A., & Winnewisser, G. 2001, *A&A*, 370, L49, doi: [10.1051/0004-6361:20010367](https://doi.org/10.1051/0004-6361:20010367)
- Mumma, M. J., & Charnley, S. B. 2011, *ARA&A*, 49, 471, doi: [10.1146/annurev-astro-081309-130811](https://doi.org/10.1146/annurev-astro-081309-130811)
- Nomura, H., Tsukagoshi, T., Kawabe, R., et al. 2016, *ApJL*, 819, L7, doi: [10.3847/2041-8205/819/1/L7](https://doi.org/10.3847/2041-8205/819/1/L7)
- Oberg, K. I. 2016, arXiv e-prints, arXiv:1609.03112. <https://arxiv.org/abs/1609.03112>
- Oberg, K. I., & Bergin, E. A. 2020, arXiv e-prints, arXiv:2010.03529. <https://arxiv.org/abs/2010.03529>
- Öberg, K. I., Guzmán, V. V., Furuya, K., et al. 2015, *Nature*, 520, 198, doi: [10.1038/nature14276](https://doi.org/10.1038/nature14276)
- Patel, B. H., Percivalle, C., Ritson, D. J., Duffy, C. D., & Sutherland, J. D. 2015, *Nature Chemistry*, 7, 301, doi: [10.1038/nchem.2202](https://doi.org/10.1038/nchem.2202)
- Powner, M. W., Gerland, B., & Sutherland, J. D. 2009, *Nature*, 459, 239, doi: [10.1038/nature08013](https://doi.org/10.1038/nature08013)
- Qi, C., Kessler, J. E., Koerner, D. W., Sargent, A. I., & Blake, G. A. 2003, *ApJ*, 597, 986, doi: [10.1086/378494](https://doi.org/10.1086/378494)
- Qi, C., Öberg, K. I., Wilner, D. J., et al. 2013, *Science*, 341, 630, doi: [10.1126/science.1239560](https://doi.org/10.1126/science.1239560)
- Schwarz, K. R., Bergin, E. A., Cleeves, L. I., et al. 2016, *ApJ*, 823, 91, doi: [10.3847/0004-637X/823/2/91](https://doi.org/10.3847/0004-637X/823/2/91)
- Teague, R. 2019, *Research Notes of the AAS*, 3, 74, doi: [10.3847/2515-5172/ab2125](https://doi.org/10.3847/2515-5172/ab2125)
- Teague, R., & Loomis, R. 2020, *ApJ*, 899, 157, doi: [10.3847/1538-4357/aba956](https://doi.org/10.3847/1538-4357/aba956)
- van Dishoeck, E. F. 1994, in *Astronomical Society of the Pacific Conference Series*, Vol. 58, *The First Symposium on the Infrared Cirrus and Diffuse Interstellar Clouds*, ed. R. M. Cutri & W. B. Latter, 319
- Vastel, C., Yamamoto, S., Lefloch, B., & Bachiller, R. 2015, *A&A*, 582, L3, doi: [10.1051/0004-6361/201527153](https://doi.org/10.1051/0004-6361/201527153)
- Wakelam, V., Herbst, E., Loison, J. C., et al. 2012, *ApJS*, 199, 21, doi: [10.1088/0067-0049/199/1/21](https://doi.org/10.1088/0067-0049/199/1/21)
- Walsh, C., Loomis, R. A., Öberg, K. I., et al. 2016, *ApJL*, 823, L10, doi: [10.3847/2041-8205/823/1/L10](https://doi.org/10.3847/2041-8205/823/1/L10)
- Woon, D. E., & Herbst, E. 2009, *ApJS*, 185, 273, doi: [10.1088/0067-0049/185/2/273](https://doi.org/10.1088/0067-0049/185/2/273)

References

- Agúndez, M., Cernicharo, J., & Goicoechea, J. R. 2008, *A&A*, 483, 831
- Aikawa, Y., & Herbst, E. 1999, *A&A*, 351, 233
- ALMA Partnership, Brogan, C. L., Pérez, L. M., et al. 2015, *ApJ*, 808, L3
- Altwegg, K., Balsiger, H., Hänni, N., et al. 2020, *Nature Astronomy*, 4, 533
- Andrews, S. M., Wilner, D. J., Hughes, A. M., et al. 2012, *ApJ*, 744, 162
- Andrews, S. M., Wilner, D. J., Zhu, Z., et al. 2016, *ApJ*, 820, L40
- Andrews, S. M., Huang, J., Pérez, L. M., et al. 2018, *ApJ*, 869, L41
- Arce, H. G., & Sargent, A. I. 2005, *ApJ*, 624, 232
- Armitage, P. J. 2018, *A Brief Overview of Planet Formation*, ed. H. J. Deeg & J. A. Belmonte, 135
- Artur de la Villarmois, E., Kristensen, L. E., Jørgensen, J. K., et al. 2018, *A&A*, 614, A26
- Bacmann, A., Taquet, V., Faure, A., Kahane, C., & Ceccarelli, C. 2012, *A&A*, 541, L12

REFERENCES

- Bailer-Jones, C. A. L., Rybizki, J., Fouesneau, M., Mantelet, G., & Andrae, R. 2018, *AJ*, 156, 58
- Balucani, N., Ceccarelli, C., & Taquet, V. 2015, *MNRAS*, 449, L16
- Bates, D. R. 1950, *Physical Review*, 78, 492
- Beaklini, P. P. B., Mendoza, E., Canelo, C. M., et al. 2020, *MNRAS*, 491, 427
- Beckwith, S., Sargent, A. I., Scoville, N. Z., et al. 1986, *ApJ*, 309, 755
- Behmard, A., Fayolle, E. C., Graninger, D. M., et al. 2019, *ApJ*, 875, 73
- Belloche, A., Garrod, R. T., Müller, H. S. P., et al. 2009, *A&A*, 499, 215
- Bennett, C. J., Jamieson, C. S., Osamura, Y., & Kaiser, R. I. 2005, *ApJ*, 624, 1097
- . 2006, *ApJ*, 653, 792
- Benson, P. J., & Myers, P. C. 1989, *ApJS*, 71, 89
- Bergin, E., Calvet, N., D’Alessio, P., & Herczeg, G. J. 2003, *ApJ*, 591, L159
- Bergin, E. A., Aikawa, Y., Blake, G. A., & van Dishoeck, E. F. 2007, in *Protostars and Planets V*, ed. B. Reipurth, D. Jewitt, & K. Keil, 751
- Bergin, E. A., Cleeves, L. I., Crockett, N., & Blake, G. A. 2014, *Faraday Discussions*, 168, 61
- Bergin, E. A., Du, F., Cleeves, L. I., et al. 2016, *ApJ*, 831, 101
- Bergin, E. A., & Tafalla, M. 2007, *ARA&A*, 45, 339
- Bergin, E. A., Cleeves, L. I., Gorti, U., et al. 2013, *Nature*, 493, 644

REFERENCES

- Bergner, J. B., Guzmán, V. G., Öberg, K. I., Loomis, R. A., & Pegues, J. 2018, *ApJ*, 857, 69
- Bergner, J. B., Öberg, K. I., & Rajappan, M. 2019, *ApJ*, 874, 115
- Bisschop, S. E., Fraser, H. J., Öberg, K. I., van Dishoeck, E. F., & Schlemmer, S. 2006, *A&A*, 449, 1297
- Bisschop, S. E., Jørgensen, J. K., van Dishoeck, E. F., & de Wachter, E. B. M. 2007, *A&A*, 465, 913
- Biver, N., Bockelée-Morvan, D., Crovisier, J., et al. 2002, *Earth Moon and Planets*, 90, 323
- Blake, G. A., van Dishoeck, E. F., & Sargent, A. I. 1992, *ApJ*, 391, L99
- Boogert, A. C. A., Gerakines, P. A., & Whittet, D. C. B. 2015, *ARA&A*, 53, 541
- Bottinelli, S., Boogert, A. C. A., Bouwman, J., et al. 2010, *ApJ*, 718, 1100
- Bouilloud, M., Fray, N., Bénilan, Y., et al. 2015, *MNRAS*, 451, 2145
- Cami, J., Bernard-Salas, J., Peeters, E., & Malek, S. E. 2010, *Science*, 329, 1180
- Carr, J. S., & Najita, J. R. 2008, *Science*, 319, 1504
- Carr, J. S., Tokunaga, A. T., & Najita, J. 2004, *ApJ*, 603, 213
- Chapillon, E., Dutrey, A., Guilloteau, S., et al. 2012, *ApJ*, 756, 58
- Chin, C.-H., Chen, S.-C., Liu, M.-C., Huang, T.-P., & Wu, Y.-J. 2016, *ApJS*, 224, 17

REFERENCES

- Cleeves, L. I. 2016, *ApJ*, 816, L21
- Cleeves, L. I., Bergin, E. A., Qi, C., Adams, F. C., & Öberg, K. I. 2015, *The Astrophysical Journal*, 799, 204
- Clem, J. M., Clements, D. P., Esposito, J., et al. 1996, *ApJ*, 464, 507
- Codella, C., Benedettini, M., Beltrán, M. T., et al. 2009, *A&A*, 507, L25
- Collings, M. P., Anderson, M. A., Chen, R., et al. 2004, *MNRAS*, 354, 1133
- Crovisier, J., Biver, N., Bockelée-Morvan, D., et al. 2009, *Earth Moon and Planets*, 105, 267
- D'Alessio, P., Calvet, N., Hartmann, L., Lizano, S., & Cantó, J. 1999, *ApJ*, 527, 893
- D'Angelo, G., & Lissauer, J. J. 2018, *Formation of Giant Planets*, ed. H. J. Deeg & J. A. Belmonte, 140
- Danger, G., Bossa, J. B., de Marcellus, P., et al. 2011, *A&A*, 525, A30
- D'Hendecourt, L. B., & Allamandola, L. J. 1986, *A&AS*, 64, 453
- Draine, B. T. 1978, *ApJS*, 36, 595
- . 2003, *ARA&A*, 41, 241
- Du, F., Bergin, E. A., & Hogerheijde, M. R. 2015, *ApJ*, 807, L32
- Duley, W. W., & Hu, A. 2009, *ApJ*, 698, 808
- Dutrey, A., Guilloteau, S., & Guelin, M. 1997, *A&A*, 317, L55

REFERENCES

- Dutrey, A., Guilloteau, S., & Simon, M. 1994, *A&A*, 286, 149
- Dutrey, A., Henning, T., Guilloteau, S., et al. 2007, *A&A*, 464, 615
- Elsila, J. E., Dworkin, J. P., Bernstein, M. P., Martin, M. P., & Sandford, S. A. 2007, *ApJ*, 660, 911
- Endres, C. P., Schlemmer, S., Schilke, P., Stutzki, J., & Müller, H. S. P. 2016, *Journal of Molecular Spectroscopy*, 327, 95
- Favre, C., Fedele, D., Semenov, D., et al. 2018, *ApJ*, 862, L2
- Ferrari, F., & Szuszkiewicz, E. 2009, *Astrobiology*, 9, 413
- Ferris, J. P., & Ishikawa, Y. 1987, *Nature*, 326, 777
- Förstel, M., Bergantini, A., Maksyutenko, P., Góbi, S., & Kaiser, R. I. 2017, *ApJ*, 845, 83
- Fortier, A., Alibert, Y., Carron, F., Benz, W., & Dittkrist, K. M. 2013, *A&A*, 549, A44
- Fuente, A., Cernicharo, J., Agúndez, M., et al. 2010, *A&A*, 524, A19
- Garrod, R. T., & Herbst, E. 2006, *A&A*, 457, 927
- Gibb, E. L., & Horne, D. 2013, *ApJ*, 776, L28
- Goldsmith, P. F., & Langer, W. D. 1999, *ApJ*, 517, 209
- Guilloteau, S., Di Folco, E., Dutrey, A., et al. 2013, *A&A*, 549, A92
- Guilloteau, S., Dutrey, A., Wakelam, V., et al. 2012, *A&A*, 548, A70

REFERENCES

- Guzmán, V. V., Öberg, K. I., Loomis, R., & Qi, C. 2015, *ApJ*, 814, 53
- Harsono, D., Bjerkeli, P., van der Wiel, M. H. D., et al. 2018, *Nature Astronomy*, 2, 646
- Hasegawa, T. I., & Herbst, E. 1993, *MNRAS*, 263, 589
- Henning, T., & Semenov, D. 2013, *Chemical Reviews*, 113, 9016
- Herbst, E. 1985, *ApJ*, 291, 226
- Herbst, E., & Klemperer, W. 1973, *ApJ*, 185, 505
- Herbst, E., & van Dishoeck, E. F. 2009, *ARA&A*, 47, 427
- Herczeg, G. J., Linsky, J. L., Valenti, J. A., Johns-Krull, C. M., & Wood, B. E. 2002, *ApJ*, 572, 310
- Herczeg, G. J., Wood, B. E., Linsky, J. L., Valenti, J. A., & Johns-Krull, C. M. 2004, *ApJ*, 607, 369
- Hily-Blant, P., Magalhaes, V., Kastner, J., et al. 2017, *A&A*, 603, L6
- Hily-Blant, P., Magalhaes de Souza, V., Kastner, J., & Forveille, T. 2019, *A&A*, 632, L12
- Hiraoka, K., Yamashita, A., Yachi, Y., et al. 1995, *ApJ*, 443, 363
- Hogerheijde, M. R., Bergin, E. A., Brinch, C., et al. 2011, *Science*, 334, 338
- Hollenbach, D. J., & Tielens, A. G. G. M. 1997, *ARA&A*, 35, 179
- Huang, J., & Öberg, K. I. 2015, *ApJ*, 809, L26

REFERENCES

- Huang, J., Andrews, S. M., Cleaves, L. I., et al. 2018, *ApJ*, 852, 122
- Hudson, R. L., Ferrante, R. F., & Moore, M. H. 2014a, *Icarus*, 228, 276
- Hudson, R. L., Gerakines, P. A., & Moore, M. H. 2014b, *Icarus*, 243, 148
- Hudson, R. L., & Moore, M. H. 2004, *Icarus*, 172, 466
- Ingleby, L., Calvet, N., Herczeg, G., et al. 2013, *ApJ*, 767, 112
- Jones, E., Oliphant, T., & Peterson, P. 2001
- Jørgensen, J. K., Belloche, A., & Garrod, R. T. 2020, *ARA&A*, 58, 727
- Kaiser, R. I., Stockton, A. M., Kim, Y. S., Jensen, E. C., & Mathies, R. A. 2013, *ApJ*, 765, 111
- Kastner, J. H., Qi, C., Gorti, U., et al. 2015, *ApJ*, 806, 75
- Kastner, J. H., Zuckerman, B., Weintraub, D. A., & Forveille, T. 1997, *Science*, 277, 67
- Keane, T. C. 2017, *Origins of Life and Evolution of the Biosphere*, 47, 223
- Kim, Y. S., Bennett, C. J., Chen, L.-H., O'Brien, K., & Kaiser, R. I. 2010, *ApJ*, 711, 744
- Kim, Y. S., & Kaiser, R. I. 2011, *ApJ*, 729, 68
- Kundu, S., Prabhudesai, V. S., & Krishnakumar, E. 2017, *Phys. Chem. Chem. Phys.*, 19, 25723
- Lahuis, F., van Dishoeck, E. F., Boogert, A. C. A., et al. 2006, *ApJ*, 636, L145

REFERENCES

- Larson, R. B. 2003, *Reports on Progress in Physics*, 66, 1651
- Lauck, T., Karssemeijer, L., Shulenberger, K., et al. 2015, *ApJ*, 801, 118
- Le Gal, R., Brady, M. T., Öberg, K. I., Roueff, E., & Le Petit, F. 2019a, *ApJ*, 886, 86
- . 2019b, *ApJ*, 886, 86
- Le Gal, R., Öberg, K. I., Loomis, R. A., Pegues, J., & Bergner, J. B. 2019c, *ApJ*, 876, 72
- Le Gal, R., Xie, C., Herbst, E., et al. 2017, *A&A*, 608, A96
- Leger, A. 1987, in *Astrochemistry*, ed. M. S. Vardya & S. P. Tarafdar, Vol. 120, 539–542
- Li, X., Heays, A. N., Visser, R., et al. 2013, *A&A*, 555, A14
- Lissauer, J. J. 1993, *ARA&A*, 31, 129
- Liszt, H., Gerin, M., Beasley, A., & Pety, J. 2018, *ApJ*, 856, 151
- Loomis, R. A., Cleeves, L. I., Öberg, K. I., et al. 2018, *ApJ*, 859, 131
- Loomis, R. A., Zaleski, D. P., Steber, A. L., et al. 2013, *ApJ*, 765, L9
- Manara, C. F., Morbidelli, A., & Guillot, T. 2018, *A&A*, 618, L3
- Mandell, A. M., Mumma, M. J., Blake, G. A., et al. 2008, *ApJ*, 681, L25
- Martín-Doménech, R., Maksiutenko, P., Öberg, K. I., & Rajappan, M. 2020, *ApJ*, 902, 116

REFERENCES

- McGuire, B. A. 2018, *ApJS*, 239, 17
- McGuire, B. A., Burkhardt, A. M., Kalenskii, S., et al. 2018, *Science*, 359, 202
- McMullin, J. P., Waters, B., Schiebel, D., Young, W., & Golap, K. 2007, in *Astronomical Society of the Pacific Conference Series*, Vol. 376, *Astronomical Data Analysis Software and Systems XVI*, ed. R. A. Shaw, F. Hill, & D. J. Bell, 127
- Melli, A., Melosso, M., Tasinato, N., et al. 2018, *ApJ*, 855, 123
- Mewaldt, R. A., Selesnick, R. S., & Cummings, J. R. 1996, Washington DC American Geophysical Union Geophysical Monograph Series, 97, 35
- Miotello, A., Facchini, S., van Dishoeck, E. F., et al. 2019, *A&A*, 631, A69
- Mizuno, H. 1981, in *Fundamental Problems in the Theory of Stellar Evolution*, ed. D. Sugimoto, D. Q. Lamb, & D. N. Schramm, Vol. 93, 133
- Monnier, J. D. 2003, *Reports on Progress in Physics*, 66, 789
- Moore, M. H., Ferrante, R. F., & Hudson, R. L. 2007, in *AGU Fall Meeting Abstracts*, Vol. 2007, P11D–0804
- Moore, M. H., & Hudson, R. L. 1998, *Icarus*, 135, 518
- . 2003, *Icarus*, 161, 486
- Muñoz Caro, G. M., Meierhenrich, U. J., Schutte, W. A., et al. 2002, *Nature*, 416, 403

REFERENCES

- Müller, H. S. P., Thorwirth, S., Roth, D. A., & Winnewisser, G. 2001, *A&A*, 370, L49
- Mumma, M. J., & Charnley, S. B. 2011, *ARA&A*, 49, 471
- Nayakshin, S., Tsukagoshi, T., Hall, C., et al. 2020, *MNRAS*, 495, 285
- Nuevo, M., Bredehöft, J. H., Meierhenrich, U. J., d’Hendecourt, L., & Thiemann, W. H. P. 2010, *Astrobiology*, 10, 245
- Öberg, K. I. 2016, arXiv e-prints, arXiv:1609.03112
- Öberg, K. I., & Bergin, E. A. 2020, arXiv e-prints, arXiv:2010.03529
- Öberg, K. I., Bottinelli, S., Jørgensen, J. K., & van Dishoeck, E. F. 2010, *ApJ*, 716, 825
- Öberg, K. I., Guzmán, V. V., Furuya, K., et al. 2015, *Nature*, 520, 198
- Öberg, K. I., Guzmán, V. V., Merchantz, C. J., et al. 2017, *ApJ*, 839, 43
- Ohishi, M., Suzuki, H., Ishikawa, S.-I., et al. 1991, *ApJ*, 380, L39
- Patel, B. H., Percivalle, C., Ritson, D. J., Duffy, C. D., & Sutherland, J. D. 2015, *Nature Chemistry*, 7, 301
- Phuong, N. T., Chapillon, E., Majumdar, L., et al. 2018, *A&A*, 616, L5
- Pollack, J. B., Hubickyj, O., Bodenheimer, P., et al. 1991, in *Bulletin of the American Astronomical Society*, Vol. 23, 1225
- Pontoppidan, K. M., Salyk, C., Banzatti, A., et al. 2019, *ApJ*, 874, 92

REFERENCES

- Powner, M. W., Gerland, B., & Sutherland, J. D. 2009, *Nature*, 459, 239
- Qi, C., Kessler, J. E., Koerner, D. W., Sargent, A. I., & Blake, G. A. 2003, *ApJ*, 597, 986
- Qi, C., Öberg, K. I., Wilner, D. J., & Rosenfeld, K. A. 2013, *ApJ*, 765, L14
- Qi, C., Wilner, D. J., Aikawa, Y., Blake, G. A., & Hogerheijde, M. R. 2008, *ApJ*, 681, 1396
- Qi, C., Ho, P. T. P., Wilner, D. J., et al. 2004, *ApJ*, 616, L11
- Reboussin, L., Wakelam, V., Guilloteau, S., & Hersant, F. 2014, *MNRAS*, 440, 3557
- Ribeiro, F. d. A., Almeida, G. C., Wolff, W., et al. 2020, *MNRAS*, 492, 2140
- Salinas, V. N., Hogerheijde, M. R., Bergin, E. A., et al. 2016, *A&A*, 591, A122
- Salyk, C., Pontoppidan, K. M., Blake, G. A., et al. 2008, *ApJ*, 676, L49
- Sargent, A. I., & Beckwith, S. 1987, *ApJ*, 323, 294
- Schindhelm, E., France, K., Herczeg, G. J., et al. 2012, *ApJ*, 756, L23
- Schwarz, K. R., Bergin, E. A., Cleeves, L. I., et al. 2016, *ApJ*, 823, 91
- Semenov, D. A. 2011, in *The Molecular Universe*, ed. J. Cernicharo & R. Bachiller, Vol. 280, 114–126
- Shen, C. J., Greenberg, J. M., Schutte, W. A., & van Dishoeck, E. F. 2004, *A&A*, 415, 203

REFERENCES

- Shu, F. H., Ruden, S. P., Lada, C. J., & Lizano, S. 1991, *ApJ*, 370, L31
- Smith, R. L., Pontoppidan, K. M., Young, E. D., Morris, M. R., & van Dishoeck, E. F. 2009, *ApJ*, 701, 163
- Snyder, L. E., & Buhl, D. 1971, *ApJ*, 163, L47
- Stolkin, I., Ha, T. K., & Günthard, H. H. 1977, *Chemical Physics*, 21, 327
- Teague, R., & Loomis, R. 2020, *ApJ*, 899, 157
- Teague, R., Semenov, D., Gorti, U., et al. 2017, *ApJ*, 835, 228
- Thi, W.-F., van Dishoeck, E. F., Blake, G. A., van Zadelhoff, G.-J., & Hogerheijde, M. R. 1999, *ApJ*, 521, L63
- Thi, W. F., Ménard, F., Meeus, G., et al. 2011, *A&A*, 530, L2
- Tielens, A. G. G. M., & Allamandola, L. J. 1987, *Composition, Structure, and Chemistry of Interstellar Dust*, ed. D. J. Hollenbach & J. Thronson, *Harley A.*, Vol. 134, 397
- Tielens, A. G. G. M., & Hagen, W. 1982, *A&A*, 114, 245
- Tsukagoshi, T., Nomura, H., Muto, T., et al. 2016, *ApJ*, 829, L35
- van der Tak, F. F. S., Boonman, A. M. S., Braakman, R., & van Dishoeck, E. F. 2003, in *SFChem 2002: Chemistry as a Diagnostic of Star Formation*, ed. C. L. Curry & M. Fich, 437

REFERENCES

- van Dishoeck, E. F. 1994, in *Astronomical Society of the Pacific Conference Series*, Vol. 58, *The First Symposium on the Infrared Cirrus and Diffuse Interstellar Clouds*, ed. R. M. Cutri & W. B. Latter, 319
- van Dishoeck, E. F., & Black, J. H. 1988, *ApJ*, 334, 771
- van Dishoeck, E. F., Thi, W. F., & van Zadelhoff, G. J. 2003, *A&A*, 400, L1
- van Dishoeck, E. F., & van der Tak, F. F. S. 2002, *Highlights of Astronomy*, 12, 146
- van Zadelhoff, G. J., van Dishoeck, E. F., Thi, W. F., & Blake, G. A. 2001, *A&A*, 377, 566
- Vastel, C., Ceccarelli, C., Lefloch, B., & Bachiller, R. 2014, *ApJ*, 795, L2
- Vasyunin, A. I., Caselli, P., Dulieu, F., & Jiménez-Serra, I. 2017, *ApJ*, 842, 33
- Vasyunin, A. I., & Herbst, E. 2013, *ApJ*, 769, 34
- Visser, R., van Dishoeck, E. F., Doty, S. D., & Dullemond, C. P. 2009, *A&A*, 495, 881
- Wakelam, V., Smith, I. W. M., Herbst, E., et al. 2010, *Space Sci. Rev.*, 156, 13
- Wakelam, V., Herbst, E., Loison, J. C., et al. 2012, *ApJS*, 199, 21
- Wakelam, V., Bron, E., Cazaux, S., et al. 2017, *Molecular Astrophysics*, 9, 1
- Walsh, C., Nomura, H., & van Dishoeck, E. 2015, *A&A*, 582, A88
- Walsh, C., Loomis, R. A., Öberg, K. I., et al. 2016, *ApJ*, 823, L10

REFERENCES

- Watanabe, N., & Kouchi, A. 2002, *ApJ*, 571, L173
- Weinberger, A. J., Anglada-Escudé, G., & Boss, A. P. 2013, *ApJ*, 762, 118
- Willacy, K., Klahr, H. H., Millar, T. J., & Henning, T. 1998, *A&A*, 338, 995
- Williams, J. P., Cieza, L., Hales, A., et al. 2019, *ApJ*, 875, L9
- Williams, J. P., & Cieza, L. A. 2011, *ARA&A*, 49, 67
- Williams, J. P., de Geus, E. J., & Blitz, L. 1994, *ApJ*, 428, 693
- Woon, D. E. 2002, *ApJ*, 571, L177
- Woon, D. E., & Herbst, E. 2009, *ApJS*, 185, 273
- Wu, Y.-J., Wu, C. Y. R., Chou, S.-L., et al. 2012, *ApJ*, 746, 175
- Youdin, A. N., & Goodman, J. 2005, *ApJ*, 620, 459
- Zhou, L., Zheng, W., Kaiser, R. I., et al. 2010, *ApJ*, 718, 1243